PHOTOMETRY AND SPECTROSCOPY OF LOW MASS STARS AND BROWN DWARFS

A thesis submitted
for the degree of
Doctor of Philosophy

by

Iain A Steele

Astronomy Group
Department of Physics and Astronomy
University of Leicester

October 1994

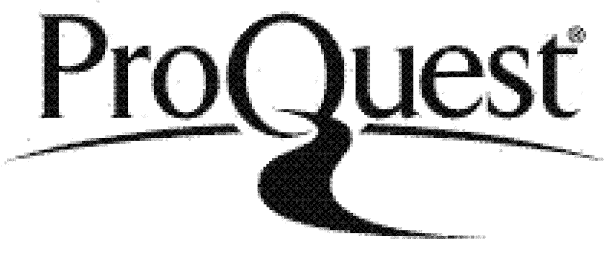

ProQuest LLC
789 East Eisenhower Parkway
P.O. Box 1346
Ann Arbor, MI 48106-1346

PHOTOMETRY AND SPECTROSCOPY OF LOW MASS STARS AND BROWN DWARFS

Abstract

This thesis describes an investigation of the faintest known proper motion members of the Pleiades star cluster. The primary aim of the work is an attempt to determine whether the lowest mass members of the cluster are brown dwarfs.

A brief introduction outlines the fundamental properties of brown dwarfs and discusses the relation of research in this area to other branches of astronomy. The second chapter describes the basic principles of astronomical photometry and spectroscopy, the instruments used and the methods of data reduction. Chapter three gives a review of the current theory and observations of brown dwarfs.

The results are presented in chapters four, five and six. $RIJHK$ photometry for a sample of 62 objects is presented. The $I, I-K$ diagram is shown to be a good discriminant of binary status for low mass cluster objects and using this diagram two single brown dwarf candidates and seven potential brown dwarf containing binaries are identified. FOS optical spectroscopy of 31 objects is used in an investigation of temperature indicators for cool stars. In addition gravity sensitive features indicate that the surface gravity of the Pleiades objects is lower than equivalent main sequence objects. Also discussed are the chromospheric and coronal activity of cluster members, and evidence is presented showing a turnover in both at $\sim 0.3 M_{\odot}$, where the objects become fully convective. CGS4 1-2.5 micron spectra are used in a futher investigation of methods of determining effective temperature and in searching for evidence of low mass companions. One object shows evidence for a low mass companion of $\sim 0.035 M_{\odot}$.

Chapter seven discusses the evidence from these results that the faintest members observed are brown dwarfs and evidence from other workers that they are not. This chapter also gives suggestions for future work. Appendices compile the theoretical models and data used in the project.

Acknowledgments

Starting from the top... Firstly it is a great pleasure to acknowledge the excellent supervison I have had in the course of this work from Richard Jameson. Richard has been constantly available and was always willing to take the time to explain things to me when I was being a bit dim. In addition he has always been an excellent travelling companion (and source of funds) in our trips both to conferences and observatories around the world, with his 'local knowledge' of both the Canaries and Hawaii proving invaluable on more than one occasion.

Special thanks are also due to Norma Corby for always being avaiable for a chat and sorting out all my admin problems (apparently) effortlessly and Ray McErlean for encouraging me to take the PhD place here and keeping all of our feet on the ground.

The other occupants of the underpass also deserve a mention, so thanks to Paul, Graham, Hassan, Iris, Danny, Kevin & Helen for (if nothing else) putting up with losing so many pens. Also thanks to Simon Hodgkin both for widening my horzions to include X-rays and for providing the X-ray data used in Chapter 5.

Outside the university (but still in Leicester) thanks to some of the occupants of 14 Brookhouse St. over the last three years (namely Ian, Alan & Joanna) for being someone to talk to about things that have nothing to do with astronomy.

Moving further afield, special thanks to Nigel Hambly of Queens University, Belfast both for much useful advice about computing in the early days and many helpful and informative discussions over the last three years. Thanks are also due to Hugh Jones of the ROE for initiating me into the mysteries of CGS4 data reduction.

Worldwide I would like to thank all the people I met at 'The 8th Cambridge Cool Stars Workshop' in Athens, Georgia and 'The Bottom of the Main Sequence

and Beyond' in Garching, Munich for the myriad of useful discussions - there are too many to name, although I have tried to acknowledge them by reference when I can.

Closer to home, I wish to thank all my family, Mum and Dad, my brother John, Grandad and Aunty Evelyn, Uncle Michael and Aunty Margery and Kathleen for all their support (in some cases financial!) which has allowed me to get where I am today.

And finally, thanks to Natasha, for putting up with (and even loving) me for the last two and a half years and generally just being.

Contents

Chapter 1

Introduction

1.1 What is a Brown Dwarf?

Brown dwarfs are objects that lie below the hydrogen burning limit ($\sim 0.08 M_{\odot}$) for stars but are presumed to have formed by the same mechanism as low mass stars (thus excluding planets from the definition). Their existence was first postulated by Kumar (1963), although the name 'brown dwarf' was not introduced until the work of Tarter (1975).

The lack of nuclear fission in the cores of brown dwarfs means that they shine only due to the energy released by their gravitational contraction. Once they have contracted to their degeneracy limited radii, they simply cool and fade. This makes them difficult to detect when young, and impossible to detect (at least by direct observation) once they have cooled.

1.2 ... and why study them?

There are several reasons why there is much current interest in brown dwarfs:

- They can provide important constraints on theories of star formation. Current stellar fragmentation theories predict minimum formation masses ranging from $\sim 0.01 M_{\odot}$ (Boss, 1991) to $\sim 0.08 M_{\odot}$ (Adams, 1994). A determination of the minimum mass actually formed would therefore help determine which of the many competing theories is correct.

- They may provide an important component of the galactic missing mass. It has long been known that the rotational velocity of gas in spiral galaxies as a function of distance from the centre is roughly constant, indicating a significant amount of unseen matter located in the galactic halo. This matter may be baryonic or non-baryonic (Faber & Gallagher 1979, Trimble 1987). If the matter is baryonic, it could be in the form of brown dwarfs. Possible detections of this halo dark matter via gravitational lensing of background objects have been reported by Alcock et. al. (1993) and Aubourg et. al. (1993).

  The question as to whether there is a local missing mass problem as proposed by Oort (1960) is less certain. For example Bahcall (1987) finds evidence for a shortfall of factor ~ 2 in the local mass density from dynamical evidence whereas Gilmore (1993) finds no evidence for any shortfall.

  In addition brown dwarfs may form an important component of cooling flows in clusters of galaxies (Fabian, Nulsen & Canizares, 1991).

- They provide a testbed for the basic physics of degenerate bodies.

- In the words of Burrows et al. (1994) they "lie on one of the last frontiers of stellar astronomy". Their faint nature means they are at the observational limit of modern astronomical instruments. This makes them a natural target for astronomical investigation.

1.3 Project aims and Thesis Structure

This thesis describes the results of observations of the faintest known members of the Pleiades open star cluster. The members are all taken from the proper motion survey of Hambly, Hawkins & Jameson (1991, 1993). The primary aim of the project has been to try and determine whether the faintest ($I \sim 17$) objects detected in the survey were brown dwarfs, or simply very low mass stars. In pursuit of this aim it was found necessary to address other questions, especially those regarding the conversion of theoretical quantities to observables for low mass Pleiads. The approach taken is a multiwavelength one, incorporating both optical and infrared photometry

and spectroscopy. In addition ROSAT EUV observations of low mass Pleiads are considered in conjunction with optical spectroscopy in order to investigate the link between the chromospheric and coronal properties of these objects and the nature of the dynamo driving these signatures of magnetic activity.

In Chapter 2 I describe the basics of astronomical photometry and spectroscopy, the instruments used in the course of the project and the methods employed to reduce the data. Chapter 3 reviews the theory of brown dwarfs, outlines the methods used to convert theoretical quantities to observables and reviews previous searches for brown dwarfs. Chapter 4 describes the basic parameters of the Pleiades cluster. It then describes in detail the results of a programme of infrared photometry of some of the lowest mass members of the cluster, identifying a number of brown dwarf candidates. In Chapter 5 the low mass stars and brown dwarf candidates identified in the previous chapter are investigated using optical spectroscopy. In addition the results of the ROSAT survey of the Pleiades are discussed. Chapter 6 discusses the results of infrared spectroscopy of the low mass objects and uses them in an attempt to determine the true nature of the brown dwarf candidates. Finally Chapter 7 discusses the overall conclusions of the project and gives suggestions for future work in the field.

Chapter 2

Observations, Instruments and Data Reduction

In this chapter I shall discuss the instruments used in this work and the methods used to reduce data from those instruments. The observations reported in this thesis can be conveniently divided into photometry and spectroscopy. The following sections will discuss each of these in turn.

2.1 Photometry

Photometry is the measurement of flux received at the Earth from an object over a specified wavelength range (usually $\sim$ a few hundred Å). It is a basic tool of astronomy and can yield much useful information. A full discussion of the issues involved in photometry is given by Kitchin (1991). Here I will simply give a basic outline of the subject, stressing the practical aspects that need to be addressed in order to carry out 'good photometry', and then discuss the common tools of modern photometry, Charged Coupled Devices (CCDs) and infrared arrays (with particular reference to IRCAM).

2.1.1 Magnitudes, Zeropoints and Airmass

The wavelength range over which photometry is carried out will be determined by the convolution of spectral response of the instrument used, any filters employed and the

transmission of the atmosphere. These factors will be considered in Section 2.1.2 below. The measured fluxes are usually expressed in terms of *magnitudes*. The magnitude scale is a logarithmic and relative scale defined by the equation

$$m_1 - m_2 = -2.5 \log_{10} \frac{I_1}{I_2} \tag{2.1}$$

where m_1 and m_2 are the *apparent* magnitudes of the two stars we are considering and I_1 and I_2 the fluxes in standard flux units (e.g.. $W/m^2/Hz$ or simply counts from a flux measuring instrument) from those stars. Zero magnitude is defined by the star α Lyr (Vega) (see Bessell (1987) for a discussion of the hidden complexities in this apparently simple statement!). The *apparent* magnitude of a star does not take into account its distance, and so is not a measure of its intrinsic luminosity. This is measured by the *absolute* magnitude defined by the equation

$$m - M = 5 \log_{10} d - 5 + A \tag{2.2}$$

where d is the distance of the object in parsecs, M the absolute magnitude, m the apparent magnitude, and A the interstellar extinction to the object. The quantity $m - M$ is known as the *distance modulus*, and is determined by the distance and extinction to the object.

Rearranging equation 2.1 gives

$$m_1 + 2.5 \log_{10} I_1 = m_2 + 2.5 \log_{10} I_2 = ZP \tag{2.3}$$

where ZP is the so called 'zeropoint'. It can be seen that the LHS of equation 2.3 is a function only of the properties of star 1 and that similarly the RHS is a function only of the properties of star 2. Therefore ZP is a function independent of the star observed, and must in fact be a measure of the sensitivity of the instrument/filter/atmosphere combination employed.

Since ZP depends on the atmospheric transmission, it will vary with the height of an object above the horizon. This is because light from an object close to the horizon will have to pass through considerably more of the Earth's atmosphere than light from an object near the zenith. It can be shown (see Bohm-Vitense (1989) for a simple derivation) that due to this effect, ZP will be proportional to $\sec z$ (the

'airmass'), where z is the angle between the object and the zenith, ie.

$$ZP = k \sec z + ZP_{\sec z=0}. \tag{2.4}$$

Because atmospheric absorption is a function of wavelength, the constant k ('the airmass coefficient', measured in magnitudes per unit airmass) will also be a function of wavelength. Unger et. al. (1988) list standard values for k for various wavelengths. However, if observations are made regularly of standards throughout the night at various airmasses, it is possible to derive values of k for the particular night in question. This procedure was used for all of the photometric observations reported in this work.

Note that in practice k will have a weak dependance on stellar colour. This is because the effective wavelengths of filters change slightly with the flux distribution of the object observed. It is therefore desirable to attempt to use standards of similar colours to the objects measured when determining $ZP_{\sec z=0}$ and k.

2.1.2 Filters and Colour Systems

Figure 2.1 shows the transmission of our atmosphere plotted against wavelength in the region $0 - 4\mu$m from data given by Allen (1973). The short wavelength limit at around 0.35μm is caused mainly by increasing molecular (Rayleigh) scattering at shorter wavelengths. In the range $0.35 - 0.7\mu$m, the atmospheric transmission is high and approximately constant. This region corresponds to the spectral response of the human eye (Allen 1973). Above 0.7μm the atmospheric transmission is dominated by deep water vapour bands centered around 1.4, 1.9 and 2.6 μm.

Below one micron, the choice of passbands for filters is dictated more by convention than physics. The U (central wavelength $\sim$ 3650Å), B ($\sim$ 4400Å), V ($\sim$ 5500Å) filter system was established by Johnson & Morgan (1953), and is currently the accepted standard for nearly all observations. In the R and I bands the situation is not so simple. Many competing systems exist, although in this work we shall only be concerned with three: the Cousins (1976) system, the natural photographic system defined by Kodak IIIa-F and IV-N plates with simple glass filters, and the natural CCD system defined by Bessell (1986). The transmissions of these systems

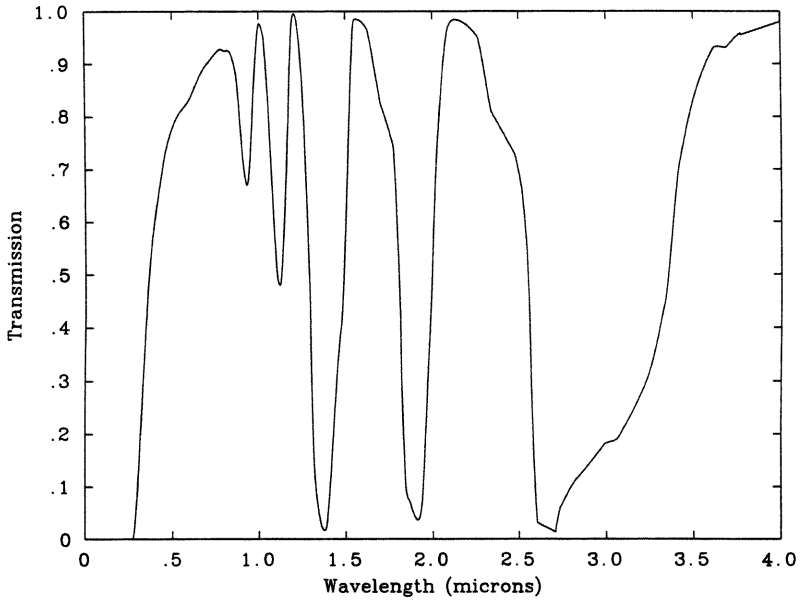

Figure 2.1: Atmospheric Transmission

are plotted in Fig. 2.2 from the data given by Bessell (1986). Note the red tail of the Cousins R band, which extends well into the I band. This is not the case for the other systems. Therefore when measuring R and I band magnitudes for very red stars, where the flux increases rapidly at longer wavelengths, the Cousins system will give results considerably different from the other two. This problem has been addressed in great detail in a series of papers by Bessel (1979, 1983, 1986, 1987). In his 1986 paper he provides equations to transform between the three systems quoted above. Throughout this work I will therefore quote all R and I magnitudes in the 'standard' Cousins system.

The photometric passbands used above 1 micron are mainly defined by the spectral transmission characteristic of our atmosphere, which in this region is dominated by water vapour. From Fig. 2.1 three natural bands in the range 1-2.5 microns are immediately apparent, the J (central wavelength $\sim 1.2\mu$m), H ($\sim 1.6\mu$m), and K ($\sim 2.2\mu$m) bands. Many filter systems have been developed to exploit these three

natural bands. Bessell & Brett (1987) and Leggett (1992) discuss them, and provide transformations between the systems. All of the J,H and K magnitudes quoted in this work are on the UKIRT system.

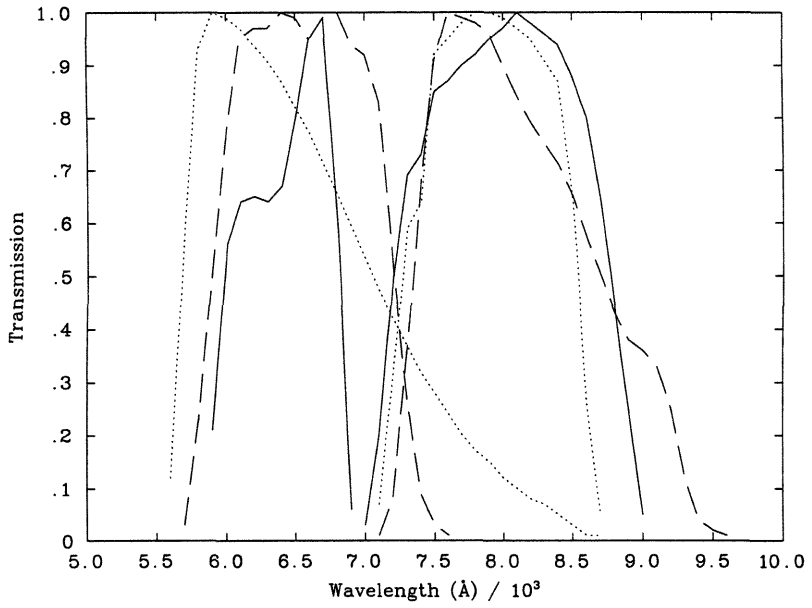

Figure 2.2: R and I Cousins (dotted line), Photographic (solid line) and CCD (dashed line) filter responses.

2.1.3 Charged Coupled Devices

The Charged Coupled Device (CCD) is the basic tool of modern optical photometry. The basic semiconductor physics and methods of construction of these bulk silicon devices is discussed by Yang (1989). The astronomical uses of CCDs are discussed by Kitchen (1991). Here I will simply outline their advantages as astronomical detectors and show the basic method of reduction of CCD data.

CCDs have five principal advantages as a photometric detector.

- They are *imaging* detectors. The relatively large field of view of a CCD means

that even on non-photometric nights, relative photometry between stars on an individual frame may be carried out.

- They are highly *linear* detectors. Therefore photometry may be carried out to a high precision without the difficulty of the removal of non-linear effects.
- They have a very large *dynamic range*. Therefore they may be used to measure stars of vastly differing brightness without resort to neutral density filters etc.
- They have a high *quantum efficiency* over a relatively large spectral region. This high sensitivity allows reduced exposures for bright objects compared with previous detectors and gives an increased potential for the detection of very faint objects.
- They make the best use of good seeing and tracking.

Additional advantages include their discrete pixel nature, which provides information in a natural form for computer reduction and allows their easy control by computerized systems and their relatively stable spectral, sensitivity and spacial characteristics over both short ($\sim$ seconds – minutes) and long ($\sim$ hours – weeks) timescales.

The reduction of a CCD image is a relatively simple process, aided by various computer packages such as FIGARO (Shortridge 1991) and KAPPA (Currie 1992). The steps involved are the following.

- Subtraction of any *bias* and *dark* frames. A bias frame is simply a zero exposure taken to measure the slight electronic bias level deliberately inherent in the CCD electronics. Either a mean bias level may be subtracted, or, if there is evidence of structure in the bias frame, the bias frame may be subtracted off pixel by pixel. Dark exposures of the same length as the image exposures, but with the shutter closed, may also be subtracted off. These serve to measure and subsequently remove any thermally generated charge in the array. With modern, low dark current CCDs, the subtraction of a dark frame is not usually necessary.

- Division by a *flat-field.* A flat field is a frame taken in order to measure the pixel-to-pixel sensitivity variations across the array. It is usually obtained either as a 'dome-flat' by taking a short exposure of the illuminated wall of the dome with the telescope defocused, or a 'sky flat', either by taking a short exposure of the twilight sky or by median filtering many long exposure frames taken over the course of one night. Since pixel sensitivity varies with wavelength, it is necessary to obtain flat-fields in all of the wavebands observed. Division of an image by the flat field (normalised to a mean value of one) will remove the pixel-to-pixel sensitivity variations in the image without affecting the overall array sensitivity.

- Extraction of Counts. Once all of the image frames taken over a night have been reduced, then the counts from the objects and standards observed can be measured. This can be done either automatically using a program such as DAOPHOT (Stetson 1987) or PISA (Draper & Eaton 1992), or manually with a program such as FIGARO (Shortridge 1991).

- Calibration. The zeropoint for the array, and airmass and colour corrections can be calculated from observations of standards as outlined in Section 2.1.1 above. This information, along with relative exposure times, can then be used to calculate magnitudes for the objects of interest within the frames.

2.1.4 Infrared Arrays and IRCAM

Infrared Arrays are the infrared analogue of optical CCDs, and although the physics upon which they are based is considerably different, to the user they appear very much as infrared CCDs. A typical Infrared Array is the IRCAM array mounted on the United Kingdom Infrared Telescope (UKIRT), Mauna Kea, Hawaii. The construction and operation of the camera is described by McLean (1987, 1989).

The InSb array used in IRCAM has 62×58 pixels, compared to the typical $\sim 1000 \times 1000$ pixels of a modern CCD, and so has a rather smaller field of view than the optical CCD. In addition it must be cooled to a rather lower temperature ($\sim 35K$) than an optical CCD. It does however share the basic linearity and

high quantum efficiency of the CCD. The method of data reduction is similar to CCD data, although more care must be taken with the removal of the considerable dark current accumulated by any lengthy exposure. In addition due to the bright nature of the infrared sky, greater care must be taken when subtracting the sky level to obtain the final counts from the object. The bright sky does however have one advantage, making the aquisition of high quality flat-fields by median filtering programme frames very easy.

Guarnieri, Dixon & Longmore (1991) carried out systematic tests of the IRCAM system, and report that the camera is capable of a photometric accuracy of better than 1%. They also show that over a five night period the variation in mean nightly zero point of the array was only 0.03 mag., demonstrating that both the site and camera system are very stable over this period.

In 1994 the IRCAM system was upgraded to a 256×256 pixel array (IRCAM3) and a new array controller (ALICE) installed. This gives both increased sky coverage and a smaller pixel size. In addition the new controller allows the use of 'shift-and-add' techniques to improve spatial resolution.

2.2 Spectroscopy

Spectroscopy is the measurement of the flux from an object as a function of wavelength. This measurement is accomplished by the use of a dispersive element such as a prism or (more frequently) diffraction grating, in conjunction with a position sensitive detector (usually a CCD). The performance of a spectrometer is generally determined by its spectral resolution R, defined by the equation

$$R = \frac{\lambda}{\Delta\lambda} \tag{2.5}$$

where λ is the wavelength observed and $\Delta\lambda$ the smallest wavelength range over which spectral features may be distinguished. R is determined by the optical design of the spectroscope, and a discussion of the factors involved spectroscope design is given by Kitchen (1991). Here I will simply note it is convenient to divide spectroscopes into three classes: Low ($R \sim 500$), Medium ($R \sim 5000$) and High ($R \sim 50000$) resolution.

Low resolution spectroscopes have an important advantage over their higher resolution cousins. Since they have a lower dispersion, the flux falling on any individual detector element will in general be greater than for a higher resolution spectroscope observing the same object. Therefore the exposure time required to obtain an equivalent signal-to-noise ratio spectrum of an object will be much lower using a low resolution spectroscope compared to a higher resolution instrument. In addition they generally give a greater wavelength coverage in a single exposure. Since in general the objects discussed in this work are faint, I will therefore mainly be concerned with the results of low resolution spectroscopy in the following chapters.

When carrying out spectroscopy it is important to be aware of the effects of differential atmospheric refraction. At high airmasses the difference in refractive indices for red and blue light can cause a significant shift in the apparent position of an object in the sky between these colours. This can be enough to move the object out of the narrow (typically $\sim 1 - 2$ arcsec) spectroscope slit at one end of the spectrum. In order to counter this affect, the slit should be aligned so that it runs parallel to the direction of the refraction (i.e. perpendicular to the horizon). This can be achieved by the use of a field rotator. A table of rotator angles (parallactic angles) for various sky positions and wavelengths is given by Fillipenko (1982). This procedure was carried out for all of the optical spectroscopy described in this thesis. It is not necessary for infrared spectroscopy since the effects of differential atmospheric refraction are much smaller at these wavelengths and the spectral coverage generally less.

I shall now briefly describe the design, performance and use of the spectroscopes used in this work (the Faint Object Spectrograph (FOS-II) and the CGS4 near-infrared spectrometer), and the methods of reduction of data from these instruments.

2.2.1 The Faint Object Spectrograph

The FOS-II spectrograph of the WHT is a high-throughput, low dispersion spectrograph, described in detail by Allington-Smith et al. (1989) and Clegg et al. (1992). It covers a wavelength range of 3500 - 9700Å, using a cross disperser to split the wavelength range into two orders. The first order covers 4600-9700Å, and

the 3500-4900Å, with respective dispersions of 8.7 and 4.3Å per CCD pixel. FOS is mounted below the WHT ISIS spectrograph (Clegg et al. 1992) and has its own optics. However it shares some facilities with ISIS, including filters, comparison lamps, autoguider, slit unit and dekker (necessary to keep the 1st and 2nd orders separate on the CCD).

The reduction of FOS data is a relatively complex task, requiring a large number of steps. The STARLINK software package FIGARO (Shortridge 1991) supplies routines to carry out the necessary procedures, and I shall refer to the various FIGARO commands used in the following discussion. The basic procedure for reduction is as follows.

- Order Straightening. The first step in reducing FOS data is to remove the curvature of the spectra introduced by the cross disperser. This may be done using the FIGARO routines SDIST and CDIST. SDIST is used to trace the curvature of the desired spectral order on a well exposed spectrum (usually of a standard) and fit a 10th order polynomial to the trace. CDIST may then be used to straighten the order for all of the spectra taken that night, using the curvature parameters supplied by SDIST.

- Bias Subtraction. Since the FOS CCD array appears to show no bias structure, it is simply necessary to subtract a constant bias value determined by averaging bias frames from the beginning and end of the night. This may be achieved using the FIGARO commands ISTAT and ICDIV.

- Order Extraction. It is useful at this stage to use the FIGARO ISUBSET command to extract only the part of the CCD array which covers the order in question. This saves memory and disk space and leads to lower processing times in the subsequent stages.

- Flat Fielding. The aim of flat fielding is to remove all small scale variations intrinsic to the chip and also any large scale variations in the spatial direction. Large scale variations in the wavelength direction will be removed later in the Flux Calibration stage. To do this one must produce a master flat field frame which maps these variations. This is done using a combination of tungsten (W)

lamp flats and twilight sky flats. The W flats do not use all of the telescope optics and hence will have a different pattern of illumination across the chip than the object frames. The sky flats will have the correct spatial direction structure but contain sky emission lines and so do not map the sensitivity in the wavelength direction correctly. The procedure to be followed in producing the master flat field is therefore as follows.

1. Average the W flats using IADD and ICDIV.
2. Compress the spectrum in the spatial direction using EXTRACT to form a 1D spectrum. Use IXSMOOTH to smooth out any small scale variations in the wavelength (λ) direction, leaving only the large scale λ variation. Use ISXDIV to divide this smoothed spectrum into each row of the averaged W flat. This gives a W flat that contains no large scale λ variations.
3. Repeat the above step for the resulting frame but using YSTRACT rather than EXTRACT and ISYDIV rather than ISXDIV. This will remove all large scale spatial variations from the W flat, which will subsequently form the master flat field.
4. Average the sky flats using IADD and ICDIV and use YSTRACT to compress in the spatial direction. This will produce a spatial direction profile.
5. Use ISYMUL to multiply every row in the W flat resulting from step 3 by the spatial direction profile. This gives the correct spatial variation to the master flat field.
6. Use ISTAT and ICDIV to normalise the master flat field to 1.

The master flat field frame produced by the above procedure can then by divided into all of the object frames using the FIGARO command IDIV.

- Sky Subtraction. The sky will contribute both emission lines and a continuum to the object spectrum which must be removed. The FIGARO command POLYSKY carries out a sophisticated sky subtraction. The routine is told which areas of the array either side of the object spectrum are to be regarded

as sky and fits a polynomial of the desired order in the spatial direction across the array to determine the sky contribution to the object spectrum. It then subtracts off this polynomial, yielding a sky-subtracted spectrum.

- Optimal Extraction. Extraction of a 1d spectrum from the 2d array is a two stage process. The FIGARO command PROFILE will determine the nature of the spectrum's spatial profile. Due to seeing effects and diffraction by the spectroscope slit, the flux from an object will in general cover more than one CCD pixel in the spatial direction. If the imaging detector is not perfectly aligned with the spectroscope optics, then the shape of this profile will vary in the wavelength direction. PROFILE accounts for this by allowing the derived profile to vary smoothly along the array as a polynomial of the desired order. The OPTEXTRACT command then extracts from each row of the spectrum a contribution to the final 1d spectrum proportional to the spatial profile for that row, thus minimizing the noise contribution from rows that only contain a small amount of signal.

- Wavelength Calibration. The FIGARO routine ARC is an interactive program which will plot the CuAr spectrum generated by the FOS arc lamp and allows the user to identify the various lines. It will then generate a dispersion curve, calculate the rms deviation of the arc lines from that curve, and display the fit graphically. The order of the dispersion curve is selectable by the user. It was found that for FOS spectra then first order (*i.e.* linear) fits were sufficient and appropriate. The output from ARC can be used to calibrate the object spectra using the XCOPY command. In Figure 2.3 I plot the approximate relation between CCD pixel number and wavelength for the first order of the spectrograph, derived from the dataset described in Chapter 5. This information is not available in the WHT control room, and is given here as an aid to quick data interpretation at the telescope.

- Extinction Correction. The EXTIN command will correct spectra for atmospheric extinction due to varying airmass, using the extinction tables provided

with the FIGARO package. For FOS spectra, the appropriate extinction table is 'lpoext', which contains the values for the La Palma site given by King (1985)

- Flux Calibration. The method of FIGARO flux calibration, using so called "spiketra" to define the flux of spectrophotometric standards is discussed at length by Shortridge (1991), and need not be repeated here. The basic method however, is to produce from an observation of a standard and the tables of standard fluxes given by Oke & Gunn (1983) a calibration spectrum for the observations, which maps the variation in sensitivity with wavelength of the spectrograph. This calibration spectrum is then multiplied by the observed spectra to yield calibrated object spectra.

- Water Removal. Above around 8500Å, the dominant source of atmospheric opacity affecting spectra is water vapour. This may be removed providing observations of so-called 'water-stars' are taken regularly during the night. Water-stars should have featureless spectra in the near-infrared, so as to simply map the water vapour absorption in this region. Water-stars are therefore typically of spectral type B. The spectrum of the water-star is divided by a smoothed polynomial to removed large-scale wavelength variations and then normalised to one. This flattened, normalised water spectrum is then divided into the object spectra to remove the water absorption.

The result of this reduction process should be a set of uniformly reduced spectra, calibrated in units of F_ν (mJy). The spectra can be converted to units of F_λ or AB-Magnitudes (Oke & Gunn 1983) using the FIGARO routines FLCONV and ABMAG. The calibration cannot be regarded as truly spectrophotometric unless a very wide slit (accepting all the starlight) is employed. However this will generally compromise the spectral resolution, as a wider slit gives a lower resolution.

2.2.2 The CGS4 Near-Infrared Spectrometer

The CGS4 cooled grating spectrometer was designed and built at the Royal Observatory, Edinburgh. Its design is described by Mountain et al. (1990) and Wright et

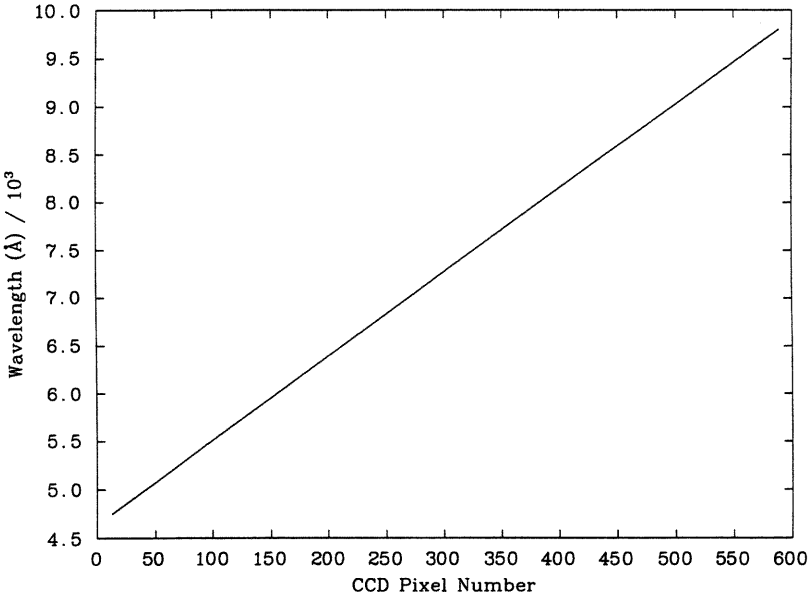

Figure 2.3: WHT FOS Wavelength Calibration

al. (1993) who also give sensitivity figures and describe some of the science achieved with the instrument during its first two years of service on the United Kingdom Infrared Telescope (UKIRT). It provides spectral coverage from 1 to 5μm and is equipped with a 58×62 infrared array similar to that used in IRCAM. The array is currently being upgraded to a 256×256 model. It provides resolving powers in the range 300-20000 by means of two internal gratings, mounted back to back, and pixel scales of 1.5 or 3.0 arcsec/pixel using interchangeable camera optics. The optical elements are cooled to about 77K and the detector to around 35K. Spectra may be oversampled by stepping the detector with a resolution of 1/10 of a pixel over a total range of 2.5 pixels. The spectrometer operates in first order beyond $\sim 1.6\mu$m, and second order below this wavelength. At first order the spectral coverage obtained with the 58×62 array and the short focal length (75 mm) camera is $\sim 0.4\mu$m and $\sim 0.2\mu$m at second order. Therefore to cover $1-2.5\mu$m requires six grating positions in total (three first order and three second order). These grating positions should

be chosen with care to give generous overlaps which are in regions not affected by poor atmospheric transmission.

Data from the array is partially reduced at the telescope using the CGS4DR software (Puxley et al. 1992). This removes bad-pixels, debiases, flat fields, linearity corrects and interleaves oversampled scan positions and writes the resulting 'Reduced Observations' to disk. The raw data is also written to disk in the form of 'Integrations' and 'Observations' so that the above processes may be repeated if necessary at a later date. The 'Reduced Observations' consist of observations in the order 'object - sky - sky - object', where the telescope pointing is offset $\sim$ 25 arcsec between 'object' and 'sky' observations. Since the array can resolve in the spatial direction, the 'sky' observations also contain a spectrum of the observed object, but located on a different set of detector rows that the 'object' observations. This procedure maximises observing efficiency, since no time is wasted looking at 'blank' sky. Also at the telescope the 'object - sky' pairs can be subtracted and the resulting sky subtracted images stacked into a so-called 'Reduced Group'. This Reduced Group can be displayed in real time at the telescope, allowing the observer to judge when enough integration time has passed to obtain a sufficiently good signal-to-noise ratio.

The subsequent stages of data reduction are best carried out using FIGARO. A comprehensive guide to this process is given by Bailey (1991). The steps involved are:

- Sky Subtraction. For CGS4 data this is a two stage process. Firstly 'object - sky' pairs are subtracted using the FIGARO routine ISUB. Any residual sky emission is then removed using POLYSKY as described in section 2.2.1.

- Optimal Extraction. The process is basically the same as described previously for FOS data, the profile for the individual Reduced Observations being derived from the Reduced Group in order to improve its signal-to-noise ratio.

- Derippling. Because CGS4 spectra are normally scanned through two or more positions to provide full sampling, it is possible to get a periodic ripple on the spectrum due to seeing, windshake or transparency variations during the scan. The FIGARO program IRFLAT can be used to remove this ripple. This

routine takes a section of spectrum which can be assumed to be flat and folds the data over this region to determine the shape and amplitude of the ripple and output a pure ripple spectrum. This ripple spectrum can then be divided into the original spectrum to remove the ripple.

- Wavelength Calibration. The CGS4 spectrometer contains argon, krypton and xenon lamps. For low resolution spectroscopy the argon lamp is the most useful, having a large number of lines in the region 1-2.5μm. The FIGARO ARC program as described in section 2.2.1 may be used to carry out the calibration.

- Flux Calibration. For CGS4 spectra flux calibration is done using observations of a star with a featureless black-body spectrum in the infrared. An A type star is typically used, the Hydrogen recombination lines in the spectrum being well determined and easy to interpolate over using the FIGARO command ISEDIT. The FIGARO routine IRFLUX divides the observed spectrum by the standard spectrum, and then multiplies the result by a black body spectrum appropriate to the spectral type of the standard. This procedure removes any response variations in the object spectrum due to both the instrument/telescope combination and any variations in atmospheric transmission due to airmass effects and other atmospheric absorptions (especially terrestrial water vapour). The spectrum is then calibrated absolutely in units of F_ν using a spot magnitude for the standard.

The various spectral fragments produced by this procedure may then be joined together, using the overlapping regions to scale the spectra to each other. The final spectrum may then be spectrophotometrically calibrated using JHK photometry (if available) in conjunction with filter profiles and zero-points from Bessell & Brett (1988).

2.3 Conclusions

I this chapter I have outlined the various instruments used during the course of this work. The great advances in the quality, size and sensitivity of the detectors used in these instruments over the last decade (especially in the infrared) mean that for the first time we have a real chance to detect, identify and investigate faint, cool objects such as very high redshift quasars, distant molecular clouds and, of course, brown dwarfs.

In addition I have given the basic method for reducing data from these instruments. In many cases it is possible to automate many of the stages in this reduction, using script control languages such as ICL, DCL or the unix c-shell, or by more direct manipulation of the data using FORTRAN or C. However no details of these script files and programs have been given as the purpose of this chapter has been to outline techniques rather than discuss technicalities.

Chapter 3

A Short Review of Theory and Previous Work

There have been several reviews of progress in both theoretical and observational work on brown dwarfs. Of particular note are those by Liebert & Probst (1987), Stevenson (1991) and Burrows & Liebert (1993). In this chapter I will draw on the material from these reviews and also from recent publications in order to give an overview of the current standing of research in the field.

3.1 The Theory of Brown Dwarfs

Very low mass stars ($M < 0.3M_{\odot}$) and brown dwarfs are, to first order, the easiest stars to model. They are completely convective throughout and therefore can be well represented by n=3/2 polytropes. Kumar (1963) used this property, combined with an equation of state that took into account non-relativistic degeneracy to show that the onset of degeneracy could prevent nuclear reactions below a mass limit of $\sim 0.07 - 0.09M_{\odot}$. Burrows & Liebert (1993) show that such an analysis allows the derivation of the most pertinent features of brown dwarfs. They have radii $R \sim 0.1R_{\odot}$, central densities in the range 10 gm/cm^3 to 1000 gm/cm^3 and central pressures around 10^5 MBar. They add to this analysis a knowledge of opacities, phases, specific heats and a boundary condition. They are then able to derive

analytic expressions for the effective temperature and bolometric luminosity of brown dwarfs as a function of time, mass and K_R, the Rosseland mean opacity:

$$T_{eff} = 1551K(\frac{10^9 yr}{t})^{0.324}(\frac{M}{0.05M_\odot})^{0.827}(\frac{K_R}{10^{-2}})^{0.088} \quad (3.1)$$

$$L_{bol} = 3.82 \times 10^{-5} L_\odot(\frac{10^9 yr}{t})^{1.297}(\frac{M}{0.05M_\odot})^{2.641}(\frac{K_R}{10^{-2}})^{0.35} \quad (3.2)$$

These equations encapsulate the analytic theory of brown dwarfs and are, in the words of Burrows & Liebert (1993) 'surprisingly accurate, given the assumptions they employ'. They find that they predict temperatures and luminosities to better than 35% as compared to the more accurate numerical models of Burrows et. al. (1993).

In the 1970's and 80's the advent of computer codes capable of modelling stellar interiors allowed more sophisticated numerical models to be constructed. The input physics into such models are:

- The standard equations of stellar structure.
- An equation of state and the thermodynamics of metallic hydrogen.
- Nuclear reaction cross-sections and rates appropriate to brown dwarf temperatures and pressures.
- A surface boundary condition.

Burrows & Liebert (1993) show that it is the surface boundary condition that controls the evolution of a brown dwarf. Unfortunately this is the only area of brown dwarf physics which is not yet well understood. The cool temperatures of brown dwarf atmospheres ($300 - 3000K$) mean that many complex and unusual molecular and atomic species are present. This introduces considerable uncertainties into the surface opacities and hence the brown dwarf structure. Efforts are being made to construct model atmospheres (Allard 1990, Saumon et al. 1994) to overcome this problem.

The basic features of the numerical models are summarised in Figure 3.1, taken from Nelson, Rappaport & Joss (1986). In this figure are plotted Luminosity, Radius

and Effective Temperature as a function of time for objects of masses ranging from 0.10 down to $0.01 M_{\odot}$. The important features of the evolution are as follows:

- Before $\sim 10^6$ years the objects evolve at constant T_{eff}, their radius and hence luminosity decreasing as they contract under the influence of gravity down the 'Hayashi track'.
- Between $\sim 10^6$ and $\sim 3 \times 10^6$ years the objects attain a constant radius, T_{eff} and luminosity. During this time they are burning the small fraction of deuterium in their core, and are said to be on the 'deuterium main sequence'.
- After $\sim 3 \times 10^6$ years all of the central deuterium is burnt and gas pressure is again insufficient to maintain hydrostatic equilibrium. The objects begin to contract again.
- At $\sim 5 \times 10^8$ years a bifurcation occurs. The $0.10 M_{\odot}$ object contracts enough to reach a central temperature of $\sim 3 \times 10^6 K$, sufficient to initiate hydrogen burning via the p-p chain. By contrast the central temperature and density in the lower mass objects of $0.08 M_{\odot}$ and below (the 'brown dwarfs') never reach the critical values necessary to start hydrogen burning. They are prevented from reaching these values by the onset of electron degeneracy, which limits their radii and stops the contraction. They therefore simply cool and fade at constant radius.

Many groups have calculated theoretical models of low mass stars and brown dwarfs, all of which have the essential features mentioned above, but which differ in the exact numerical values of luminosity and temperature at a given time. Luminosities and Temperatures for all of the models used in this work are listed in Appendix A.

In the absence of any method of evaluating the various models, their accuracy can best be judged by intercomparison. Fig. 3.2 therefore plots the most recent theoretical models from Nelson, Rappaport & Joss (1993) (crosses), Stringfellow (1991) (octagons), Burrows et al. (1993) (squares) and D'Antona & Mazzitelli (1994) (stars). The models are all for solar metallicity, the Pleiades age of 70 Myr (Section

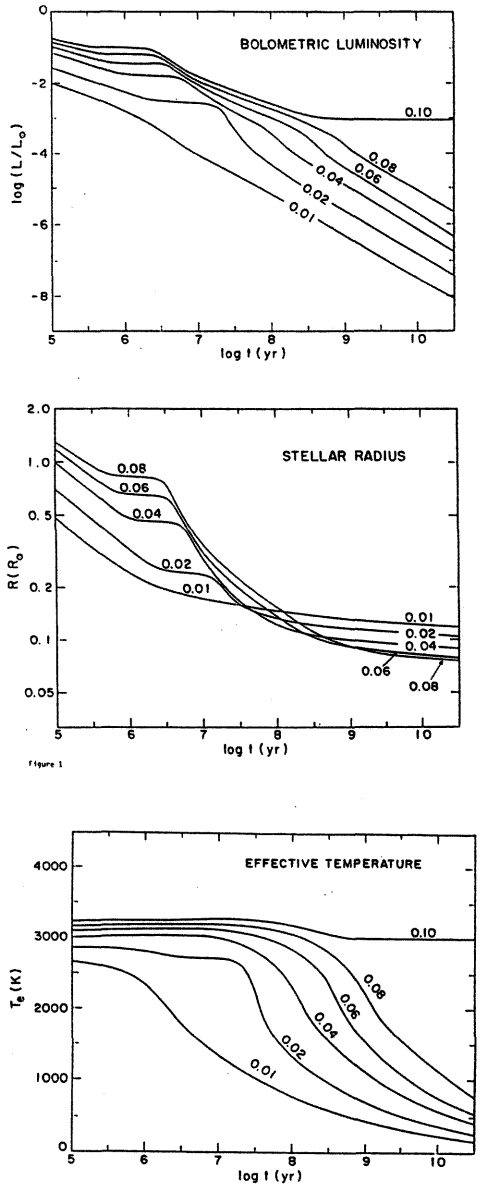

Figure 3.1: Luminosity, Radius and Effective Temperature as a function of time for objects from 0.10 to 0.01 $M_\odot$ (reproduced from Nelson et. al. (1986).

4.1.1) and are plotted for the masses 0.20, 0.15, 0.10, 0.09, 0.08, 0.07, 0.06, 0.05, 0.04 and $0.03M_{\odot}$ (except for the Nelson et al. model which extends only to $0.04M_{\odot}$). Note that there is considerable agreement between the models in the general location of the objects at the low mass end, although there are still large disageements about the exact masses of these objects. At higher masses the models diverge more, due mainly to differing treatments of convection and Coulomb forces. The most *conservative* model (i.e. the one that places the brown dwarf limit at the lowest luminosity) is that of Stringfellow (1991). I shall therefore generally prefer this model in the chapters that follow, since anything this model predicts is a brown dwarf, the others all agree on.

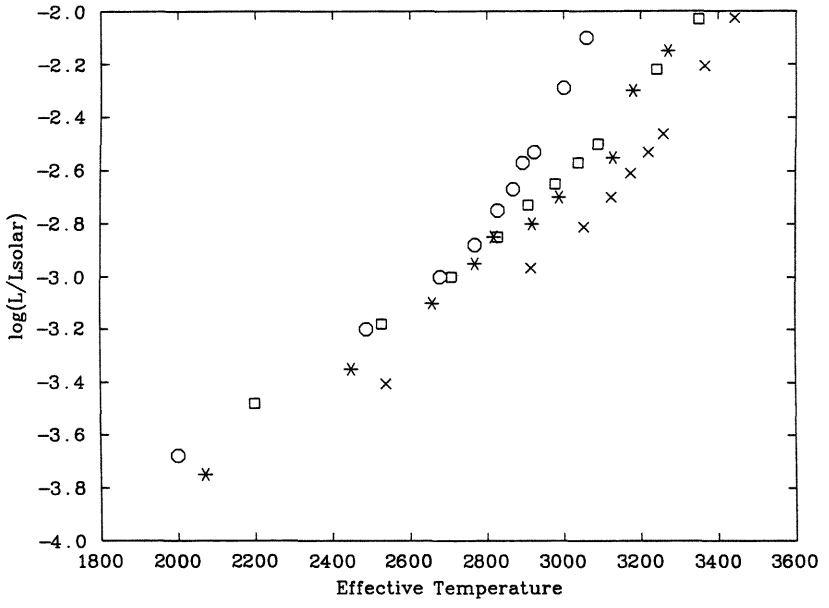

Figure 3.2: A comparison of recent theoretical models.

3.2 Temperature Scales and Bolometric Corrections

The theoretical models discussed above yield their results in terms of effective temperatures and bolometric luminosities. Conversion of these quantities to observable colours and magnitudes requires the use of temperature scales and bolometric corrections. This task is made difficult by the nature of cool stellar atmospheres which, as already noted, contain mainly atomic and molecular features. In the 0.6 - 2.2 micron region a 3000K object will emit over 70% of its flux. This region of the spectrum is heavily contaminated by water vapour absorption and this means that simple black body assumptions to derive T_{eff} and L_{bol} are inappropriate and other more sophisticated methods must be employed.

The best method of deriving temperatures for cool stellar objects will undoubtably be model atmosphere fitting. In the last few years considerable progress has been made in the field of modelling these atmospheres, especially by Allard (1990). Allard (priv. com) has kindly made several of these model atmospheres available. In Figure 3.3 I plot her model atmospheres for $T_{eff} = 3200, 2800$ and $2400K$ at $\log g = 5.44$. The strong temperature dependance of the atmospheres, especially with regard to water vapour above 1.3 microns is immediately apparent. In Figure 3.4 I plot her atmospheres for a constant $T_{eff} = 2400K$ but for $\log g = 5.14, 4.44$ and 3.74. Very little difference is apparent between the figures, although some individual line strengths are altered (e.g. NaI). No effects can be seen in the water vapour bands since at present the models here use laboratory derived opacities rather than theoretical oscillator strengths. This illustrates the current problem with the model atmosphere approach. Allard (1994) states that a full theoretical treatment of several of the most important opacity sources is still some way away. However progress is being made rapidly, and within the next few years the quality of the atmospheres will improve to the point where they do become the best method of T_{eff} determination. Until then simpler methods of temperature determination must be employed, and it is these I shall discuss for the remainder of the section.

I shall therefore compare the three most recent empirical temperature scales (and

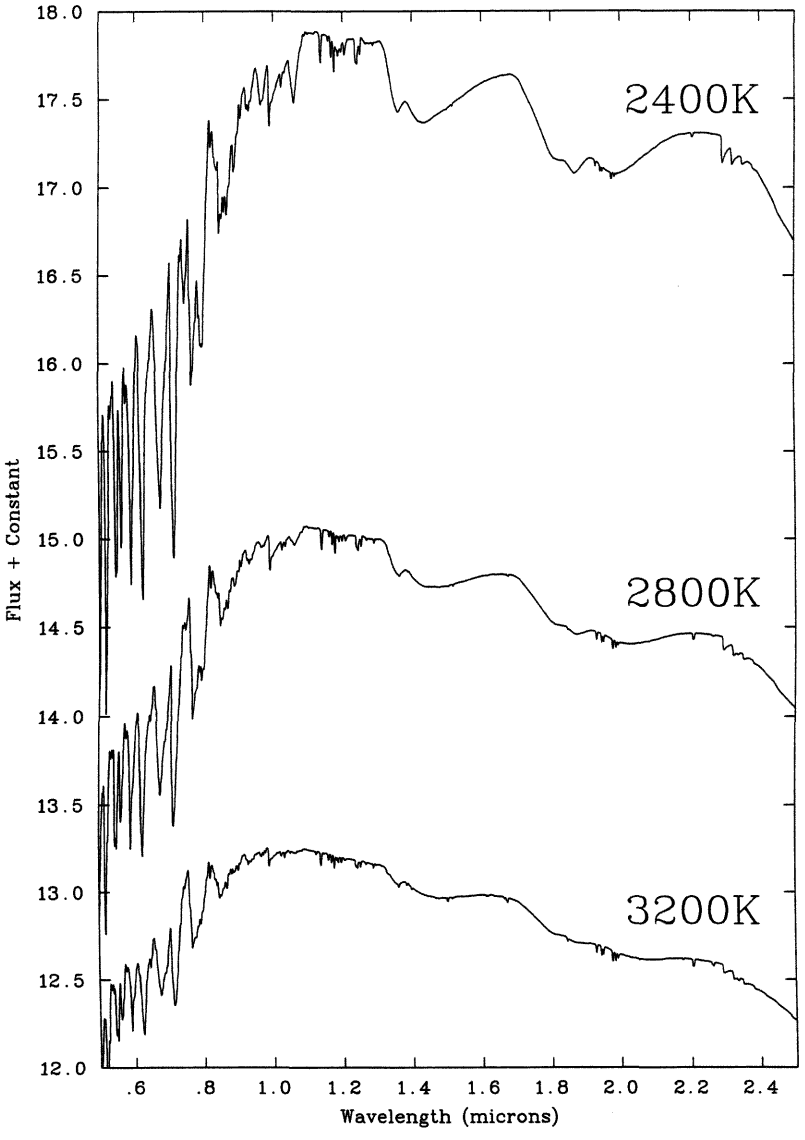

Figure 3.3: Model Atmospheres for various T_{eff} (supplied by Allard (priv. com.))

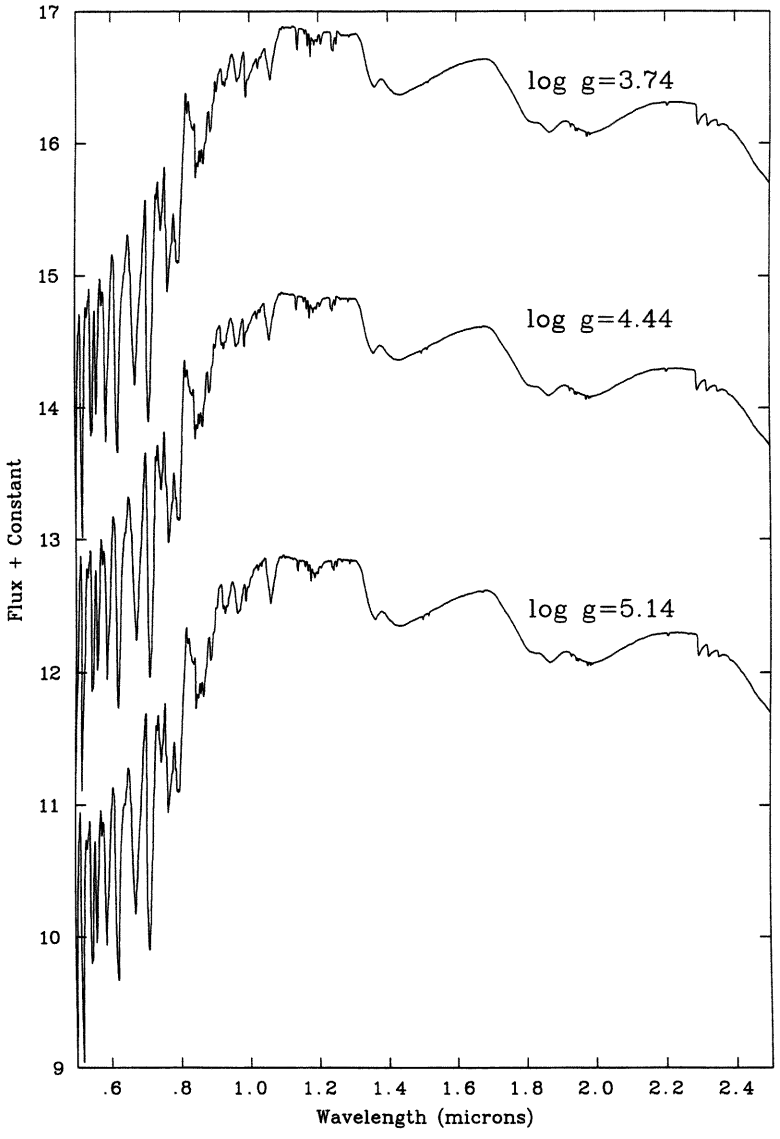

Figure 3.4: Model Atmospheres for various $\log g$ (supplied by Allard (priv. com.))

associated bolometric corrections). These are the scales of Bessell (1991 - B91), Berriman, Reid & Leggett (1992 - BRL92) and Jones et. al. (1994 - JLJM94).

B91 is an empirical scale based on the Sun, two binary systems for which fundamental temperatures can be determined (YY Gem and CM Dra), and a large sample of low mass stars for which temperatures are determined by black body fits to broad-band colours. Bolometric magnitudes and colours are derived by observation and a temperature scale and bolometric corrections thereby constructed. BRL92 show that the black body assumption in this method is probably inappropriate. However, the combination of the B91 temperature scale and the theoretical models of Stringfellow (1991) was shown by B91 to fit the old M-dwarfs well, whereas the BRL92 scale gives temperatures that are too cool by $\sim 200 - 300K$.

BRL92 is an update of the temperature scale of Berriman & Reid (1987). The method is to match the flux under a black body anchored at K (2.2 microns) to the total bolometric observed flux derived spectroscopically. JLJM94 show this is equivalent to solving the equation

$$C\frac{f_{2.2}}{f_{bol}} = \frac{F_{2.2}(T_{eff})}{\sigma T_{eff}^4} \tag{3.3}$$

where $f_{2.2}$ and f_{bol} are the measured 2.2μm and bolometric fluxes respectively, with the constant $C = 1$. However JLJM94 show that for stars with significant steam absorption, $C < 1$ (i.e. 2.2 μm not a continuum point), and they believe this invalidates the temperature scale, as it leads to derivation of temperatures systematically lower than the 'true' T_{eff}.

The method of JLJM94 is the most sophisticated and the explanation here is adapted from that given in their paper. It is based on the strength of the infrared water absorption bands which the theoretical models from Allard (1990) show to be the dominant opacity source beyond 1.34 μm. The oscillatory nature of the water vapour opacity (see Figure 3.5) means that at several wavelengths through the spectrum it will have the same value for a given temperature, corresponding to points of equal optical depth. Fitting a black body through these points generates a fit temperature T. Using this T the constant opacity wavelengths can be refined and the fit repeated, obtaining a better estimate of T. This process can obviously be iterated until the best estimate of T is obtained. T is *not* the effective temperature,

since it is not measured at optical depth $\tau \sim 1$. However, using T it is possible to calculate the ratio $\frac{R^2}{d^2}$ from the equation

$$f_\lambda = \frac{R^2}{d^2} F_\lambda(T) \tag{3.4}$$

where f_λ is the measured flux at one of the constant opacity wavelengths, R the radius, d the distance and $F_\lambda(T)$ the Planck function. The effective temperature can then be determined from the bolometric flux f_{bol} using

$$\sigma T_{eff}^4 = \frac{d^2}{R^2} f_{bol}. \tag{3.5}$$

The T_{eff}'s derived from this method for a selection of low mass stars are then combined with photometry to define the temperature scale.

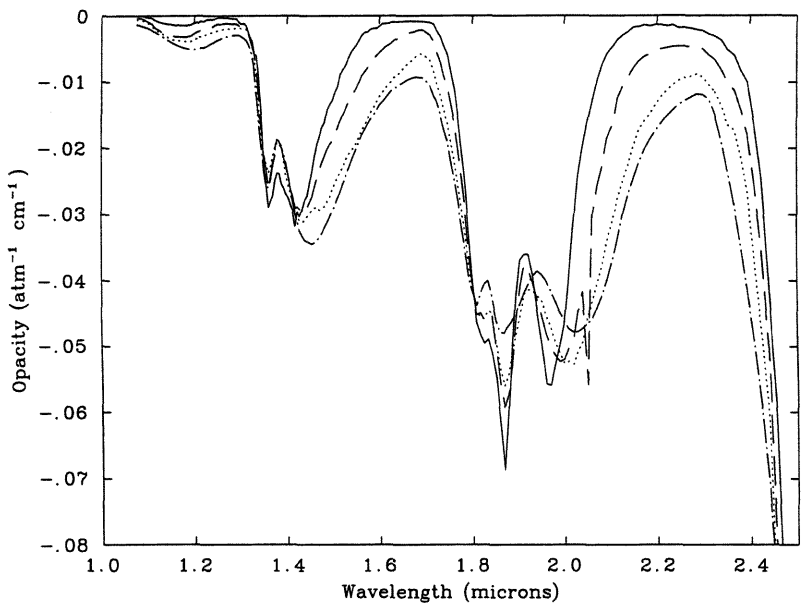

Figure 3.5: Water Vapour Opacity as a function of Wavelength for $1500K$ (solid line), $2000K$ (dashed line), $2500K$ (dotted line) and $3000K$ (dot-dash line). Data from Ludwig (1971).

Fig. 3.6 therefore shows the $R - I, T_{eff}$ relations of B91 (squares), BRL92

(crosses) and (JLJM94) (octagons). Similarly Fig. 3.7 shows the $I-K, T_{eff}$ relations. In both cases the same general feature is apparent, namely B91 giving temperatures $\sim 300K$ hotter than BRL92 for a given colour, with JLJM94 lying somewhere between the two. In terms of identifying brown dwarf candidates, B91 will therefore be the most conservative of the three scales. For this reason I shall in general prefer this scale in the following chapters. I shall also return to the question of temperature scales in Chapter 6.

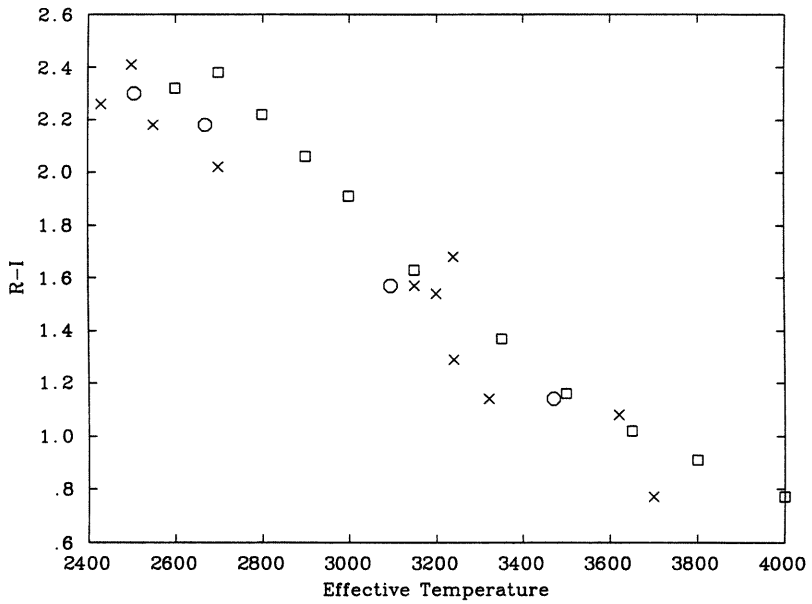

Figure 3.6: $R-I, T_{eff}$ scales from B91 (squares), BRL92 (crosses) and JLJM94 (octagons)

Figure 3.8 shows the I band bolometric corrections ($BC_I = m_{bol} - m_I$) as a function of (a) T_{eff} as derived by the various authors and (b) $I-K$. Note that the large scatter in (a) is caused by the relatively large uncertainties in the derived temperatures. Comparison with (b) shows that in terms of measured colours, BC_I is well determined, with little disagreement between the authors. In this thesis the

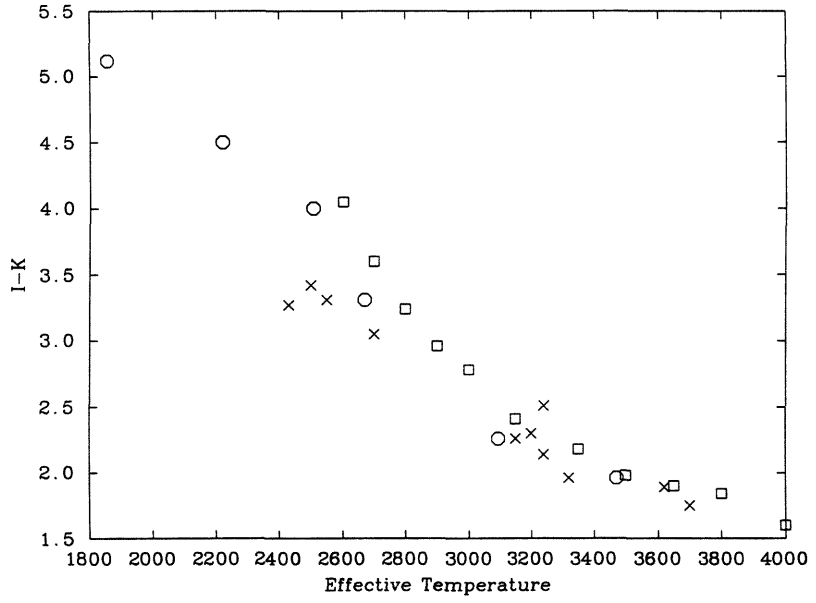

Figure 3.7: $I-K$,T_{eff} scales from B91 (squares), BRL92 (crosses) and JLJM94 (octagons)

bolometric corrections of B91 will therefore be used. However using the alternative scales would not change any of the conclusions significantly.

3.3 Luminosity and Mass Functions

The luminosity function (LF) of a stellar population is defined as the number of stars per unit luminosity interval. It is often expressed in terms of the number of stars per unit M_V per cubic parsec. For cooler objects however it is better to use M_R, M_I or even M_{bol}.

The mass function (MF) of a stellar population is defined as the number of stars per unit mass interval. It may be determined from the LF if a mass-luminosity relationship is available by the convolution of the two:

$$N(m) = LF_\lambda \frac{dM_\lambda}{dm} \tag{3.6}$$

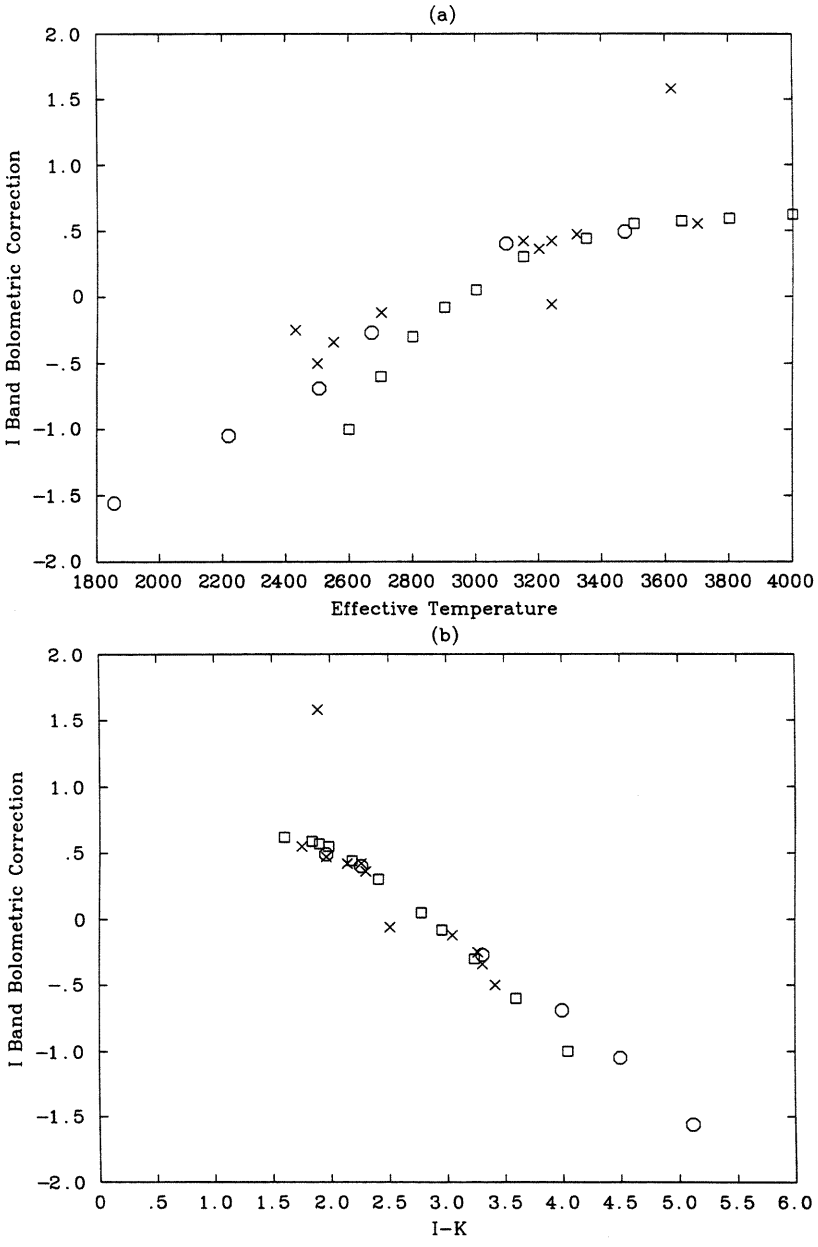

Figure 3.8: BC_I as a function of (a) derived T_{eff} and (b) $I - K$ colour. Labels are B91 (squares), BRL92(crosses) and JLJM94 (octagons)

In this formula $N(m)$ is the mass function, $\frac{dM_\lambda}{dm}$ the mass-luminosity relationship and λ the photometric passband employed.

Many attempts have been made to determine the luminosity and mass function of the field. For higher mass objects ($\sim 0.4M_\odot$ and greater) Salpeter (1955) found a power law for the number of stars per unit mass interval:

$$\frac{dN}{dm} = 0.013m^{-2.35}. \tag{3.7}$$

Below $0.4M_\odot$ the situation is more controversial. Determinations of the LF become hampered by incompleteness problems and uncertainties in the mass-luminosity relationship for the lower mass objects. D'Antona (1994) shows that much of the structure found in the LF is a result of 'kinks' in the mass-luminosity relationship due to various opacity sources becoming predominant in the cool M-dwarf atmospheres. Unless an accurate mass-luminosity relationship is employed, these kinks will propagate into the mass function and lead to incorrect conclusions as to its behaviour at the low mass end. Kroupa, Tout & Gilmore (1990,1991) also examined these effects and find that a MF power law with an index change at $\sim 0.5M_\odot$ fits observations of the field LF. Reid (1994) disputes this, claiming their analysis is flawed. Other determinations of the field LF (and hence MF) have been carried out by Hawkins & Bessell (1988) and Leggett & Hawkins (1988), who find a peak in the LF at $0.2M_\odot$. The LF then falls reaching a minimum at around $0.1M_\odot$ and then appears to begin to increase again.

Proper motion surveys and number counts allow LFs to be constructed for open clusters. This has been done by various groups for a selection of clusters. The first deep survey of the Hyades cluster was carried out by Leggett & Hawkins (1988). Leggett et al. (1994) updates this work, also incorporating the results of proper motion surveys by Reid (1992, 1993) and Bryja et. al. (1992, 1994) and finds a MF power law index of between 0 and -1 to be consistent with the data at the low mass end.

The Pleiades MF has been extensively studied. At high ($> 0.7M_\odot$) masses work carried out by van Leeuwen (1970) established that a power law with index -2.7 represented the cluster MF well (similar to the Salpeter (1955) value for the field). The MF has subsequently been pushed down to the region of the hydrogen burning

limit by the work of Hambly, Hawkins & Jameson (1991,1993). The cluster MF they derive is shown in Figure 3.9 (top). In this figure the solid points correspond to a Pleiades age of 70 Myr and the dotted points to an age of 100 Myr. The higher mass MF from van Leeuwen (1980) is shown by crosses and the solid line. The cluster MF has a near flat appearance at the faint end of this log-log plot, corresponding to a power law index of -1.0. The MF of Praesepe has also been studied by this group (Hambly et. al. 1994a,b) and is plotted in Fig. 3.9 (b). The MF determined here appears similar to that derived for the Pleiades, with a power law index of -1.3 at the low mass end.

A group lead by Richer & Fahlman (Drukier et. al. 1988, Fahlman et. al. 1989, Richer et al. 1990, Richer et. al. 1991) have investigated the LF and MF of galactic globular clusters. They find that some (and perhaps all) of the clusters have very steep mass functions, with slopes of ~ -2.5 or greater down to masses of $\sim 0.15 M_{\odot}$. Extrapolation of this mass function into the brown dwarf regime would imply that a significant fraction of the mass of globular clusters is in the form of brown dwarfs. Note this power law is far steeper than any of the other (population I) low mass power laws found in the local field or open clusters. In a later paper (Richer & Fahlman 1992) they measure the LF and MF of the galactic halo using very deep CCD frames. In this other population II sample they also find a very steep MF slope (~ -3.5) down to a similar mass limit. It therefore appears that while low mass stars and brown dwarfs are not a dominant, or even substantial, component of population I, they may be very significant for population II. This has important implications for studies of low mass star formation and proto-stellar cloud fragmentation.

3.4 Brown Dwarf Searches

3.4.1 Searches in the Field

Perhaps the most obvious way to search for low mass objects is simply to look for low luminosity, cool objects in large scale surveys of the field. Unfortunately their is no direct way to measure the mass of an individual field object. In addition their ages can not be determined precisely, but only estimated from their space motions,

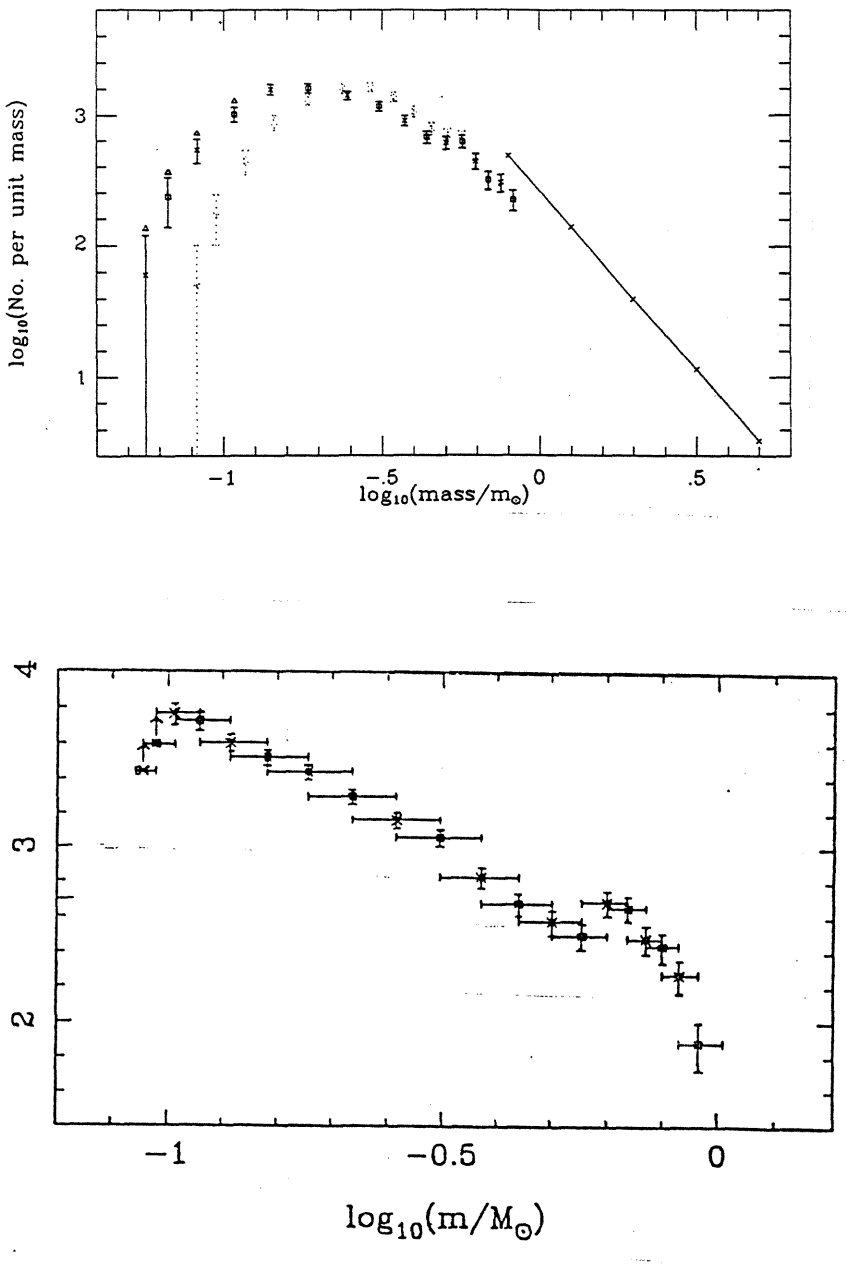

Figure 3.9: The mass functions of (top) the Pleiades and (bottom) Praesepe derived by Hambly et. al. (1991, 1994b). See text for details.

rotation rates and any evidence of surface activity. Using the age estimate, along with a temperature and bolometric luminosity estimated from broad-band colours (Section 3.2) allows a comparison to be made with theoretical models (Section 3.1).

In practice the results of such a comparison are generally unclear. Fig. 3.10 (from Jones, Miller & Glazbrook 1994) plots various low mass stars and brown dwarf candidates . Also plotted on this figure are the 0.6 and 10 Gyr models of Burrows et. al. (1993). The effective temperatures and luminosities were derived using the method of Jones et. al. (1994, also Section 3.2). Note how the classification of an object as stellar or substellar is a very strong function of age, and that age can not be determined by the position of an object on this diagram as the theoretical isochrones lie very close together.

The most recent (and most promising) field brown dwarf candidates discovered are those of Jones, Miller and Glazebrook (1994) and Hawkins (1994). The first of these (JMG 0918 -0023B) is the binary companion of an M dwarf found in a deep K band survery carried out by Glazebrook et. al. (1993). It has comparable colours to GD165B (see 3.4.2). The candidates of Hawkins (1994) are based on digital stacking of a large ($\sim$ 60) number of plates of ESO field 287, giving a survey of 25 square degrees down to limits of $R \sim 23, I \sim 21.5$. 50 objects with $R-I > 3$ were detected and several with $R-I > 4$. Follow up spectroscopy of one object (DO4) confirms a very cool temperature. The faintest of these objects have estimated $M_I \sim 18.5$ and are therefore good brown dwarf candidates.

3.4.2 Searches for Binary Companions

A search for brown dwarfs as binary companions to higher mass objects has several advantages over searches in the field. Such searches may be carried out astrometrically, by high-resolution imaging techniques, by infrared imaging or spectroscopically. Astrometric techniques in which both objects may be observed, such as those using speckle imaging techniques (e.g. Henry et al. 1992) have the potential to directly measure dynamical masses and therefore hold out the prospect of discovering brown dwarfs without the uncertainty that comes from photometric mass determinations.

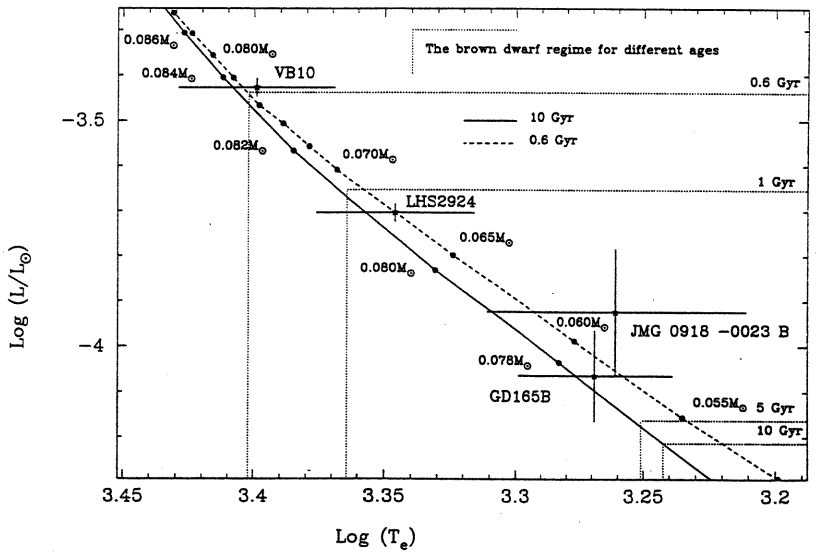

Figure 3.10: Comparison of various low mass objects with theoretical models (from Jones, Miller & Glazebrook 1994).

In the past their have been several spurious claims to have detected brown dwarfs using astrometric techniques (e.g. Barnard's Star by Van de Kamp (1977, 1981) refuted by Heintz (1978) and Wolf 424 by Heintz (1989) refuted by Marcy (1994)). Systematic searches with considerably more accuracy than the previous surveys are now being undertaken by several groups. Marcy (1994) reviews the work of these groups and notes that these surveys have yet to discover any bona-fide brown dwarf companions.

Infrared imaging provides another method of searching for low mass (and hence cool) companions. Infrared imaging surveys of nearby M-dwarfs have been carried out by Jameson et. al. (1983), who found no companions and Strutskie et. al. (1989), who found one potential brown dwarf companion, Gliese 569B, although they conclude that the object could also simply be a very low mass star. Rieke & Rieke (1990) surveyed all known stars within 8 pc of the sun north of a declination

of -20 degrees and fainter than $M_V = +11$ (i.e. early M spectral type and later) down to K=15.5. No plausable brown dwarf candidates were found.

Probst & Liebert (1983) realized that if the primary object was a white dwarf rather than an M-dwarf then low mass stellar companions and cool brown dwarfs might be detected in the infrared. Using JHK photometry they failed to find any companions in surveys of around 100 white dwarfs. Zuckerman & Becklin (1987) extended this search to cluster white dwarfs in the Pleiades and Hyades but found no companions. They also extended the survey to many more field white dwarfs. They discovered two interesting objects. The pulsating white dwarf G29-38 showed an infrared excess. The simplest explanation for this appeared to be an unresolved companion with a temperature around 1200K and a luminosity of $5 \times 10^{-5} L_{\odot}$. Such an object would be a definite brown dwarf. However 10 micron observations by Graham et. al. (1990a,b) and Tokunaga, Becklin & Zuckerman (1990) found a flux in excess of that which would be expected from the thermal emission from a brown dwarf of 1200K. It therefore appears there may be some sort of dust shell surrounding the white dwarf. However Graham et. al. (1990a,b) also found evidence for radial velocity variations in the object indicative of a companion. Barnbaum & Zuckerman (1992) subsequently determined this period to be around 11 months. The case against a brown dwarf companion is therefore not yet closed in this instance.

Becklin & Zuckerman (1992) also found a resolved companion to the white dwarf GD165. GD165B is at a distance of 120 AU from the primary. They estimated a temperature for this object of $2100K$ and a luminosity of $8 \times 10^{-5} L_{\odot}$. Jones et. al. (1994) use their constant water vapour opacity method to improve these estimates to $1860 \pm 160K$ and $8.6 \times 10^{-5} L_{\odot}$. The spectrum of GD165B is also unusual in the optical (Kirkpatrick, Henry & Liebert, 1993), although the infrared spectrum appears to follow the sequence of Jones et. al. (1994). The primary GD165 has a temperature of 11000K. This corresponds to a cooling age of around 600 Myr. In Fig 3.10 the position of GD165B from Jones et. al. (1994) is plotted. Since the companion must be at least as old as the white dwarf cooling age, then according to the models of Burrows et. al. (1993) this object should have a mass in the range $0.058 - 0.078 M_{\odot}$. This object therefore remains a good brown dwarf candidate.

Spectroscopic radial velocity surveys are being carried out by many groups (including those lead by Duquennoy, Marcy, Cambell and Henry). Marcy (1994) reviews the work of all of the groups and notes that two approaches to this technique are possible, surveying a large sample ($\sim$ hundreds) at resolutions capable of determining velocity shifts of around ~ 200 m/sec, or surveying smaller ($\sim$ tens) samples to a precision ~ 10 m/sec. The first approach appears so far to have had more success in finding potential brown dwarfs. Marcy (1994) however presents a statistical analysis which shows that the spread in inclination angles in a large sample means that the probability of finding several high mass objects with a low $M \sin i$ is high. One such object may be HD114762, which Latham et. al. (1989) have found to have 84 day period variations corresponding to $M \sin i = 0.011$. The nature of the (unseen) companion is still therefore uncertain.

3.4.3 Searches in Clusters

Searches for low mass objects and brown dwarfs in stellar clusters have several advantages. These are:

- The cluster age is generally well known from observations of the upper main sequence turn off point. In addition in young clusters brown dwarfs will have relatively high temperatures ($\sim 3000K$) and luminosities ($\log L/L_{\odot} \sim -4$). This means they should be relatively easy to detect at optical and near-infrared wavelengths.
- The cluster distance is known.
- The cluster extinction is known and may be corrected for.
- The cluster metallicity is known.

All of these properties mean that comparison with theoretical models (assuming a suitable temperature scale is known) are relatively straightforward. In addition clusters generally occupy a relatively small area of the sky, thus limiting the search area, and are often amenable to proper motion surveys.

In order of increasing age, the five principal clusters which have been surveyed for brown dwarfs are Taurus-Augira (age $\sim 10^6$ yr.), Rho-Ophiuchus ($\sim 3 \times 10^6$ yr.), Theta Carinae ($\sim 2 \times 10^7$ yr.), the Pleiades ($\sim 7 \times 10^7$ yr.) and the Hyades ($\sim 6 \times 10^8$ yr.). I will now consider the surveys which have been made of each of these clusters in turn.

The Taurus-Augira Clouds

This is one of the nearest sights of recent star formation ($d \sim 140$ pc.) and many low mass pre-main sequence objects (T-Tau stars) have been found in the cluster. Forest et. al. (1989) made a K band survey of areas on 25 square arcsec around 26 T-Tau stars in an effort to detect faint companions. They found 20 objects, nine of which had very red JHK colours. Of these nine, seven were visible on Palomar Sky Survey plates and could therefore have their proper motions determined. Four of the objects were found to have proper motions consistent with cluster membership. Comparison of the photometry with theoretical models assigned masses of $\sim 0.01 M_\odot$ to these objects, indicating that they were good brown dwarf candidates. Stauffer et. al. (1991) carried out follow up infrared photometry of these candidates and found they were heavily reddened background dwarfs. No good brown dwarf candidates therefore remain in this cluster.

Rho Ophiuchus

Rho Ophiuchus has a very high internal extinction ($A_V > 50$), making surveying only possible in the infrared. It has an age of $\sim 3 \times 10^6$ yr and is at a distance of 160 pc. The deepest survey of this cluster is that of Rieke & Rieke (1990). This survey, complete to $K = 15, H = 17$ was extended by Comeron et. al. (1993) to a total area of 200 square arcmin, who found 91 faint sources. The cluster age corresponds to the deuterium burning main sequence, therefore comparison can be made with theoretical isochrones even if the stars are all not exactly coeval. By comparing different reddenings to the theoretical predictions and the observations they were able to derive masses for their objects. They find 7 brown dwarf candidates with

masses from 0.01 to 0.07 $M_{\odot}$. Infrared follow-up spectroscopy is needed to determine whether these candidates are as cool as the authors claim.

Theta Carinae

Theta Carinae has an age of around 2×10^7 yr. is at a distance of 155 pc and is almost free of reddening. Hambly (1991) used I band Schmidt plates to construct a proper motion survey with a baseline of $\sim$ 10 years down to $I \sim 18$. While a number of objects with the cluster proper motion were found, no obvious sequence in the $I, R-I$ diagram could be constructed, although a number of apparently cool objects were found from their $R-I$ colours.

The Pleiades

The Pleiades at age 7×10^7 yr., distance 130 pc and with no appreciable reddening is an ideal hunting ground for brown dwarfs. Chapters 4,5 and 6 of this thesis discuss photometric and spectroscopic observations of brown dwarf candidates in the cluster from the proper motion survey of Hambly, Hawkins & Jameson (1991, 1993). In this section I will discuss the results of other groups observations of the cluster.

The first CCD survey of the cluster was carried out by Jameson & Skillen (1989) who surveyed an area of 125 square arcminutes at R and I. They proposed seven brown dwarf candidates based on their position in the $I, R-I$ diagram. Stauffer et. al. (1989) made a similar survey at V and I. Stauffer et. al. (1994) extended the areal coverage of their survey to a total of 0.4 square degrees finding in total six brown dwarf candidates. Hamilton & Stauffer (1993) obtained spectra of several of the Stauffer et al. (1989) candidates and confirmed their status as very cool objects. Both sets of objects are therefore good brown dwarf candidates. They may however simply be background stars.

Simons & Becklin (1992) surveyed an area of 200 square arcminutes at I and K. They also surveyed a 75 square arcmin control area outside the cluster. From the resulting $I, I-K$ diagram they identified 22 objects with masses in the range 0.04 to $0.01 M_{\odot}$. Martin (1993) carried out spectroscopy of several of the brown dwarf candidates, and assigned spectral types in the range M1 to M3, corresponding to

masses greater than $0.3M_{\odot}$. The objects therefore appear to be hotter than their $I-K$ colour suggests, and therefore not brown dwarfs.

The Hyades

The Hyades has an age of 6×10^8 yr. and a distance of only 48 pc. It is therefore an ideal cluster for studying the bottom of the main sequence. It's age however means that any brown dwarfs in the cluster will have cooled significantly, cancelling out the advantage of its close distance. In addition the large cluster depth to distance ratio (due to the closeness of the cluster) introduces a large scatter into the main sequence.

Early photometric surveys were carried out by Leggett & Hawkins (1988,1989). More recently Brya et. al. (1992, 1994) and Reid (1992, 1993) have carried out proper motion surveys using Schmidt plates. Leggett, Harris & Dahn (1994) provide a good review of all previous work on the Hyades to date. In addition they have selected a sample of 62 of the faintest Hyads from the above surveys, and obtained high quality V and I photometry to add to the existing infrared photometry. They follow the main sequence down to $M_I = 14.6$. Objects of this luminosity may or may not be classified as brown dwarfs depending on the models employed.

3.5 Conclusions

In this chapter I have given a necessarily brief review of the basic physics and evolution of low mass stars and brown dwarfs and discussed the mechanisms by which their observed properties (colours and magnitudes) may be converted to temperatures and luminosities for comparison with that theory. This conversion remains a difficult and controversial process, and I will return to this problem in Chapter 6.

I have also outlined another tool for investigating stellar populations – Luminosity and Mass Functions. They are a powerful statistical tool for investigating the abundance of low mass stars, and by extrapolation can often give clues as to brown dwarf numbers. The most important result in this field is the much steeper

mass function (implying a larger fraction of low mass objects) for population II as opposed to population I.

Finally I have discussed the various locations one may search for brown dwarfs – in the field, as binary companions or in clusters and reviewed the successfulness of each method. Overall the advantages of cluster surveys seem to make these the preferred hunting grounds. However any brown dwarfs one finds here will generally be still hot ($\sim 2500K$) and therefore not necessarily representative of the nature of 'classical' cool brown dwarfs. Nevertheless it is here (specifically the Pleiades) that Chapters 4,5 and 6 will concentrate their efforts.

Chapter 4

The Pleiades I: Background and Infrared Photometry

This chapter reviews the parameters of the Pleiades relevant to brown dwarf searches and describes the proper motion survey of the cluster carried out by Hambly, Hawkins & Jameson (1991). It then gives the results of a programme of $RIJHK$ photometry carried out of cluster members and identifies a number of single and binary brown dwarf candidates.

4.1 The Pleiades Cluster

The Pleiades open cluster (M42) is located at right ascension $03^h\ 40^m$, declination $+24°$ in the constellation of Taurus. It contains 6 (or 7, depending on the observer) naked eye members and many hundreds of fainter objects. As a relatively young ($\sim$ 70 Myr, see Section 4.1.1 below), nearby ($m - M \sim 5.65$, see Section 4.1.2) cluster it forms an ideal hunting ground for brown dwarfs, as they will still be relatively hot ($T_{eff} \sim 2500$K), and luminous ($I \sim 17$) (Stringfellow 1991). In addition the cluster is fairly compact, with a maximum angular diameter of $\sim 9°$ (van Leeuwen 1980). The central region may therefore be imaged on one UKST Schmidt Plate.

Previous searches for brown dwarfs in the Pleiades have been reviewed in Section 3.4.3 and the cluster Luminosity and Mass functions discussed in Section 3.3. Here I

will discuss the parameters of the cluster (age, distance, metallicity and reddening) important for this work.

4.1.1 The Cluster Age

The upper main sequence turn off age of the Pleiades is generally accepted to be $\sim$ 70 Myr (Harris 1976, Patenaude 1978). There is however some evidence that this age may be affected by main sequence overshooting and the true age may be upto twice this value (i.e. $\sim$ 150 Myr). The lower main sequence age is also uncertain, as it is possible that the low and high mass stars are not coeval. Stauffer (1982) found a lower main sequence age of $\sim$ 300 Myr but later revised this (Stauffer 1984) to $\sim$ 100 Myr. Eggen & Iben (1988) used narrow band photometry to determine an age $\sim 100 - 200$Myr. In their latest work Stauffer et al. (1994b) use an age of 70 Myr and lacking any firm evidence to the contrary I shall also use this age. The effects of different cluster ages will however also be considered.

4.1.2 The Cluster Distance

There have been many determinations of the distance to the Pleiades (Crawford & Perry (1976), Turner (1979), Jones (1981), van Leeuwen, Alphenaar & Brand (1986), Eggen & Iben (1988)). These were based on a main-sequence fitting technique, the zero-age main sequence being defined by a combination of nearby field stars of known parallax and the Hyades main sequence. Gatewood et. al. (1990) obtained trigonometric parallaxes of several cluster members.

Hambly (1991) considered all of these and arrived at a mean distance modulus $m - M$ of 5.65 ± 0.12. Since then O'Dell, Hendry & Collier-Cameron (1994) have applied a new technique to the cluster. The technique is based on a knowledge of the periods, rotational velocities and angular diameters of a small sample of late type stars within the cluster. They derive $m - M = 5.60 \pm 0.16$, which is in good agreement with the value used by Hambly (1991). I will therefore continue to use the value of Hambly (1991) in this work.

4.1.3 The Cluster Metallicity

The most recent determination of the cluster metallicity is that of Boesgaard & Friel (1990). From their high dispersion, high signal to noise spectroscopic observations of twelve F and G dwarfs in the cluster they obtain [Fe/H]= -0.034 ± 0.024, i.e. essentially the same as the solar value.

4.1.4 The Cluster Reddening

Reddening to the Pleiades has been determined by Breger (1987), who determines $E(B-V) = 0.04$. Burstein & Heiles (1982) use a combination of HI and galaxy counts to derive an extinction $E(B-V) = 0.15$ *behind* the cluster. There is a small region of higher extinction in the cluster at $\mathrm{RA}_{1950} = 3^h43^m$, $\mathrm{DEC}_{1950} = 23°30'$. None of the objects considered in this work fall in this region.

The small reddening, combined with the relatively long wavelength (> 6000Å) of the observations considered in this thesis make the application of extinction corrections unnecessary, especially since most of the R and I band magnitudes used in this work are photographic in origin. No corrections have therefore been applied to any of the photometry reported here.

4.2 Proper Motion Surveys

The Pleiades stars have a common proper motion of $\mu_{\alpha\cos\delta} = +2.5$ arcsec/century, $\mu_\delta = -4.5$ arcsec/century (Jones 1981). Van Leeuwen (1980) finds that cluster members are found up to 4.5° away from the cluster centre.

There is a long history of proper motion surveys of the cluster, from the early work of Hertzprung (1947) to the surveys of Eichhorn et. al. (1970), Jones (1973) and Jones (1981). The most recent survey is that of Hambly, Hawkins & Jameson (1991 - HHJ91). This survey, fully described by Hambly (1991), is the deepest proper motion survey of the cluster so far carried out. In addition its use of R band plates for the proper motion work means it has high sensitivity to cool, low mass objects. Finder charts and object lists for this survey are given by Hambly, Hawkins & Jameson (1993). This proper motion survey forms the basis of all the Pleiades

work reported in this thesis. I will therefore briefly describe its construction and results.

The survey was based on the Palomar Observatory Sky Survey plates E-441 (taken on 29/11/51) and E-31 (taken on 21/12/49). Second epoch positions were obtained from the UK Schmidt Telescope Unit (UKSTU) plate OR13496 (taken on 17/12/89). The plates were measured using the COSMOS plate measuring machine (MacGillivray & Stobie, 1984) of the Royal Observatory, Edinburgh. The images were paired up using software designed by Hawkins (1986) to produce a proper motion catalogue. The UKSTU I band plate I13497 was also measured to provide I magnitudes. The plate scans were calibrated using photometry from Erro (1969), Stauffer (1982), Stauffer (1984) and Jameson & Skillen (1989) converted to the photographic system using the transforms of Bessell (1983,1986) (see Section 2.1.2).

Figure 4.1 shows a proper motion diagram of all stellar images common to the first and second epoch plates, taken from HHJ91. The Pleiades stars can be clearly distinguished as a clump of stars (circled) in the SSE region of the diagram. An adjacent region containing field stars is also circled. Figure 4.2 plots $I, R-I$ colour-magnitude diagrams for these two regions. The effectiveness of the proper motion survey in picking out the Pleiades main sequence is apparent.

Hambly (1991) evaluates membership probabilities for the survey and finds that for objects brighter than $I = 17.5$ the membership probability is always greater than 70%. For objects brighter than $I = 16.5$ this figure rises to over 90%. Contamination of the survey by background and foreground objects will therefore be low.

Hambly (priv. com) has also produced a list of so-called I-only objects. These are objects that do not appear on the R plates but only on the I plates. They are therefore obviously very red and faint but since they do not have measured proper motions their membership status is naturally very uncertain.

Currently in development at the Royal Observatory, Edinburgh is a new measuring machine, superCOSMOS. Due to improved scanning technology and better environmental control this will have an astrometric accuracy $\sim 5-10\times$ better than COSMOS. It will therefore be able to carry out a proper motion survey of the Pleiades based on I plates over a relatively short baseline ($\sim$ 5 years). This should

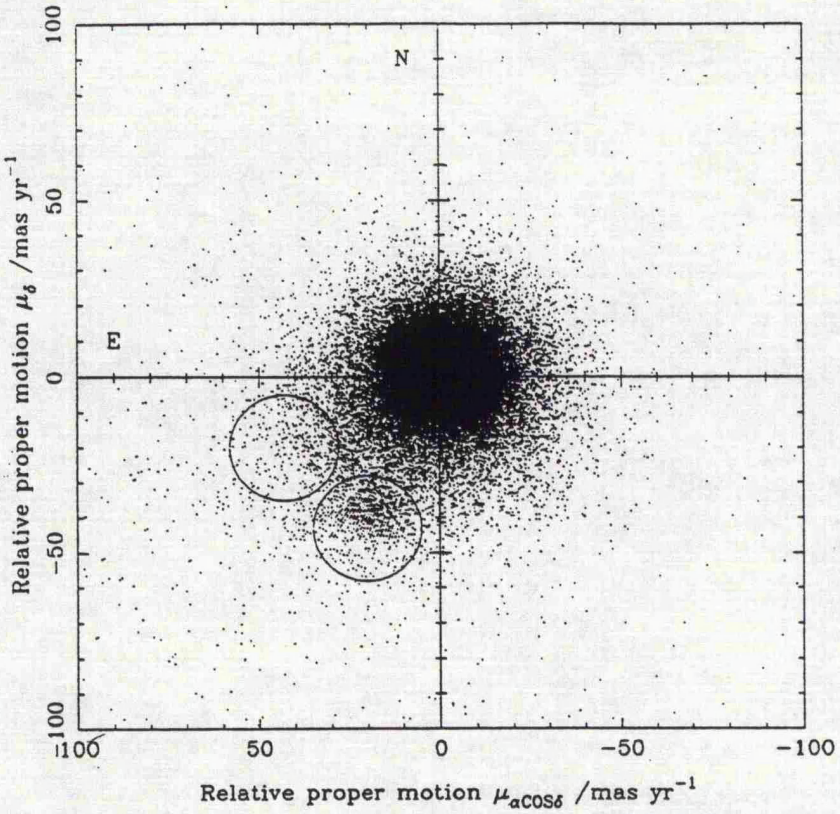

Figure 4.1: Proper motion diagram for all stars in the Pleiades field. The SW circle selects out the proper motion members, the NE circle a sample of field stars (from Hambly (1991)).

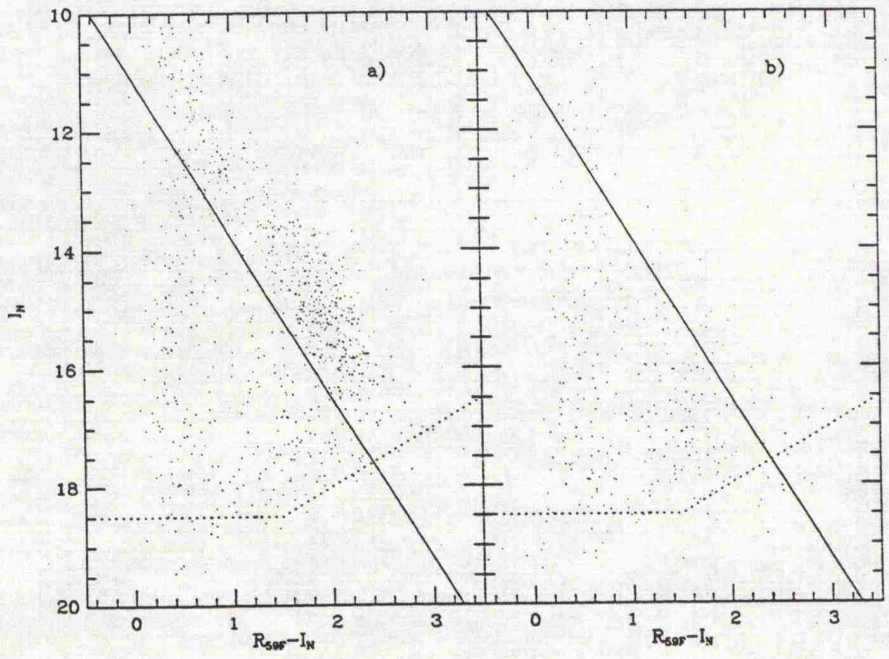

Figure 4.2: $I, R-I$ diagrams for (a) the SW circle in Fig. 4.1 (cluster stars) and (b) the NE circle (non-cluster stars) (from Hambly (1991)).

find proper motion members of the cluster upto 1 magnitude fainter than the HHJ survey. Any such objects would therefore be excellent brown dwarf candidates.

4.3 Infrared Photometry

The proper motion survey of HHJ91 selects a sample of Pleiades members down to $R \sim 20, I \sim 18$. The relatively short wavelength base of the $R-I$ colour however means that deriving temperatures for the reddest of these objects is uncertain. In order to rectify this HHJ91 obtained JHK photometry of a small sample of their objects. Here I extend this photometry to a much larger sample and discuss the observations in terms of the identification of brown dwarf candidates. I will also describe RI CCD observations of a smaller sample of HHJ91 objects.

4.3.1 Observations

The principal set of observations is JHK photometry of a total of 62 objects taken on 6th-9th October 1991 using the IRCAM infrared array at UKIRT. The weather and photometric conditions on all four nights were good. 48 of the stars observed were proper motion members from HHJ91. The selection of these stars from the list of 441 members was made according to two criteria

- All objects with $I > 16.5$ not previously measured by HHJ91. These are the candidate low mass stars/brown dwarfs.
- A sample of objects with $13 < I < 16.5$ chosen to include both bright and faint stars of all colours. These will help define the main sequence above the lowest mass objects.

The remaining observations were of a sample of I-only objects as described above. The data were reduced using the standard procedures outlined in Chapter 2.

The resulting JHK magnitudes, along with the RI COSMOS magnitudes from Hambly (1991) (converted to the Cousins system) or the RI service CCD observations (marked with asterix) are given in Appendix B. An estimate of the mean non-systematic photometric errors in the IRCAM photometry is possible since each

object was measured twice. The mean photometric error was found to be $\sim \pm 0.04$ magnitudes for all three wavebands. Appendix B also reproduces the data from HHJ91 for the 20 proper motion members measured by them. Errors are those quoted by Hambly (1991).

In order to confirm the calibration of the R and I COSMOS magnitudes given by Hambly (1991) and to estimate a mean scatter in those magnitudes, service observations were made using the GEC CCD detector of the Jacobus Kaptyn Telescope (JKT) on 18th October 1991. R and I observations were taken of 5 of the I-only objects and 10 of the HHJ91 objects. These CCD observations are indicated in Appendix B by asterix. No systematic differences were found between the CCD and COSMOS magnitudes. The rms scatter of the I COSMOS magnitudes was found to be $\sim \pm 0.12$ increasing to $\sim \pm 0.25$ for the faintest I-only images at the plate limit. The rms scatter of the R COSMOS magnitudes was $\sim \pm 0.21$.

4.3.2 Cluster Membership

Proper motions are not a certain indicator of cluster membership and it would be advantageous to reinforce these proper motions by a photometric membership test. The most obvious test is a Hertzprung-Russell (i.e. luminosity-colour) diagram, since this should pick out the Pleiades sequence well. Note that I will not employ the term 'main-sequence' in the following discussion since the lower mass Pleiades objects are still contracting to their degeneracy limited radii and therefore have not yet reached the zero age main sequence.

In Figure 4.3 I plot the $I, I-K$ colour-magnitude diagram for all of the candidate proper motion members for which photometry is listed in Appendix B. It is immediately apparent that not all of these objects are cluster members, a small number of them falling well to the left of the Pleiades sequence. These non-members have been denoted by squares, the rest of the objects being shown as vertical crosses ('plus signs') with a small number of intermediate cases shown as question marks. Likewise the I-only objects are shown as squares (clear non-members), question marks (uncertain) and inclined crosses ('multiplication signs' - likely members). Note that

as expected only a small fraction (2 out of 14) of the I-only candidates appear to be cluster members.

Also plotted on Figure 4.3 as open circles are higher mass Pleiades members from Stauffer (1982). This brighter sequence can be seen to match the bright end of the fainter HHJ91 sequence well.

From this figure it is apparent that the $I-K$ colour is a reasonable temperature indicator and the $I, I-K$ diagram a reasonable discriminant of cluster membership when combined with proper motion information. For comparison I plot in Figure 4.4 the $I, R-I$ colour-magnitude diagram. It can be seen that the Pleiades sequence appears much broader in this diagram that in the $I, I-K$ diagram. Some of the additional width is due to the greater photometric error in this colour due to the fact that it is composed of two photographic magnitudes. This cannot account for of all the additional scatter however, which must simply result from the relatively poor quality of $R-I$ as a temperature indicator for very cool ($T_{eff} < 3000K$) objects.

An additional source of scatter in both of these diagrams is unresolved binarity. This will be discussed in Section 4.3.4 below.

4.3.3 Comparison with Theory

As previously discussed (Sections 3.1,3.2) the comparison of the observed properties of low mass stars with theory is a difficult and controversial process. The theoretical models of low mass stars and especially brown dwarfs are heavily age dependant, and yield results in the form of luminosities and effective temperatures. The conversion of these quantities to observable magnitudes and colours requires the use of empirical transforms which are themselves of uncertain accuracy and an accurate cluster distance.

In Section 3.1 various theoretical models of low mass stars and brown dwarfs were discussed. Here I will compare the Pleiades photometry with the models of Stringfellow (1991 - S91) and Burrows et. al. (1993 - BSHL93). The transformation of the models from T_{eff} to $I-K$ and M_{bol} to I was carried out using the relations supplied by Bessell (1991). The reasons for preferring this temperature scale have

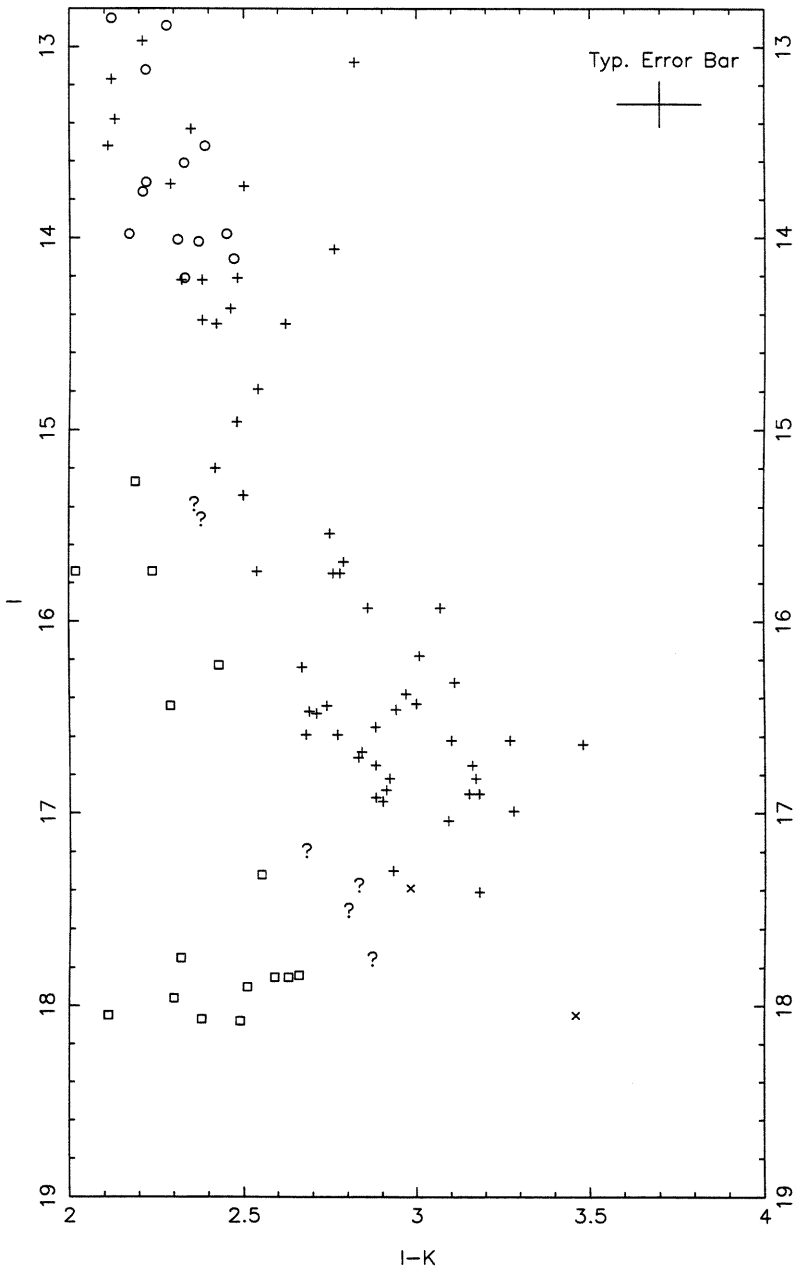

Figure 4.3: The $I, I-K$ diagram

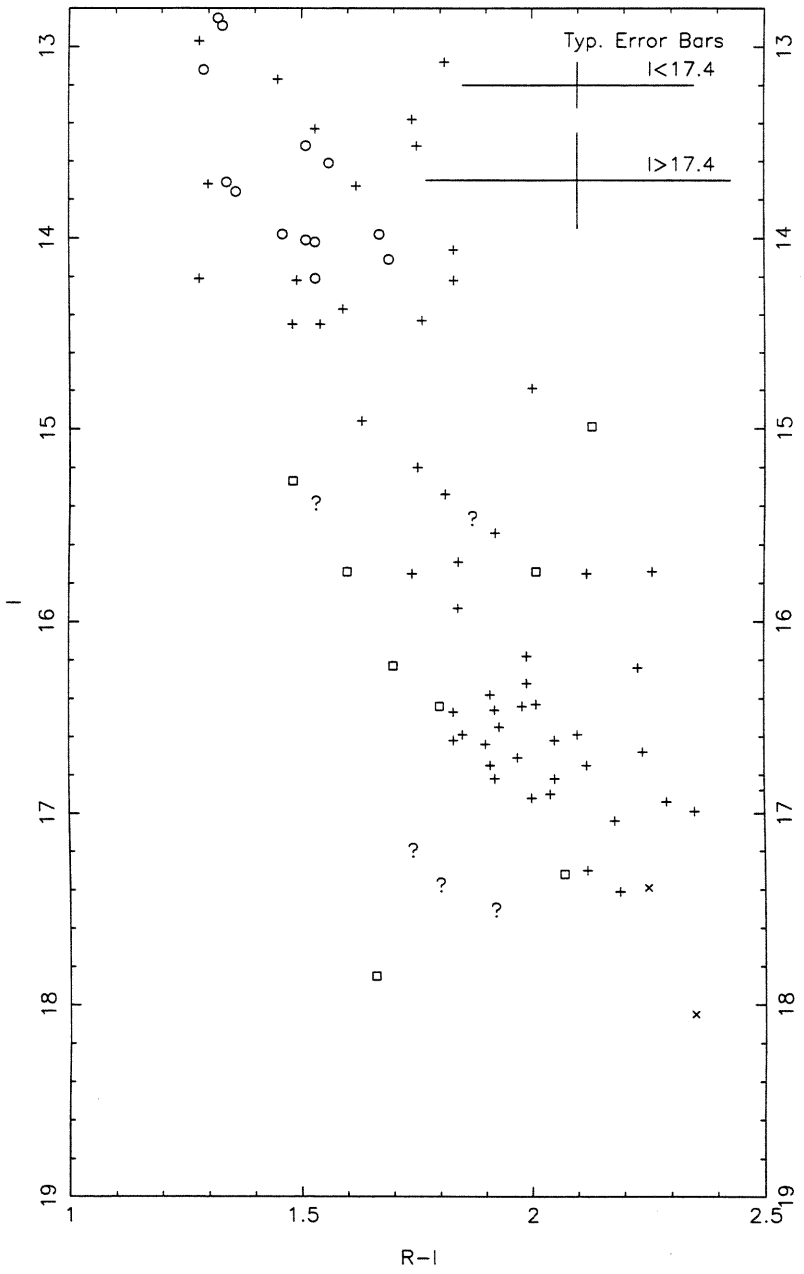

Figure 4.4: The $I, R-I$ diagram

been discussed in Section 3.2. In Chapter 6 the question of effective temperatures for Pleiades objects will be reexamined in more detail.

In Figure 4.5 I replot the $I, I-K$ diagram using the same symbols as Figure 4.3. Overlayed on the figure are the 1, 6, 10, 50, 70 and 300 Myr isochrones of S91 (solid squares, solid and dashed lines) and the 70 Myr isochrone of BSHL93 (solid triangles and dotted line). It is interesting to note that our lower bound to the Pleiades sequence lies very close to the 70 Myr isochrone of S91. This suggests that the lower and upper main sequence ages of Pleiads are approximately the same. Using the model of BSHL93 the Pleiades sequence lies considerably to the right of the isochrone however, which might naively be interpreted as implying a younger age for lower mass Pleiads. This is however more likely simply a result of inaccuracies in the models or temperature scale. The spread in the Pleiades objects would seem to indicate a similar conclusion – using the S91 models there seems to be evidence for a second epoch of formation around 30 Myr ago. This was the conclusion drawn by Steele, Jameson & Hambly (1993). This conclusion is almost certainly incorrect, and instead the spread in the $I, I-K$ diagram is now believed to be simply a consequence of unresolved binarity.

4.3.4 The effect of Binarity and the Binary Fraction

Duquennoy & Mayor (1991) found that for main sequence G dwarfs $\sim 53\%$ of systems were multiple. Similarly Richichi et al. (1994) find that for low mass pre main sequence objects $\sim 49\%$ of systems are multiple. Unresolved binarity (and higher degrees of multiplicity) will naturally affect the photometry of our objects. In this section I will discuss how these effects may be modelled and use this photometric model to make a quantitative estimate of the low mass Pleiades binary fraction.

The 70 Myr model of Stringfellow (1991), converted to the observational $(I, I-K)$ plane using the temperature scale and bolometric correction of Bessell (1991), was used to create artificial binaries of all combinations of objects from $0.2M_{\odot}$ to $0.01M_{\odot}$. These have been plotted on Figure 4.6 and are labelled according to the combination employed (e.g. a $0.09 + 0.04M_{\odot}$ binary is labelled as '0904'). Also plotted on this figure is the 70 Myr model for single objects. It is immediately apparent that the

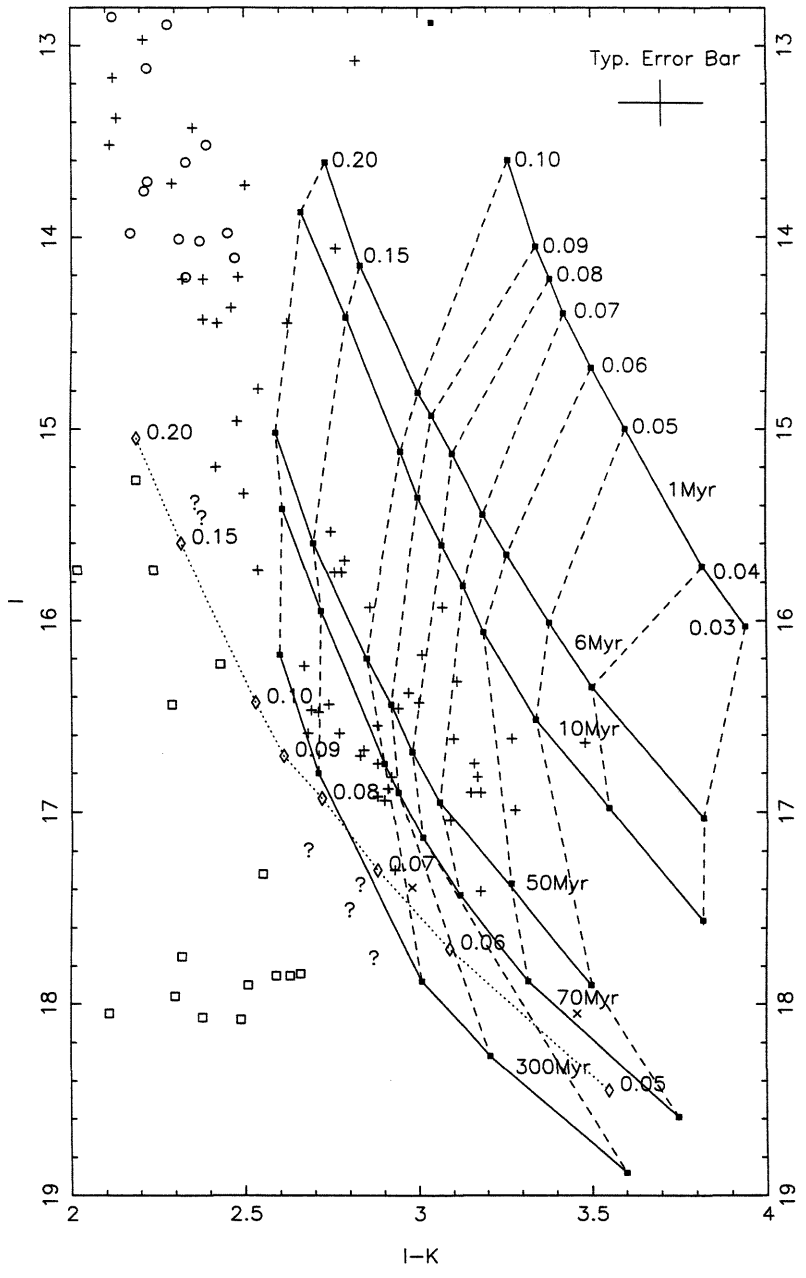

Figure 4.5: The $I, I-K$ diagram with isochrones from Stringfellow (1991 - solid and dashed lines) and Burrows et.. al. (1993- dotted line) overlayed.

effect of binaries on the $I, I-K$ diagram is to give a second 'binary' sequence (BS) lying ~ 0.75 mag. above the 'single star sequence' (SSS). It is important to note that the BS is not formed only by objects of equal masses. Even if the masses of the binaries differ substantially then the lower total luminosity is compensated for by a redder net colour, keeping the object on the BS. It is only in the case of extreme mass ratios (e.g. '2003') that the artificial objects move away from the BS to the gap inbetween it and the SSS. Note that combinations involving masses of 0.01 or $0.02 M_{\odot}$ lie very close to the SSS and are therefore not plotted.

Figure 4.7 plots the objects from Appendix B which lie in the region of the $I, I-K$ plane covered by the artificial binaries (i.e. $14.5 < I < 17.5$). Also plotted are the loci of the SSS (solid line) and BS (dashed line). It is immediately apparent that the spread in the $I, I-K$ diagram noted in above is in fact due to binarity. Using this diagram identifies HHJ5, 6, 10, 11, 14, 16, 19, 22, 24, 36, 46, 54, 58, 81, 101, 118 and 236 as probable binaries. By contrast HHJ 2, 3, 7, 8, 9, 12, 13, 15, 17, 20, 21, 23, 25, 27, 37, 92, 139 and 153 appear to be single. This corresponds to $\sim 47\%$ of systems being binary. While this figure compares well with those given at the start of this section, it should not be relied on too heavily since no attempt has been made here to treat rigorously the incompleteness errors in the sample.

The $I, I-K$ diagram presented here does not allow any estimate to be made of the masses of the binary companions, since many combinations occupy the same space on the diagram. The objects identified here as binaries should however be followed up, either with high resolution imaging (e.g. using the Hubble Space Telescope) or high dispersion spectroscopy in order to search for evidence of the binary companions. If found, such companions could have their masses measured dynamically. Such measurements would allow a much better calibration of the low mass pre-main-sequence in the Pleiades, and also help settle the debate at to the nature of the lowest mass objects found.

4.3.5 Brown Dwarfs?

In the absence of dynamical masses however, one can still attempt to assess the quality of the brown dwarf candidates identified in Section 4.3.3. From Figure 4.7

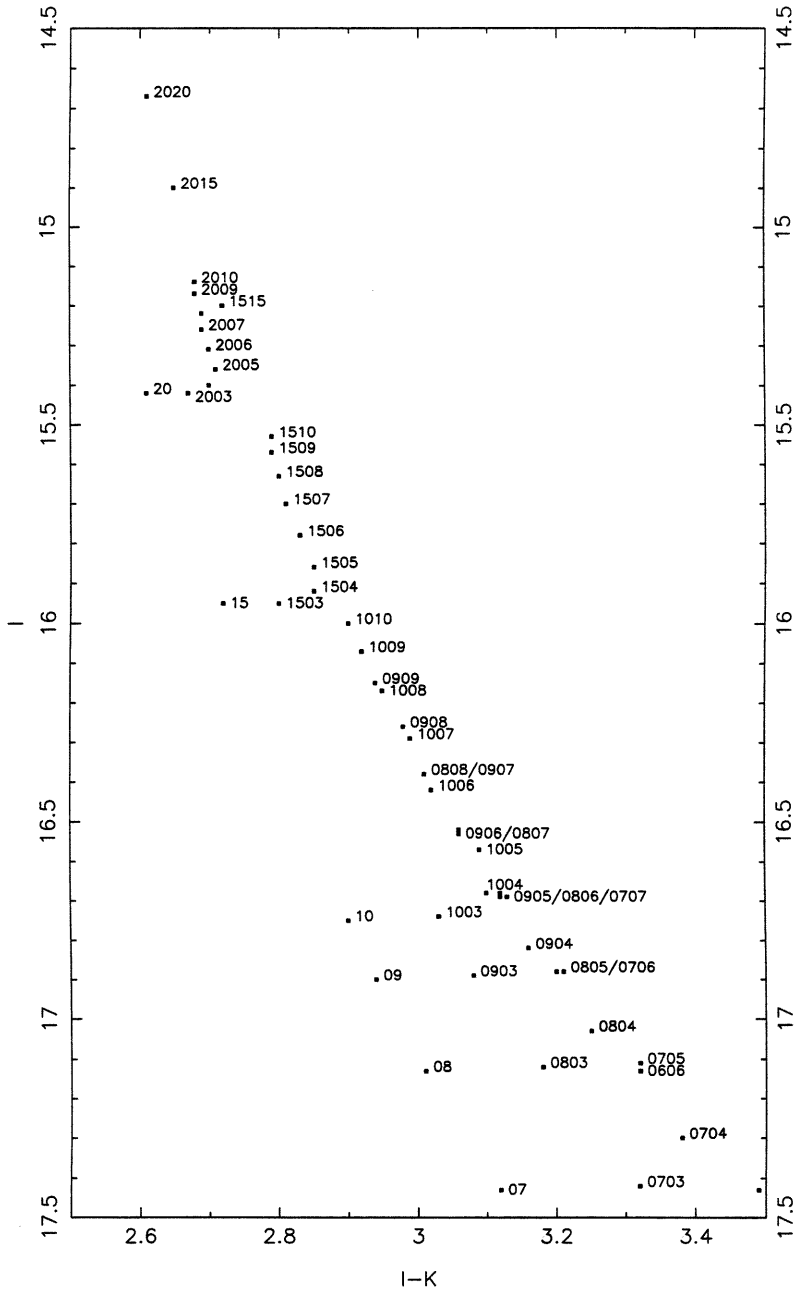

Figure 4.6: Combinations of artificial binaries plotted on the $I, I-K$ diagram

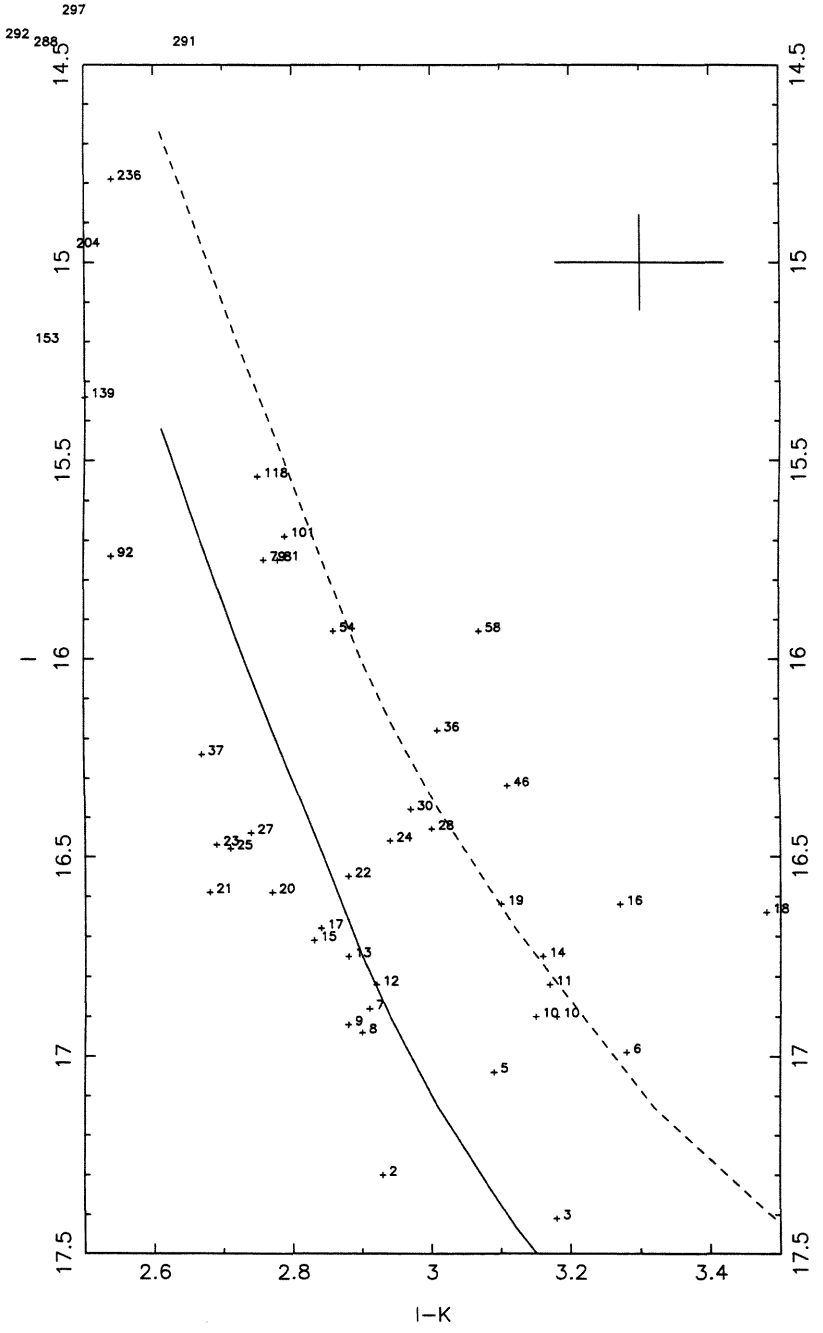

Figure 4.7: Pleiades members overlayed on the Single Star (solid line) and Binary Star (dotted line) Sequences

it is possible to identify 2 single brown dwarf candidates (HHJ2 and HHJ3, with masses of around $0.075M_{\odot}$). In addition all combinations of systems which contain *at least* one brown dwarf must lie in a region redder and fainter than the '0808' point in this diagram. For Stringfellow's model this corresponds to objects with $I-K>3.0$,$I>16.4$. Seven binary systems should therefore contain brown dwarf candidates. These are HHJ5, 6, 10, 11, 14, 16, and 19. Using the model of Burrows et. al. (1993) moves the '0808' point to $I-K>2.8, I>16.1$. This brings a much larger number of systems into the brown dwarf containing regime. Using this model indicates a total of 26 brown dwarf containing systems, of which 11 are single and 15 multiple. Note also from Figure 4.6 that objects above the '0808' point may or may not also contain a brown dwarf component.

In Chapter 7 I will return to the question of the status of our lowest mass components, in the light of the optical and infrared spectroscopy that will be presented in the following two chapters.

4.3.6 Other Photometric Diagrams

For completeness I give here the $R-I, I-K$ and $J-H, H-K$ diagrams of of the cluster objects. On these diagrams open squares indicate single objects, filled squares are binary objects, crosses objects of unknown binarity and circles higher mass Pleiads from the survey of Stauffer (1982). Note that much of the spread in the $R-I, I-K$ diagram, which Steele, Jameson & Hambly (1993) attributed to an age spread is simply due to binarity, which has a larger effect in $I-K$ than $R-I$. The errors in the $J-H, H-K$ diagram make it hard to determine any trends in this diagram, although a possible effect due to binarity may be present.

4.4 Conclusions

In this chapter I have shown how using a combination of optical and infrared photometry of proper motion members of the Pleiades allows the identification of a number of brown dwarf candidates. The number of candidates identified is a strong

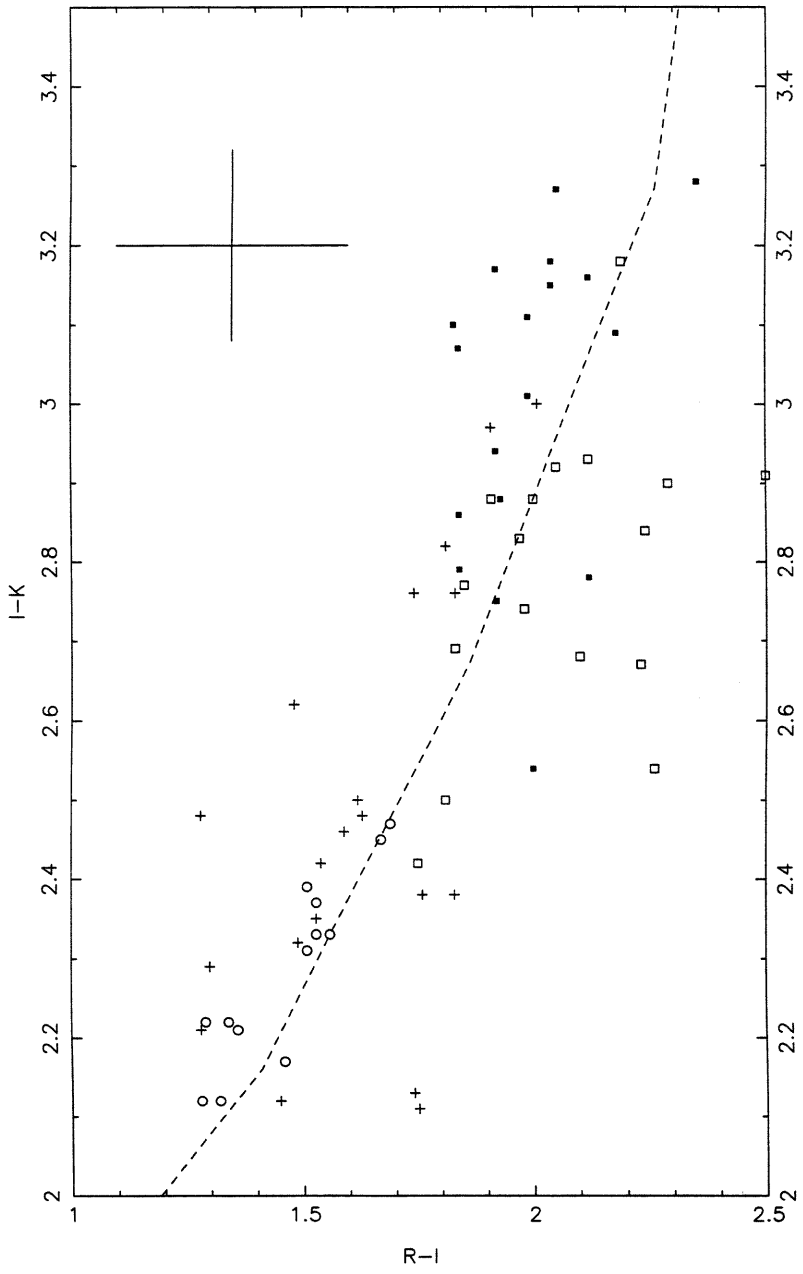

Figure 4.8: The $R-I$,$I-K$ diagram. Single objects are open squares, binaries are filled squares, crosses objects of unknown binarity and circles higher mass objects from Stauffer (1982).

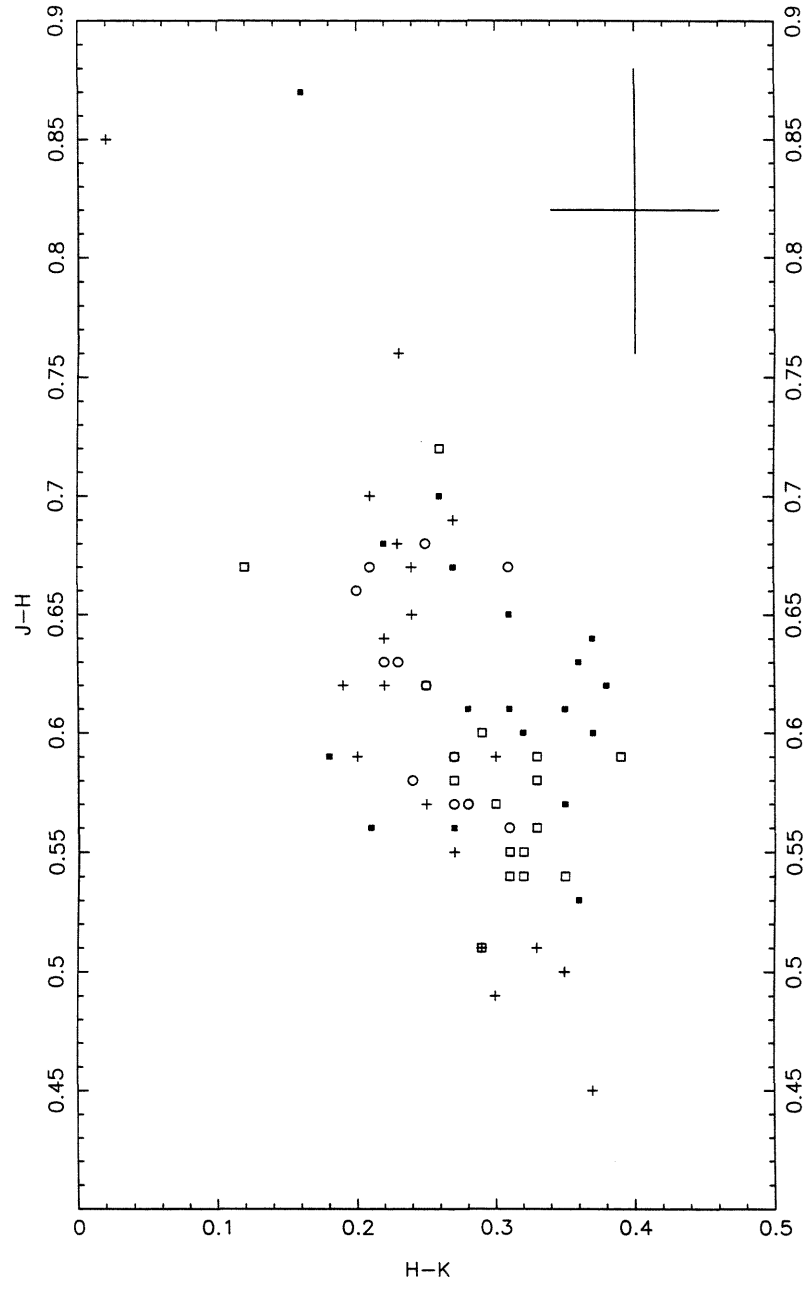

Figure 4.9: The $J-H, H-K$ diagram. Symbols as Figure 4.8

function of the theoretical model and temperature scale employed. In addition unresolved binarity means that many objects will appear to be younger than their true ages. However using an $I, I-K$ diagram it is possible to identify probable binary members (no matter what combination of objects forms the binary) and a number of brown dwarf containing binary systems (again the exact number depends on the model and temperature scale). The following chapters will outline attempts to better determine the true nature of the lowest mass objects.

Chapter 5

The Pleiades II: Optical Spectroscopy, a Spectral Sequence and Activity

In order to further investigate the Pleiades low mass stars and brown dwarf candidates of the last chapter, this chapter presents results from optical 3500 - 9700 Å spectroscopy of 31 of the HHJ91 members. In addition ROSAT X-ray fluxes from three Pleiades pointings are used in an investigation of coronal activity of the low mass objects.

5.1 Observations

The spectroscopic observations discussed in this chapter were obtained using the FOS spectrograph of the WHT discussed in Section 2.2.1. The observations were obtained on the nights of 1993 November 12-13. The weather on both nights was clear. In order to obtain to the full spectral resolution of the spectrograph, a slit width of 1 arcsec was used on both nights. Average seeing on the first night was ~ 1 arcsec and ~ 2 arcsec on the second night. The absolute flux calibration of the 2nd night observations will therefore be unreliable. This is not important since I will in general be concerned with normalized spectra in the following analysis. All of the objects observed were at airmass < 2.0 and in most cases < 1.3. In all cases care

was taken to rotate the slit to the optimum angle in order to compensate for the effects of differential atmospheric refraction (Fillipenko 1982).

Table 5.1 presents a list of the objects observed with exposure times and observation dates. Several sets of objects were targeted for observation. These were:

- a sample of the lowest mass objects identified in the analysis of the infrared photometry presented in the previous chapter.
- all of the objects for which partial or complete 1-2.5 micron spectra had been obtained using CGS4 at UKIRT. These spectra will be presented in Chapter 6.
- a sample of X-ray bright Pleiades members that were identified in the ROSAT PSPC fields 200068, 200556 and 200557 by Hodgkin (priv. com.). These X-ray results will be discussed in Section 5.5.2 below.
- a sample of objects from the survey of HHJ with various $R-I$ colours and luminosities.
- a sample of M dwarf spectral standards from Kirkpatrick, Henry & McCarthy (1991) and Leggett (1992). These were observed in order to provide comparison spectra for typing.

The data were reduced using routines from the STARLINK supported package FIGARO (Shortridge 1991) as outlined in Section 2.2.1. Briefly, the order-separating cross disperser introduces a curvature into the spectra which was removed before any further reduction took place. Both tungsten and sky flats were used to flat-field the data and the instrumental response calibrated using observations of standards from Oke & Gunn (1983). Atmospheric extinction effects were removed using the extinction tables of King (1985), however no attempt was made to remove terrestrial O_2 and water vapour absorption features from the spectra as the humidity variations through each night were large. The spectra therefore show the atmospheric 'A' and 'B' bands at 6897 and 7594 Å and water vapour features at 7186, 8164, 8227, 8282, 8952 and 8980 Å. Above 9000 Å water vapour features dominate the spectra. These

Object	Exposure (seconds)	Date (1993 Nov)
HHJ2	1500	13
HHJ3	1800	12
HHJ6	1200	13
HHJ7	1500	12
HHJ9	1500	13
HHJ12	1500	13
HHJ16	1500	12
HHJ18	1500	13
HHJ19	1500	13
HHJ23	1500	13
HHJ36	1500	12
HHJ37	1000	12
HHJ44	1200	13
HHJ48	1500	12
HHJ54	1500	12
HHJ58	800	12
HHJ59	1500	12
HHJ101	800	13
HHJ111	1000	12
HHJ139	300	13
HHJ144	600	13
HHJ161	600	13
HHJ229	400	13
HHJ250	600	12
HHJ257	400	13
HHJ298	600	12
HHJ390	400	12
HHJ391	400	12
HHJ427	400	13
HHJ429	300	13
HHJ430	300	13
HHJ435	400	13
HHJ436	400	12
GL65AB	30	13
GL806	20	13
GL809	3	13
GL829	5	13
GL875.1	15	13
GL905	30	12,13
GL905.2	15	12

Table 5.1: Objects observed using FOS

may be intrinsic to the spectra or terrestrial in origin. This region will therefore generally be ignored in the discussion that follows.

5.2 Line Identifications and Spectral Sequence

Fig. 5.1 shows an example spectrum with various spectral features identified. The primary source for line identification was Kirkpatrick et. al. (1991). Other sources for line identification were Ẅay, Stein & Warren (1974) and, for terrestrial features, Stevenson (1994). All of the Pleiades spectra show Hα emission, a signature of youth, further enhancing their membership status. The spectrum of HHJ144 however (a photometric non-member of the cluster) does not show Hα emission, validating the photometric membership tests applied in Chapter 4. Hα emission is a recognised signature of chromospheric activity and I shall discuss this, along with ROSAT X-ray observations of the coronae of cluster members, in Section 5.5 later.

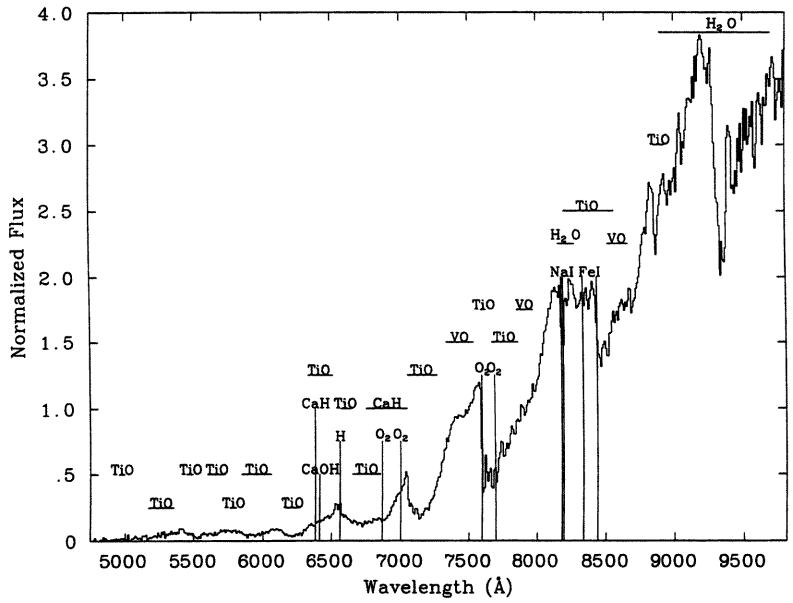

Figure 5.1: FOS 'red' spectrum of HHJ3

As expected the spectra are generally cool in appearance, although the overall shape deviates significantly from a black body due mainly to molecular absorptions of TiO and VO. These molecular absorptions make the determination of effective temperatures (T_{eff}'s) for the objects difficult. As already discussed (Section 3.2), simple black-body fitting will obviously be inappropriate and the best approach is to fit a model atmosphere including all of the relevant opacity sources. This is considered by Kirkpatrick et. al. (1993). At present however, it appears that such an approach is restricted by our limited knowledge of some molecular opacities, most notably water vapour. Until the model atmosphere approach has been properly refined, the best method for determining T_{eff} is the constant water vapour opacity method of Jones et. al. (1994). The disadvantage of this method is that it requires a complete infrared 1–2.5μm spectrum. While obtaining such spectra is possible for faint Pleiades objects it is a slow process, requiring $\sim$ 4 hours per object. The application of this method to the two Pleiades objects for which complete infrared spectra are available is considered in Chapter 6.

However, in order to investigate the efficiency of various methods of determining effective temperature (such as colours, line strengths etc.), it is not necessary to have an absolute calibration of T_{eff}. It is sufficient merely to order the spectra from hottest to coolest. To order the spectra the procedure devised by Kirkpatrick et al. (1991 - K91) was followed. The following description of the method is an abbreviated version of the one given in their paper.

First the spectra are normalized to a mean F_ν of 1.0 between 7490 Å and 7510 Å (a region of near continuum). The spectra are then run through a least squares minimization program. This program was written according to the algorithm given by K91. Briefly, the program compares each normalized spectrum with all of the other normalized spectra by computing the flux difference for each spectral element between the two spectra. It then calculates the sum of the squares of these differences for each pair of spectra. Because of noise in the spectra, the normalization at 7500 Å may not have been perfect. Each spectrum is therefore multiplied by a number between 0.75 and 1.25 (typically in the range $\sim 0.95 - 1.05$) until a minimization of the squared differences between it and the spectrum being matched is found.

The program was run on the full dataset described in Section 5.1, which contained in addition to the Pleiades sample the selection of M dwarf spectral standards. The comparison was done using the 'red' spectra over the range 5000 – 9000 Å. The least squares values output by the program were used to match spectra to their nearest neighbours in terms of T_{eff}. To order neighbours a combination of two methods was used.

The first method repeated the least squares minimization process for two sub-regions of the spectra, from 5000 – 7000 Å and from 7000 – 9000 Å. Comparison of the normalization constants for these two regions allows a comparison of the overall 'redness' of the spectra as described by K91 and therefore can be used to order nearest neighbours. The second method, which was found to be almost as reliable, was simple overlaying of the spectra for 'ocular estimation'. The final order presented here was derived using a combination of the two methods. Most of the spectra were ordered using the automatic method. Certain noisy spectra however did not appear to have a nearest neighbour, as the effect of noise on a spectrum is to increase the least squares deviation of it from all the other spectra. These spectra were therefore inserted into the spectral sequence by eye.

Figures 5.2, 5.3, 5.4 and 5.5 plot all of the 'red' spectra in the order resulting from the above method, and assigns spectral types to our Pleiades objects based upon the spectral types of the M dwarf standards. The spectra are all normalized to a flux (F_ν) value of 1.0 at 7500 Å and, for the purposes of the figures offset by either 1.0 or 1.5 from each other. The temperature sequence is immediately apparent.

One object, HHJ18, which has the reddest $I - K$ of the candidates of Chapter 4 could not be fitted in the spectral sequence, its flux distribution being unlike any of the other objects. Fig. 5.6 shows the spectrum of HHJ18 (solid line) and that of HHJ12 (dotted line) overlayed. Note how until 8000 Å the spectra agree well. However, between 8000 and 9000 Å some additional opacity source appears to be operating in HHJ18. The additional opacity is not likely to be due to TiO or VO since below 8000 Å these features seem no stronger than those in HHJ12. Above 9000 Å the object does not appear particularly red, being bluer than HHJ2 and HHJ6 here. It is therefore unlikely that the object is very cool, and the additional opacity

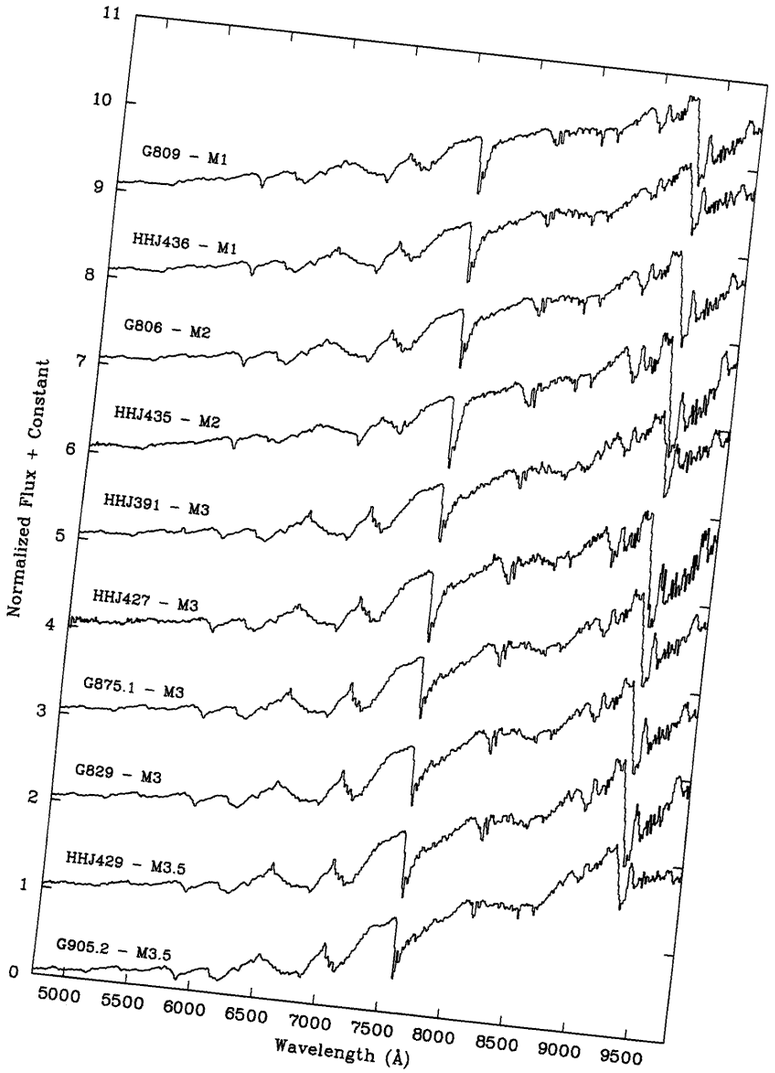

Figure 5.2: Spectral Sequence (first page).

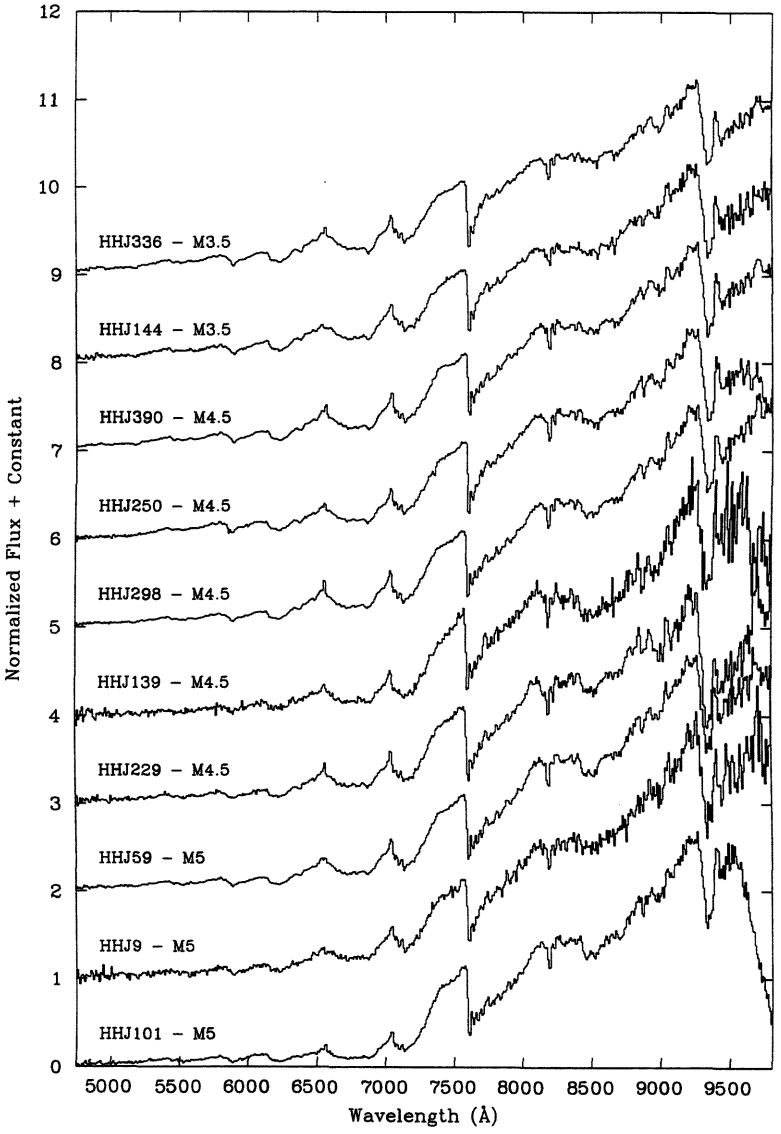

Figure 5.3: Spectral Sequence (second page).

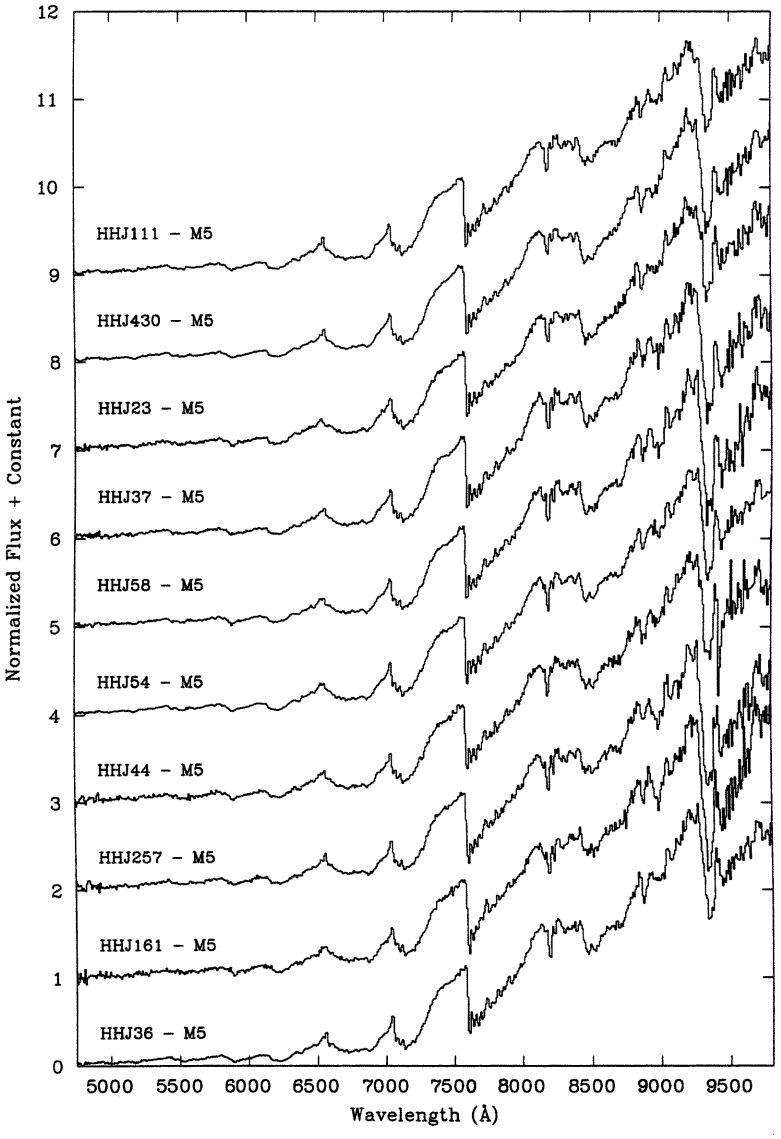

Figure 5.4: Spectral Sequence (third page).

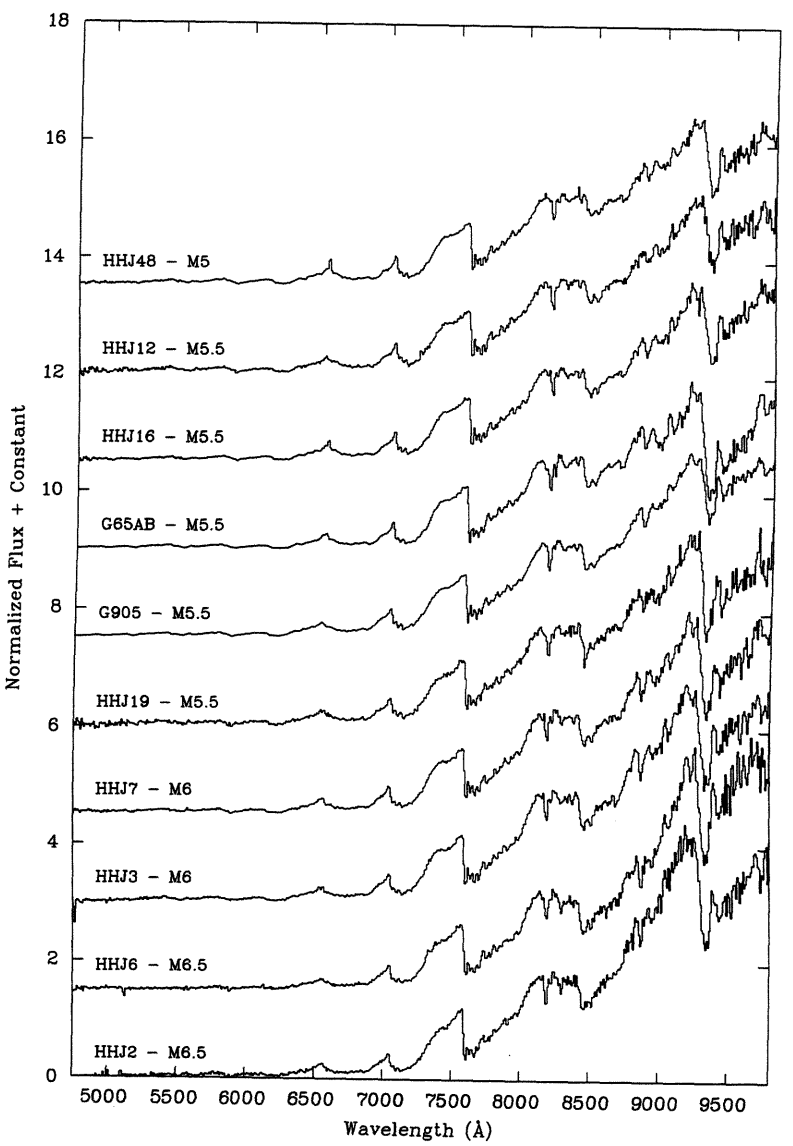

Figure 5.5: Spectral Sequence (final page).

due to some species that only forms at very low temperatures. At present therefore I can propose no explanation for the anomalous flux distribution of this object (in Section 5.4 below I consider, and rule out, unresolved multiplicity in the object). Note however that the region 8000–9000 Å roughly corresponds to the Cousins I band, and therefore HHJ18 will appear underluminous at I compared to the other cluster members. This is undoubtably the cause of the large $I - K$ of this object.

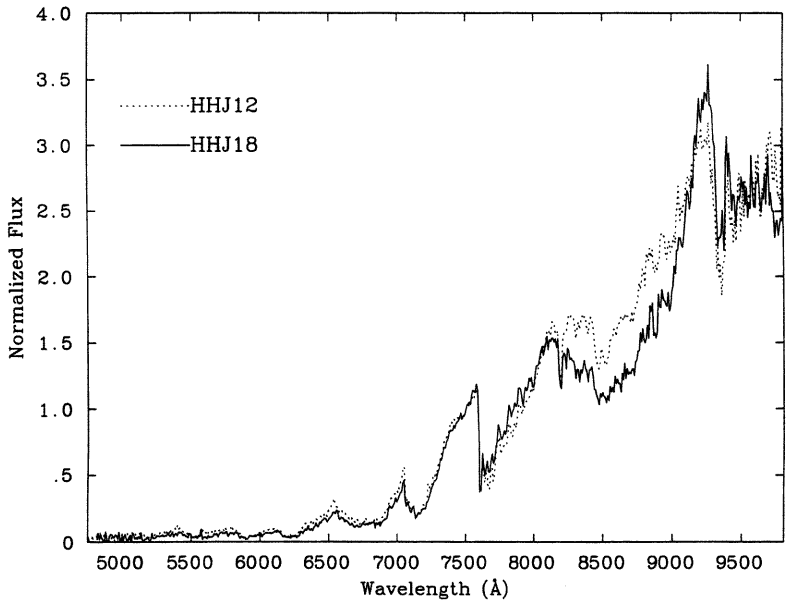

Figure 5.6: The spectra of HHJ18 (solid line) and HHJ12 (dotted line).

5.3 Temperature and Gravity Indicators

5.3.1 Spectroscopic Temperature Indicators

The spectral classifications derived from the method described above can be used to test the effectiveness of various proposed temperature indicators for low mass stars as applied to the Pleiades. K91 propose four ratios (A to D) based on the relative

Ratio	Numerator	Denominator	Feature Measured
A	7020-7050Å	6960-6990Å	CaH 6975Å
B	7375-7385Å	7353-7363Å	TiI 7358Å
C	8100-8130Å	8174-8204Å	NaI 8183,8193Å
D	8567-8577Å	8537-8547Å	CaII 8542Å

Table 5.2: Wavelengths for Ratios defined by Kirkpatrick et. al. (1991)

strengths of various atomic and molecular features to nearby 'continuum' which measure both temperature and luminosity. The features measured by these ratios and the regions over which the flux was summed to carry out the measurements are given in Table 5.3.1. K91 calibrate their fluxes in wavelength units (F_λ) and I have naturally converted the spectra to these units before measuring the ratios. The derived ratios are listed in Appendix C.

Fig. 5.7 plots the measured ratios against spectral subclass. In all cases the general appearance and trends in these plots are similar to that found for the field M dwarf sample by K91. In particular note that all of the objects observed lie on the loci defined by K91 for dwarfs (*not* giants), providing further evidence that our Pleiades sample is not contaminated by distant giants. The best discriminant of T_{eff} appears to be ratio A, based on the CaH 6975 Å feature. This feature is however contaminated by a terrestrial O_2 B band and the large spread around M5 however shows that even this feature will not be totally reliable.

Hamilton & Stauffer (1993 - HS93) observed a small sample of possible Pleiades members from the survey of Stauffer et al. (1989). They also define some useful spectral indices in terms of spectra calibrated in AB magnitudes (Oke & Gunn 1983). These are

$[TiO]_1 = AB(7150) - AB(7560)$

$[TiO]_2 = AB(7590) - AB(8120)$

$[TiO]_3 = AB(7590) - AB(7560)$

$[TiO]_4 = AB(8450) - AB(8120)$

$[VO] = AB(7450) - AB(7560).$

All of these indices measure the depth of a particular feature relative to pseudo-continuum points at either 7560 Å or 8120 Å. In addition HS93 use these two points to define a pseudocontinuum index

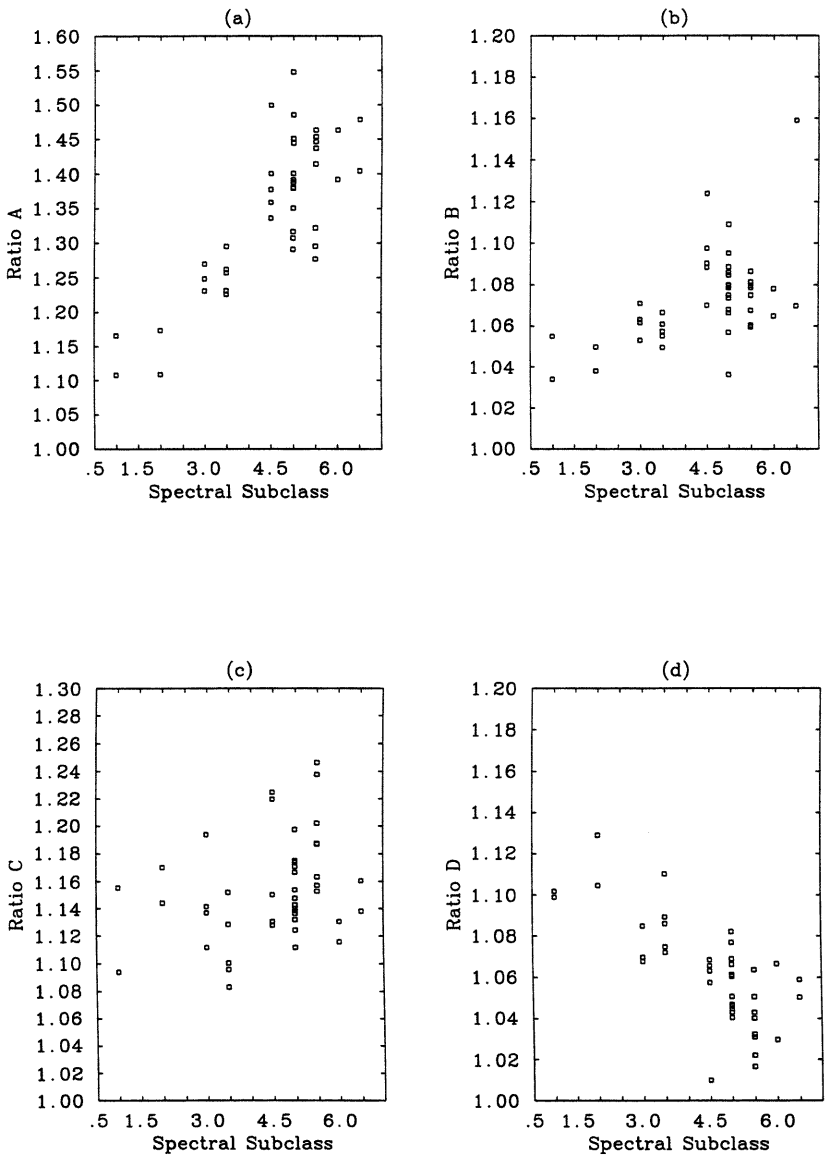

Figure 5.7: Ratios A to D as defined by Kirkpatrick (1991) for the Pleiades and field star sample.

$[PC] = AB(7560) - AB(8120)$.

In order to measure these indices the spectra were converted to AB magnitude units. The derived indices are again listed in Appendix C. Figures 5.8 and 5.9 plot the values of these indices. From these figures it appears that the TiO indices $[TiO]_1$ and $[TiO]_4$ correlate best with the spectral sequence (ie. T_{eff}). HS93 found that $[TiO]_3$ correlated best with T_{eff} derived from the temperature scale of Berriman & Reid (1987). This temperature scale has since been shown to be inaccurate for cooler stars (Jones et al. 1994, see Section 3.2) and hence I do not attribute any great importance to this difference.

The $[VO]$ index appears to correlate very well with the spectral sequence, especially for the coolest objects. This is as expected since for very cool stars it is well known that the strength of the VO bands increases rapidly (Bessell 1991).

The $[PC]$ index, measuring the near continuum slope between 7560 and 8120 Å, also appears to correlate well with the spectral sequence. This index was also found to correlate well with T_{eff} (again from Berriman & Reid 1987) by HS93. For the very coolest stars (M6.5) however, the index appears to start to fall again. This effect can be seen in the spectra. For HHJ6 and HHJ2, which I have classified as M6.5, the flux in the 8100–8300Å region is lower than for the hotter M6 HHJ3 and HHJ7. This is presumably due to the very strong TiO absorption features in this region. However around 8900–9100Å the flux for the M6.5 objects is greater than in the M6 objects. A second PC index was therefore defined based on the flux at the pseudocontinuum point at 9040Å:

$[PC]_2 = AB(7560) - AB(9040)$.

This index is also listed in Appendix C and plotted in Fig. 5.9 and, as might be expected with its longer wavelength base, seems better at classifying the coolest stars than the $[PC]$ index.

Also note that in general the indices of HS93 seem to have lower intrinsic spread in them than the ratios of K91. A possible explanation for this will be discussed in Section 5.4 below.

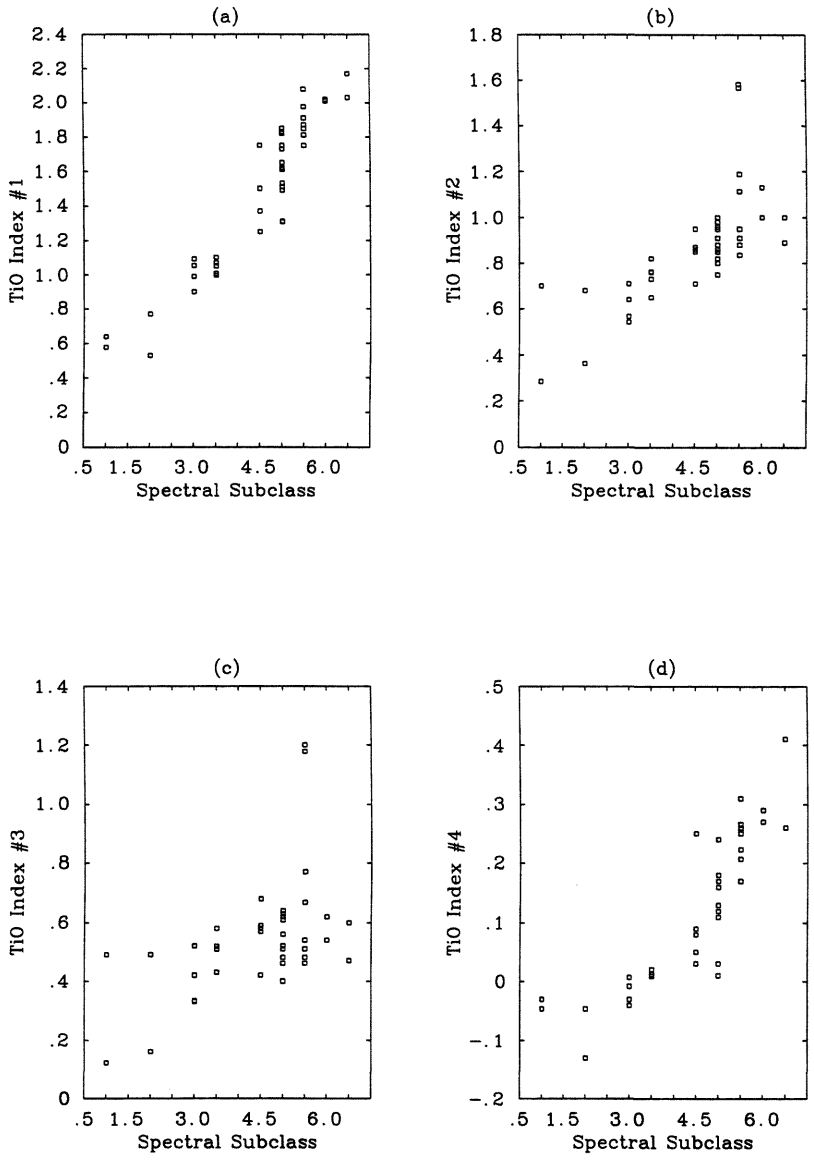

Figure 5.8: The [TiO] indices defined by Hamilton & Stauffer (1992).

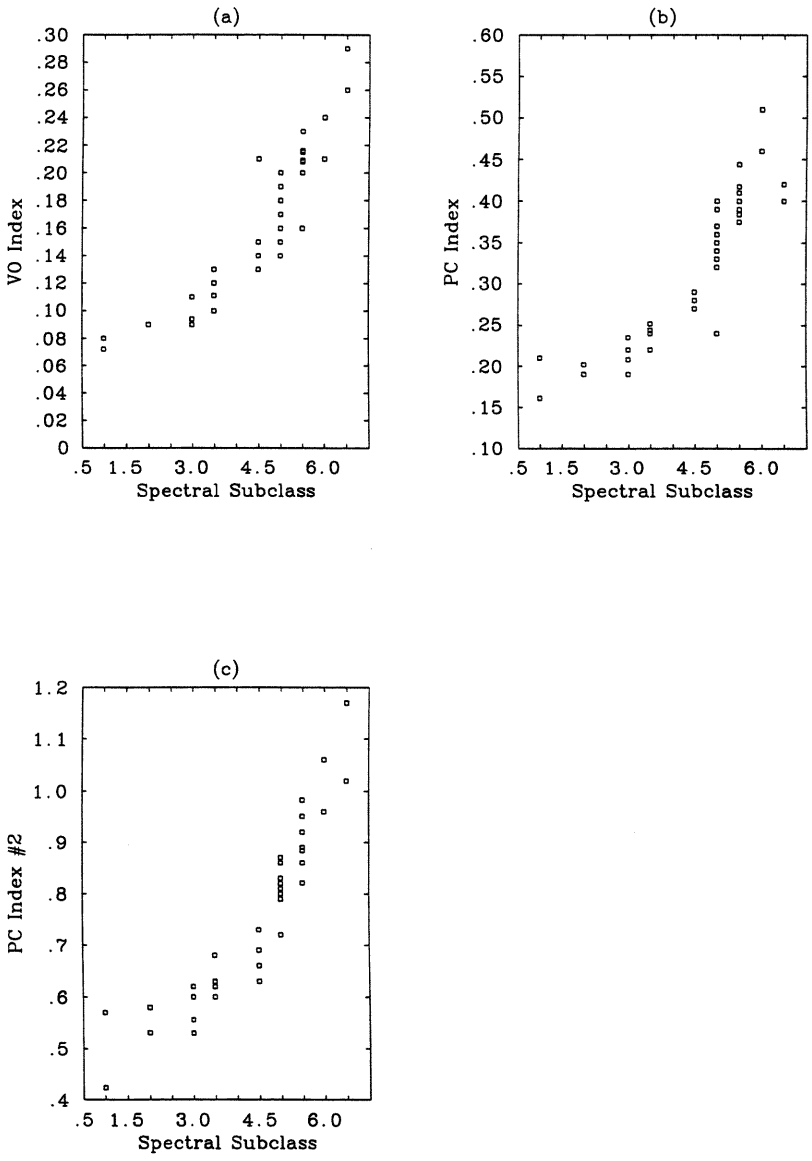

Figure 5.9: [VO] and [PC] indices from Hamilton & Stauffer (1992) and the new [PC2] index.

5.3.2 Photometric Temperature Indicators

On the basis of the spread in a plotted colour magnitude diagram in Section 4.3 I claimed that the $I-K$ colour was a more reliable measure of T_{eff} than $R-I$. This is not an unexpected result, given the longer wavelength base of the $I-K$ colour and the fact that the peak of a $\sim 2500K$ black body lies in the region of the H and K bands. The spectral sequence allows a test of that result and also of the effectiveness of other colours as temperature indicators.

Fig. 5.10 therefore plots (a) $R-I$, (b), $I-K$, (c) $H-K$ and (d) $J-H$ as a function of spectral subclass. Open squares signify Pleiades objects which have JHK photometry listed in Appendix B. Filled squares are the sample of field dwarfs, with photometry from Leggett (1992) converted to the UKIRT system using the transforms provided in Appendix 2G of that paper.

From the plots both $R-I$ and $I-K$ appear to be reasonable temperature indicators. The scatter in $I-K$ is slightly less although at the latest types this index begins to saturate. The relatively large spread at these late spectral types ($\sim$ 0.4 mag.) may be due to unresolved binarity distorting the $I-K$ colours of some objects. This will be considered in Section 5.4 below. $R-I$ has a slightly larger intrinsic spread but does not appear to saturate. This large spread may in part be due to the larger photometric error of the $R-I$ colour ($\sim \pm 0.25$ mag.) as compared with $I-K$ ($\sim \pm 0.12$ mag.), since both the R and I magnitudes are mainly photographic in origin.

$H-K$ also appears to be a reasonable temperature indicator. This colour however suffers from photometric errors that are large ($\sim$ 0.1 mag.) compared with the value being measured ($\sim$ 0.3). $J-H$ is a known metallicity indicator (Leggett 1992), the spread in the field stars in this diagram reflecting their metallicity differences. One would expect the Pleiades objects to all have the same metallicity, however the spread in this plot is greater than can be explained by the estimated photometric error ($\sim \pm 0.1$ mag.). Therefore either metallicity variations exist amongst low mass Pleiades members or some other effect which will distort the $J-H$ colours is operating.

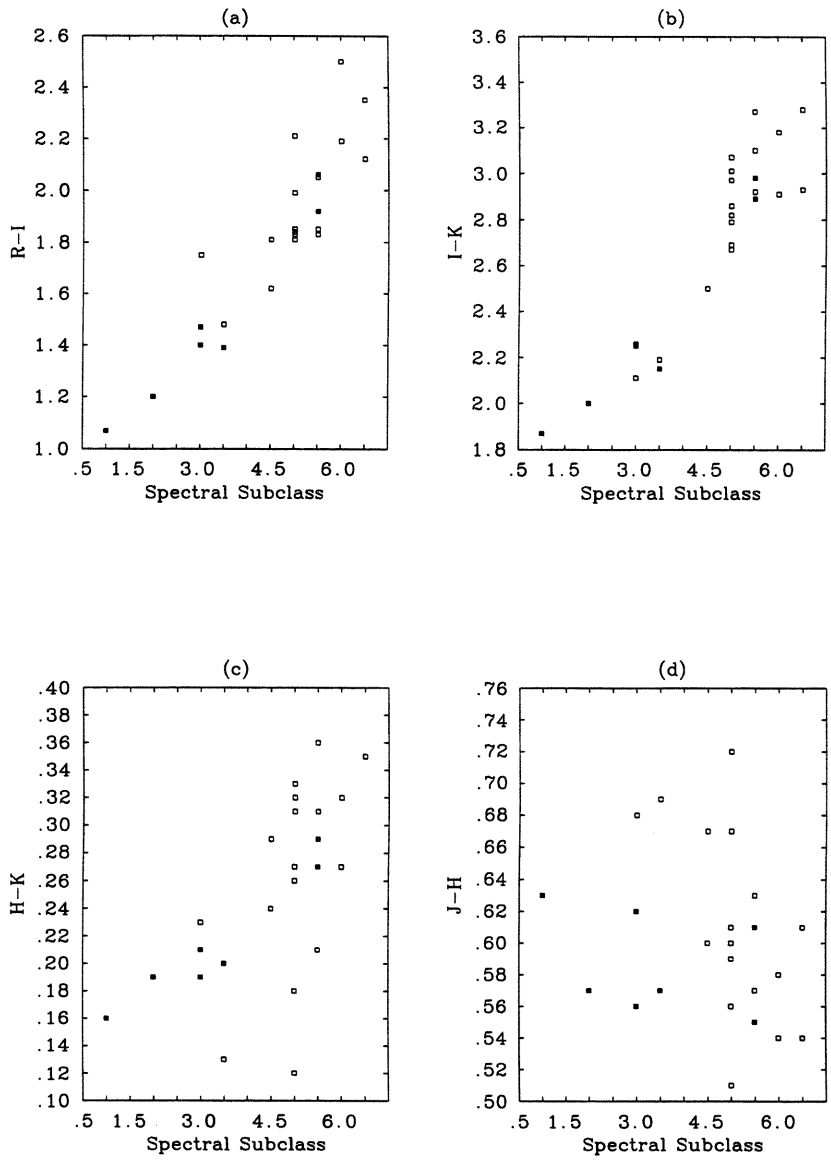

Figure 5.10: Photometric Colours versus Spectral Subclass. Filled symbols indicate standards, open symbols Pleiades members.

5.3.3 Spectroscopic Gravity Indicators

An obvious difference between Pleiades and field stars is age. Since the young, lower mass Pleiades objects in the sample are still contracting towards the main sequence, one would expect them to have lower surface gravities than a main sequence object of the same T_{eff}. Stringfellow's (1991) models predict that a $0.1M_{\odot}$ object at the Pleiades age will have a surface gravity $g = 2.23g_{\odot}$ ($\log g = 4.79$). Jones et. al. (1994) estimate that a $0.1M_{\odot}$ main sequence object has $g = 4.50g_{\odot}$ ($\log g = 5.09$), i.e., ~ 2 times greater.

The NaI doublet at 8183 and 8195 Å is a well known indicator of surface gravity for cool objects, the equivalent width (EW) of the doublet increasing with increasing gravity. Using this doublet one can therefore estimate the surface gravity of the objects in the sample. Mould (1978) shows that for a gravity difference of factor 10 (between $\log g = 5.75$ and $\log g = 4.75$ at 3500K), the NaI EW changes by a factor of 1.7. Theoretical models from Allard (priv. com.) which she has kindly supplied show that at 2800K for a gravity change of factor 5 ($\log g = 4.44$ to $\log g = 5.14$) the NaI EW changes by a factor of 1.2. A factor 2 difference in g should therefore result in a NaI EW change of $\sim 1.1 - 1.2$ times.

Figure 5.11 plots NaI equivalent width versus Spectral Subclass. The estimated error in the EW determinations is $\sim$ 1Å. Again the Pleiades objects are shown as open squares, whereas the field objects are shown as filled squares. Note that for the lower mass objects of M5.5 the NaI EW for the field dwarfs is significantly greater (by a factor of $\sim$ 1.3) than for the Pleiades objects, roughly in line with the prediction given above. No difference is apparent for the objects earlier than M4. This implies that Pleiades objects of M3.5 have reached the main sequence whereas objects of M5.5 have not. The models of D'Antona & Mazzitelli (1985) (since Stringfellow's (1991) models do not extend above $0.2M_{\odot}$) predict that for the Pleiades age (70 Myr) objects with the colours and luminosity of M3.5 objects have masses $\sim 0.35M_{\odot}$ and M5.5 objects have masses $\sim 0.1M_{\odot}$. D'Antona & Mazzitelli (1985) (their Fig. 1) also show that objects of above $0.3M_{\odot}$ lie very close to the zero-age main sequence. Hence these observations of Pleiades objects nearing the

main sequence somewhere between M3.5 and M5.5 are consistent with a Pleiades age of 70 Myr and the masses derived from theory for these objects.

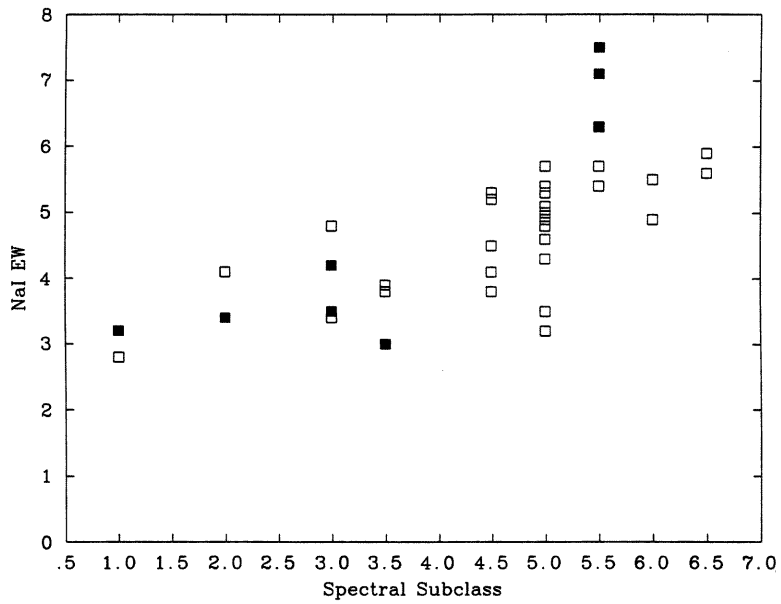

Figure 5.11: Na Equivalent width versus Spectral Subclass. Filled symbols are standards, Open symbols Pleiades members.

5.4 The Effect of Multiplicity

The discussion in this chapter so far has assumed that all of the objects observed are single. This is almost certainly not the case. In Chapter 4 I showed how the $I, I-K$ diagram allowed the identification of a sample of likely binary objects, as they lay on a binary sequence (BS) 0.75 magnitudes above the single star sequence (SSS). Unresolved binarity (and higher degrees of multiplicity) will naturally affect the spectroscopy of the sequence . In this section I will discuss how these effects may be modelled and the effect they have on the spectral sequence and the indicators derived from it.

The effect of binarity on the FOS spectra may be modelled by addition of spectra of single objects to produce an artificial binary. Fig. 5.12 shows the results of adding the flux calibrated spectra of HHJ2 (M6.5, $\sim 0.07M_{\odot}$) to that of HHJ23 (M5, $\sim 0.12M_{\odot}$), the resulting spectrum being normalized to 1.0 at 7500 Å. Also plotted in Fig. 11 is the original spectrum of HHJ23 (solid line). It can be seen that the effect of HHJ2 on the combined spectrum is fairly small until around 9000 Å, where the spectrum becomes significantly redder. This is as expected, since the lower mass object, being cooler, will naturally contribute relatively more flux at longer wavelengths. In the regions of the spectra where the molecular absorptions are particularly strong (e.g. around 7600 and 8500 Å) the spectra of the single object and artificial binary coincide. This is because in these regions the cooler, lower mass object will suffer greater absorption than the higher mass object, effectively 'canceling out' its higher relative underlying flux at these wavelengths.

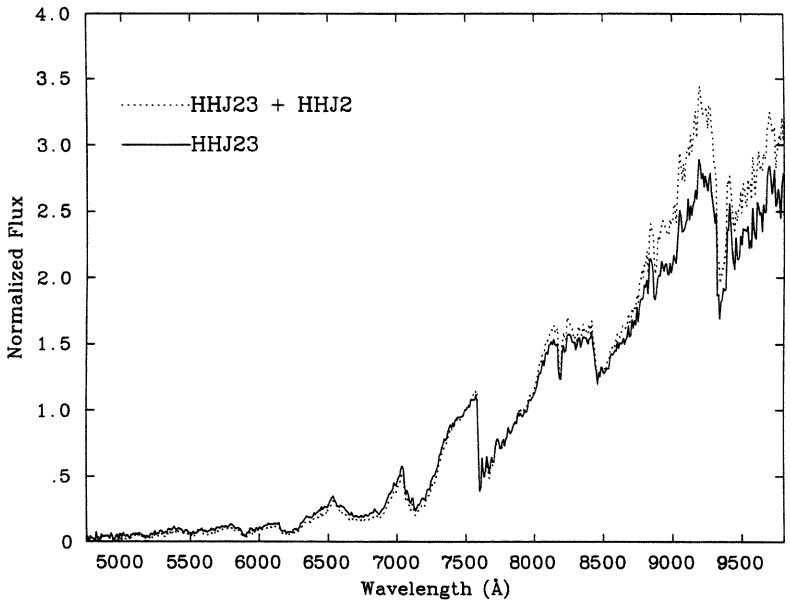

Figure 5.12: Artificial Binary Spectrum.

This will obviously affect the derivation of the spectral sequence as outlined in

Section 5.2. Kirkpatrick & McCarthy (1994) investigated the effect of an unresolved cooler companion on the least squares minimization technique of K91 and found that it changed the spectral type of the higher mass object by only half a subclass (see their Figs. 3, 4 and 5). Running the artificial binary though the least squares minimization program, places it in the spectral sequence next to HHJ16, i.e. a spectral type of M5.5. Again this is only half a subclass redder than the true spectral type of the primary. The effect of unresolved binarity on the spectral sequence is therefore relatively small. While it is possible to redo the spectral sequence for those objects which were photometrically determined in Chapter 4 to be single, in practice such a sequence would only contain 8 Pleiades objects. I therefore prefer to continue to use the full sample while being careful to recognize its limitations.

In principal it should be possible to use the single star spectra in an attempt to deconvolve the spectra of the suspected binaries. This is limited by the fact that the position of an object on the binary star sequence is not unique (for example HHJ28 could be composed of 0.08+0.08, 0.09+0.07 or 0.10+0.06 $M_{\odot}$) and a lack of single objects with masses less than $0.07M_{\odot}$. In addition the differences between the binary and single star spectra can be seen to be relatively small from Fig. 4.6. The differences will be much larger for CGS4 1-2.5 micron spectra and I will discuss attempts to detect these differences in the following chapter.

How will unresolved binarity affect the spectroscopic indicators discussed in Section 5.3.1 ? Because of the 'cancelling out' effect mentioned above, spectral indices based on strong absorption features such as the $[TiO]$ and $[VO]$ indices defined by HS93 should be largely unaffected by unresolved binarity. They should hence remain effective in determine the spectral type of the higher mass star (primary). In order to test this I have measured the indices for the artificial binary as compared to HHJ23 alone, and find that $[TiO]_1$ index is increased by an amount corresponding to half a subclass, the other $[TiO]$ indices remaining unaffected. The $[VO]$ index is increased by one subclass – this is probably the origin of the large vertical scatter in this plot.

The ratios of K91 are based on atomic lines. Examination of the artificial binary spectrum shows that the strengths of these lines changed with respect to HHJ23.

This is not surprising as the strength of these lines is not as strong a function of temperature as the molecular bands. In one case (Ratio D), the strength of the line *decreases* with decreasing T_{eff}. In this case there is no chance of a 'cancelling out' effect. Unresolved binarity therefore appears to provide an explanation for the greater spread in the K91 ratios compared with the HS93 indices noted in Section 5.3.1. Again to test this supposition ratios A to D were measured for the artificial binary. Ratios A and B were increased by an amount corresponding to half a subclass.

It therefore appears that both the indices of HS93 and the ratios of K91 are relatively unaffected by unresolved binarity and may be used with relative confidence to classify low mass stars of unknown multiplicity.

I also note that HS93's relatively short wavelength $[PC]$ index is unaffected by the artificial companion. The longer wavelength $[PC]_2$ index is naturally more affected and should not be used for stars which are not known to be single.

The anomalous spectrum of HHJ18 was noted in Section 5.2 above. It position in the $I, I-K$ diagram (well to the right of the BS) suggests it may be a triple (or greater!) system, but I have already shown that its very red $I-K$ is not due to excess luminosity at K which would indicate multiplicity, but to an underluminosity solely at I, which does not. It is also hard to imagine a multiple system that would give the observed optical flux distribution, since the primary anomaly is simply a flux deficit in a certain wavelength range. Multiplicity does not therefore explain the observed flux distribution of this object.

5.5 Activity and the nature of the Magnetic Dynamo

Hα is a well known indicator of chromospheric activity in low mass stars, whereas coronal activity may be measured using X-ray fluxes. The mechanism (dynamo) providing the energy input to the chromospheres of late type stars is uncertain. For objects greater than $0.3M_{\odot}$, which have a radiative core and convective envelope a 'shell dynamo' is the favoured mechanism (Parker 1975, Golub et. al. 1981). In this

mechanism it is the sheer layer between the core and the envelope that is responsible for concentrating the field lines and thus driving the heating mechanism. Objects of less than $0.3M_{\odot}$ are fully convective (Liebert & Probst, 1987) and therefore the shell dynamo mechanism can not be operating. Some form of 'distributive dynamo' is therefore presumed to operate (Rosner 1980). A change in activity should therefore be observed at around $0.3M_{\odot}$ due to the change in dynamo mechanisms.

Previous attempts to investigate the nature of low mass stars have relied on samples constructed from the solar neighbourhood (Giampapa & Liebert 1986, Fleming & Giampappa 1989, Liebert et. al., 1992). The problem with this approach is that the varying ages and metallicities of the objects in the sample make attempts to disentangle effects due to mass difficult. I have shown that the photometry of low mass Pleiads shows that all of the objects may be coeval and found no firm evidence of metallicity variations within the cluster members. The Pleiades sample of HHJ91 therefore makes an ideal testbed for stellar dynamo theories.

5.5.1 Chromospheric Activity

In Figure 5.13 I plot $H\alpha$ equivalent width (EW) for the FOS Pleiades sample (filled circles) versus M_I (absolute I magnitude). Also plotted (open circles) are higher mass Pleiades objects whose EW had been previously measured by Prosser, Stauffer & Kraft (1991), Stauffer & Hartman (1987) and Stauffer (1980). EWs were measured using the FIGARO routine ABLINE (Robertson 1986) with respect to an interpolated continuum at 6563Å. The estimated error in the EWs is $\sim$ 1Å. $H\alpha$ EWs were also measured with respect to the pseudo-continuum point at 6530 Å(K91). The effect of this was to decrease the EW by between 3% (hottest object) and 20% (coolest object). In both cases this is a smaller error than the estimated 1Å error in the measurements. The EWs relative to 6563Å are therefore preferred in this analysis since this was (presumably) the procedure adopted by the previous investigators of the higher mass sample. The measured EWs are listed in Appendix C.2.

Also plotted on Figure 5.13 are the theoretical models of D'Antona & Mazzitelli

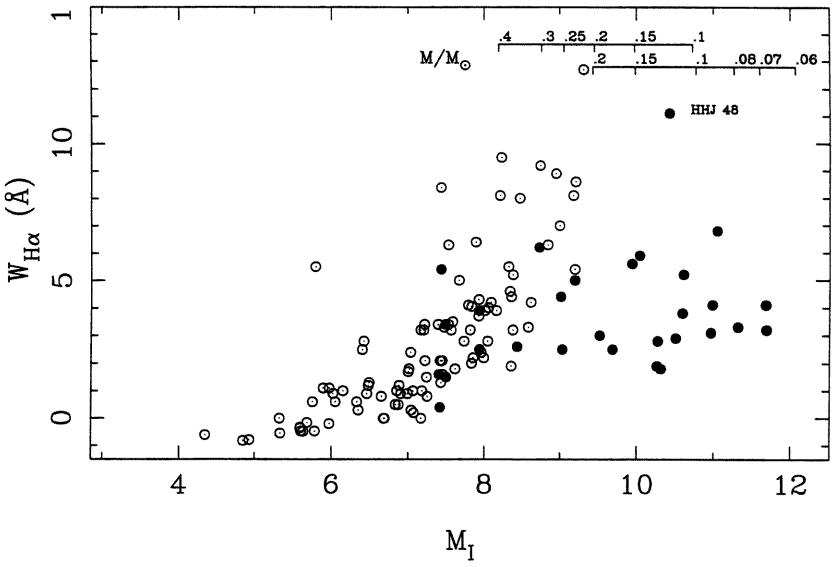

Figure 5.13: $EW_{H\alpha}$ versus M_I. Filled symbols are FOS measurements, open circles are measurements from previous surveys.

(1985) (upper line) and Burrows et. al. (1993) lower line, converted to the observational plane using the bolometric correction of Bessell (1991). The agreement between the models in the region of overlap is encouraging. The model of Stringfellow (1991) used previously also agrees well with the others. D'Antona & Mazzitelli (1985) is plotted since only this model extends above $0.2M_\odot$.

Three obvious features are apparent in Figure 5.13:

1. A diagonal upper bound to H_α EW as a function of M_I.

2. An apparent turnover in $H\alpha$ EW in the region $M_I = 8 - 10$

3. An increase in the lower bound with fainter M_I.

There may however be a selection effect in this diagram. The objects from previous surveys were in general detected as flare stars, whereas the FOS measurements are of a sample which is a random subset from the essentialy complete HHJ91 sample of fainter Pleiades members. Therefore by the criteria for their selection, the previous object sample may tend to have larger EWs than the FOS sample. Possible

evidence for this may be seen in the overlap region between the two samples, where the average EW for the flare stars appears greater than that for the FOS sample.

Another important limitation of Figure 5.13 is that as one goes to fainter M_I (and therefore lower masses) the photospheric continuum flux will rapidly decrease, leading to an increased EW for the same line luminosity. Since line luminosity is presumably the more fundamental parameter, it would be preferable to use this quantity rather than EW. Herbig (1985) shows that emission line flux received from a $H\alpha$ source may be calculated using

$$f_{H\alpha} = 3.8 \times 10^{-9} \times EW \times \frac{F_\lambda(6563)}{F_\lambda(5556)} \times 10^{-0.4V} \tag{5.1}$$

where $\frac{F_\lambda(6563)}{F_\lambda(5556)}$ is the ratio of the continuum at $H\alpha$ to the continuum at the centre of the V band and V is the apparent magnitude in that band.

The continuum ratio was measured for all of the FOS spectra and a least squares fit of this ratio to $R-I$ carried out:

$$\frac{F_\lambda(6563)}{F_\lambda(5556)} = 2.786(R-I) - 0.932. \tag{5.2}$$

This allows line luminosities to be calculated not only for the objects in the FOS sample but also for the objects observed by previous investigators who have only published EW's and colours.

Figure 5.14 therefore shows the distribution of $L_{H\alpha}$ with M_I. $L_{H\alpha}$ is constant out to $M_I = 8-9$, then beings to fall off. However, this effect may be simply due to the smaller radii of the lower mass stars. In order to remove the surface area effect Figure 5.15 plots $L_{H\alpha}/L_{bol}$. This ratio is the fraction of total energy output in $H\alpha$ and therefore a good indicator for chromospheric heating efficiency. Note that the turnover around $M_I \sim 9$ still remains. This can be seen to correspond to masses around $\sim 0.25 - 0.3 M_\odot$. It therefore appears that some change in the dynamo mechanism *is* operating around the mass range where the star becomes fully convective, and that the dynamo below this mass is considerably less efficient than the one operating in objects with a radiative core. Note however that there is still chromospheric heating below $0.3 M_\odot$, as the figure does not plummet below this limit but merely turns over. This may be due to some form of distributed dynamo as discussed at the start of this section.

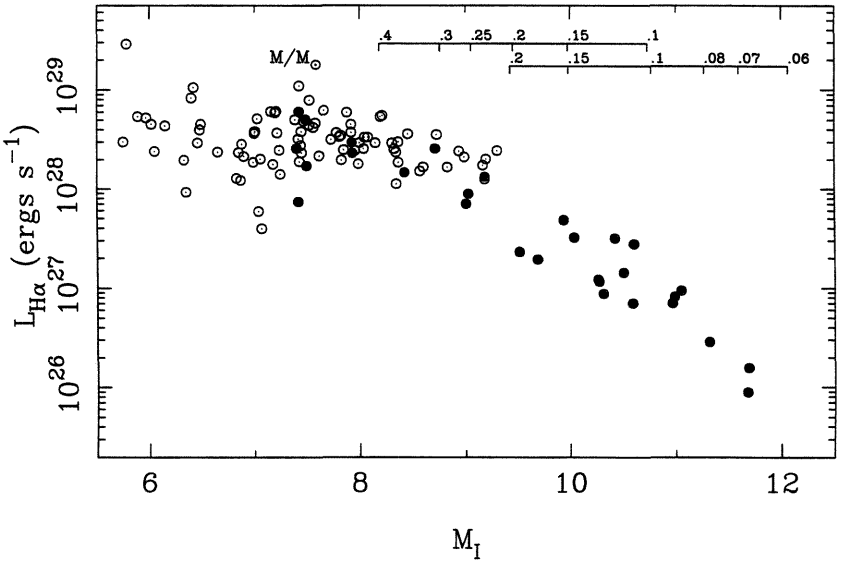

Figure 5.14: $L_{H\alpha}$ versus M_I. Filled symbols are FOS measurements, open circles are measurements from previous surveys.

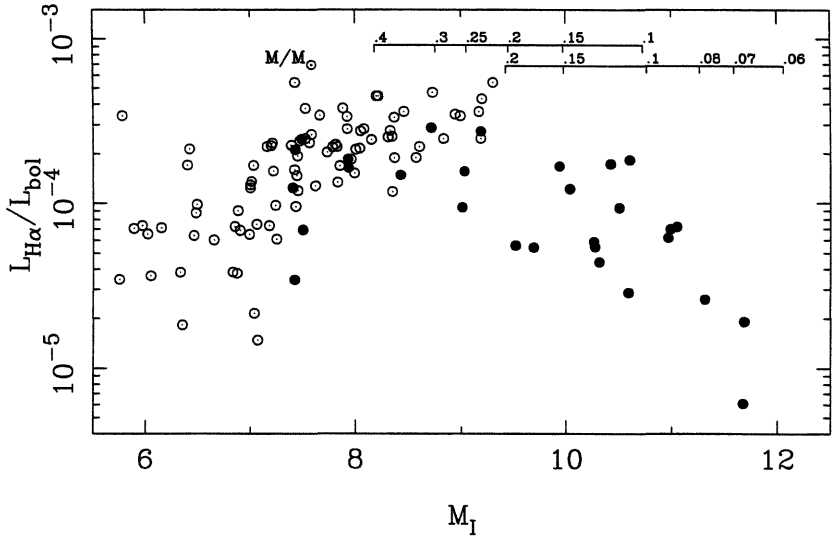

Figure 5.15: $L_{H\alpha}/L_{bol}$ versus M_I. Filled symbols are FOS measurements, open circles are measurements from previous surveys.

Ref. Number	PI	RA_{2000}	DEC_{2000}	Exposure (sec)
200068	Rosner	03 36 48.0	23 54 00	35862
200556	Stauffer	03 50 09.6	24 21 36	25944
200557	Stauffer	03 44 24.0	24 47 24	20868

Table 5.3: ROSAT fields in the Pleiades

5.5.2 Coronal Activity

Hodgkin (priv. com) has carried out a reanalyis of three ROSAT PSPC observations of the Pleiades, listed in table 5.3 and has kindly supplied the results used in this section. More complete details of this work will be published in Hodgkin, Jameson & Steele (1994, MNRAS, submitted). Here I merely give the basic results of the analysis for comparison with the chromospheric analysis presented above.

In the reanalysis each image was binned into 512×512 15 arcsec pixels over the total energy range of the PSPC (0.1-2.4 keV) and analysed using the program PSS (Pye et. al, 1994) with a three sigma detection threshold. This produced a source list with measured X-ray luminosity L_X which was matched with both the HHJ91 catalogue and also a list of higher mass members supplied by Stauffer (priv. com).

In Figure 5.16 I plot L_X/L_{bol} as an indicator of coronal activity. The upper bound in this figure represents the X-ray saturation boundary (i.e. the stellar surface fully covered in active regions) and on first inspection the whole figure seems to indicate increasing coronal activity down to the lowest masses with no indication of a turnover. This would imply different mechanisms are responsible for heating the corona and chromospheres of low mass stars.

However, note that there are in fact many more upper limits than detections plotted in the figure. If only the detections are considered the sample is naturally biased towards the properties of the X-ray bright objects. Further analysis requires the use of survival statistics (Kaplan and Meier 1958, Feigelson & Nelson 1985). This allows the mean of a sample containing upper limits to be estimated in a rigorous fashion. Figure 5.17 therefore plots the estimated mean of $\log L_X/L_{bol}$ versus M_I as supplied by Hodgkin (priv. com). The expected turnover can now be seen at around $M_I \sim 8$, indicating that similar mechanisms *do* appear to operate in heating both stellar coronae and chromospheres. This is the first evidence for a change in the

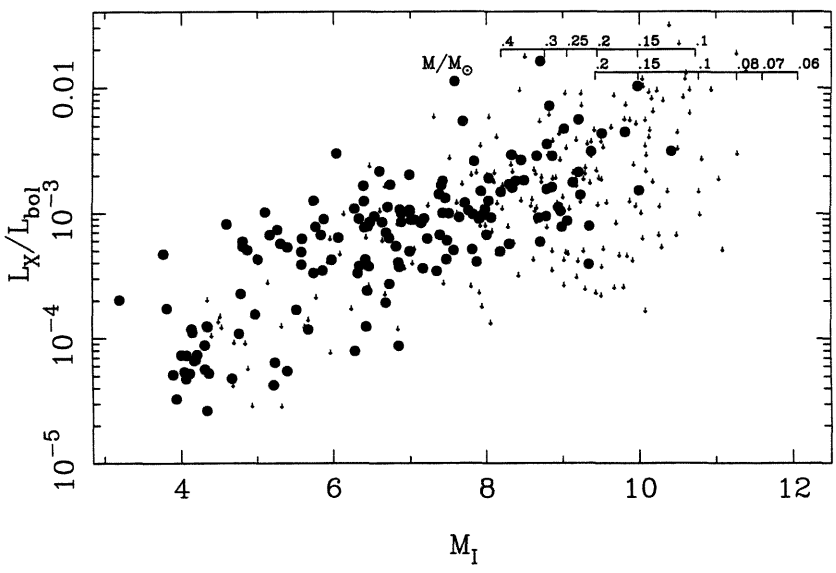

Figure 5.16: L_X/L_{bol} versus M_I.

nature of *both* coronal *and* chromospheric activity at or around the point at which stars are expected to become fully convective.

5.6 Conclusions

In this chapter I have shown how the application of the least squares minimization technique of K91 to optical spectra of a sample of the Pleiades objects of HHJ allows the construction of a spectral sequence and the assigning of spectral types. These spectral types allow an investigation into the effectiveness of various temperature indicators for low mass stars. Both $R-I$ and $I-K$ appear to be reasonable photometric temperature indicators. Of the spectroscopic temperature indicators investigated those based on molecular bands (especially TiO) appear to be better indicators than those based on atomic lines. The NaI 8183/8194Å doublet appears to be a good indicator of surface gravity and its strength for the lower mass Pleiads is consistent with their estimated surface gravities from theoretical models. The effect of binarity on the sequence and temperature indicators has also been investigated.

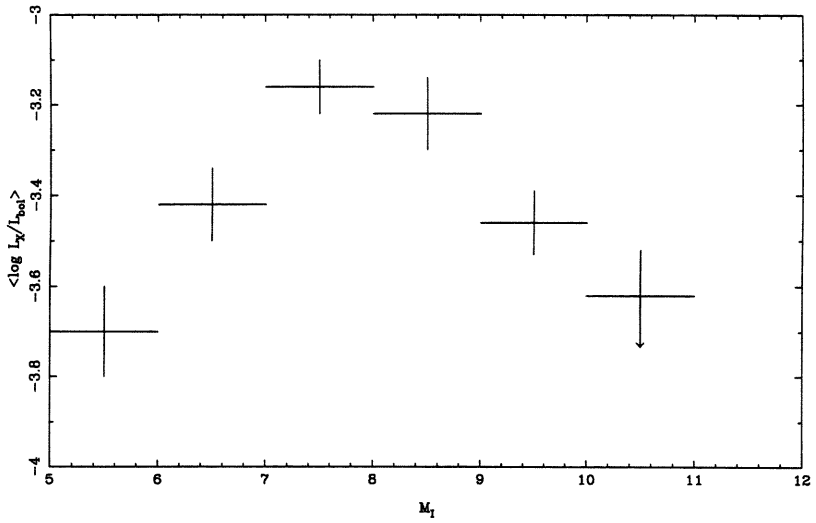

Figure 5.17: log $< L_x/L_{bol} >$ versus M_I.

The effect on the sequence of an unresolved companion is to increase its spectral type by up to half a spectral subclass. A similar effect is found for the spectroscopic temperature indicators. The effect on the photometric indicator $I - K$ is much larger. This is not a problem however as it was this large effect that allowed the initial identification of the binaries. One object (HHJ18) has an optical spectrum which can not be fitted in to the spectral sequence, although it is obviously a cool stellar spectrum. The nature of this object will be considered again in the next chapter, along with infrared spectra of a small sample of low mass Pleiads.

In this chapter I have also shown how the optical spectra of the homogeneous Pleiades sample allows an investigation to be made of the chromospheric properties of low mass stars. $L_{H\alpha}/L_{bol}$ is found to increase with decreasing mass until around $0.3M_{\odot}$. After that the activity begins to decrease. Supplied X-ray fluxes show a similar behaviour in the coronal activity. This implies a change in the nature of the magnetic dynamo when a star becomes fully convective - possibly a transition from a 'shell-type' to a 'distributed-type' mechanism.

Chapter 6

The Pleiades III: Infrared Spectroscopy, Effective Temperatures and Indicators of Binarity

This chapter presents the results of $1 - 2.5\mu$m CGS4 spectroscopy of the low mass stars and brown dwarf candidates of Chapter 4. The spectra are investigated in terms of effective temperature and for indications of binarity.

6.1 Observations

In this chapter I shall consider results obtained using the CGS4 Cooled Grating Spectrometer. The characteristics of this instrument and an outline of the necessary steps in data reduction were given in Chapter 2. The observations were obtained in two observing runs on the nights of 1992 October 28-30 and the night of 1993 December 18. In both cases the short focal length camera and 75 lines/mm grating were employed. This configuration results in a slit width of 3 arcsec. The grating positions employed for the first observing run are listed in table 6.1. Some difficulty was encountered when joining the spectral sections observed during the first run together. Therefore for the second run slightly different positions were used, listed

Central λ (microns)	λ range (microns)
1.07	0.98 - 1.16
1.23	1.13 - 1.33
1.41	1.31 - 1.51
1.59	1.49 - 1.69
1.88	1.68 - 2.07
2.25	2.04 - 2.45

Table 6.1: CGS4 Grating Positions 28/10/92.

Central λ (microns)	λ range (microns)
1.07	0.98 - 1.16
1.21	1.11 - 1.30
1.43	1.34 - 1.50
1.66	1.45 - 1.86
1.90	1.69 - 2.10
2.21	2.00 - 2.41

Table 6.2: CGS4 Grating Positions 18/12/93.

in table 6.2. These positions give a slightly smaller total coverage but a greater degree of overlap between the spectral sections.

For both observing runs the weather was poor, with high cirrus spoiling much data, increasing exposure times and reducing the signal to noise ratio. The resulting dataset presented here is therefore somewhat fragmented. The initial aim of the programme was to obtain complete 1–2.5μm spectra for around 5-6 low mass Pleiads. Due to the poor weather only two complete spectra (HHJ 2 and HHJ3) were obtained plus a number of spectral fragments centred on 1.2μm (containing a large number of molecular and atomic features) and 2.2 μm (containing the temperature sensitive 2.3μm CO features and the edge of the 1.87μm water vapour band). The complete spectrum of HHJ2 is of very poor signal-to-noise ratio but is included for completeness. Tables 6.3 and 6.4 list the observations obtained in the two runs along with exposure times.

The flux standard used for both runs was BS1137. This has $T_{eff} = 9570K$ $V = 6.10$ and spectral type A0 (Popper 1980, Hoffleit & Jaschek, 1982). The maximum difference between the mean air mass of the standard and object observations

ID	1.07μm	1.23μm	1.41μm	1.59μm	1.88μm	2.25μm
HHJ3	29/10/92 960 sec	29/10/92 1200 sec	29/10/92 1200 sec	29/10/92 960 sec	29/10/92 1200 sec	28/10/92 1680 sec
HHJ7	–	–	–	–	–	29/10/92 1200 sec
HHJ16	–	–	–	–	–	29/10/92 960 sec
HHJ36	–	28/10/92 1200 sec	–	–	–	28/10/92 1440 sec
HHJ37	–	30/10/92 1200 sec	–	–	–	–
HHJ54	–	28/10/92 1200 sec	–	–	–	28/10/92 1920 sec
HHJ139	–	30/10/92 960 sec	–	–	–	–
HHJ144	–	30/10/92 960 sec	–	–	–	–
HHJ390	–	–	–	–	–	29/10/92 720 sec
HHJ391	–	30/10/92 960 sec	–	–	–	30/10/92 480 sec
HHJ430	–	30/10/92 1440 sec	–	–	–	–

Table 6.3: CGS4 Observations - 1st run.

ID	1.07μm	1.21μm	1.43μm	1.66μm	1.90μm	2.21μm
HHJ2	18/10/93 1680 sec	18/10/93 1680 sec	18/10/93 1680 sec	18/10/93 1680 sec	18/10/93 1680 sec	18/10/93 1680 sec
HHJ6	–	–	–	–	–	18/10/93 720 sec
HHJ18	–	–	–	–	–	18/10/93 720 sec

Table 6.4: CGS4 Observations - 2nd run.

was never more than 0.1. Atmospheric features should therefore have been effectively removed from the spectra. The spectra were reduced following the standard procedures outlined in Chapter 2, with wavelength calibration being carried out using the CGS4 argon lamp. The mean rms error in the wavelength calibration was $< 0.01\mu$m in all cases.

After reduction the spectra were smoothed using a gaussian filter of total width 5 pixels and full width half maximum 3 pixels. This improves the general appearance of the spectra and makes it easier to distinguish spectral lines. Care was taken when doing this not to alter the equivalent widths of any spectral features present, although the actual widths of the features are often considerably broadened. Many of the apparent features in the fainter objects are simply noise. The features in the spectra of the brighter objects (HHJ36 and above) are however real, and can all be identified with known (and expected) atomic and molecular species by comparison with spectra of Jones et al. (1994 - JLJM94).

Figure 6.1 shows the complete 1.0–2.5μm spectra of HHJ2 and HHJ3 (fluxed with HHJ3 offset by 2 mJy). As expected the spectra are dominated by deep, water vapour absorption bands centered at 1.45, 1.87 and 2.6 μm. There are also many strong molecular and absorption features. These have been identified on the figure by comparison to the spectra of JLJM94 and Kleinmann & Hall (1986). Figures 6.2 and 6.3 show the 1.2 and 2.2 micron spectral fragments obtained. For the purposes of the plot the 1.2 micron spectra have been normalized to 1.0 at 1.22 microns and then 'stretched' about Flux 1.0 by a factor of 4 for clarity. They are also plotted offset by 1.0 normalized flux unit from each other. The same procecedure was applied to the 2.2 micron spectra, but in this case the normalization was at 2.1 microns and 'stretch' factor was 3.

6.2 The determination of Effective Temperature

In Section 3.2 the difficulty of assigning accurate T_{eff}'s for cool objects was demonstrated. In the absence of complete model atmospheres (Allard 1990), the best

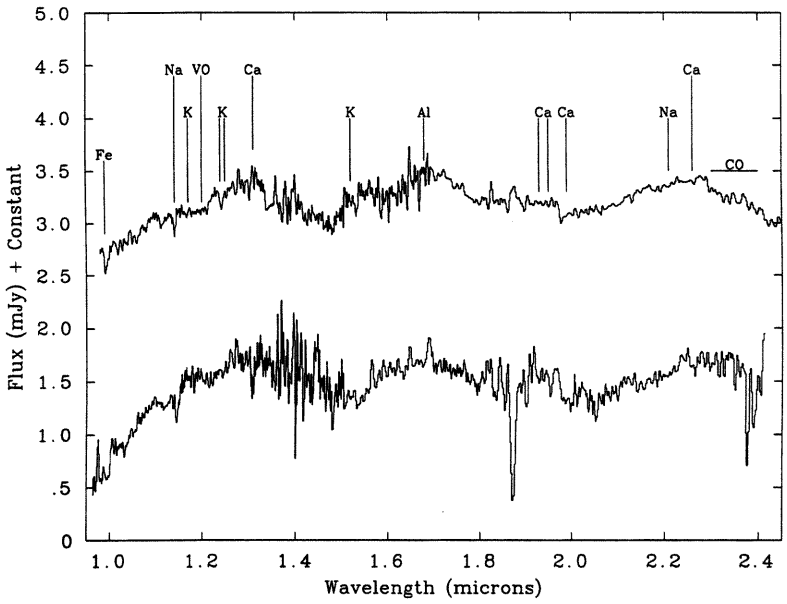

Figure 6.1: CGS4 1-2.5μm spectra of HHJ2 (lower) and HHJ3 (upper).

(most fundamental) method of measuring effective temperatures is the constant water vapour opacity method of Jones et. al. (1994 - JLJM94) as outlined in that section. The disadvantage of this method is of course that is requires a complete 1-2.5 micron spectrum. I will now consider the application of this method to the object for which we have a useable complete spectrum, HHJ3. While the method should also be applicable to HHJ2, in practice this spectrum was found to be too noisy to allow an accurate joining of the spectral fragments.

6.2.1 Spectroscopic Method

The first stage of this method is to fit a temperature T_{fit} through regions of constant opacity. To determine the wavelengths of the points of opacity it is necessary to have a rough idea of the fit temperature. The $I-K, T_{eff}$ relation of Bessell (1991 - B91) predicts that HHJ3 has $T_{eff} = 2805 \pm 40K$, the error quoted being that simply

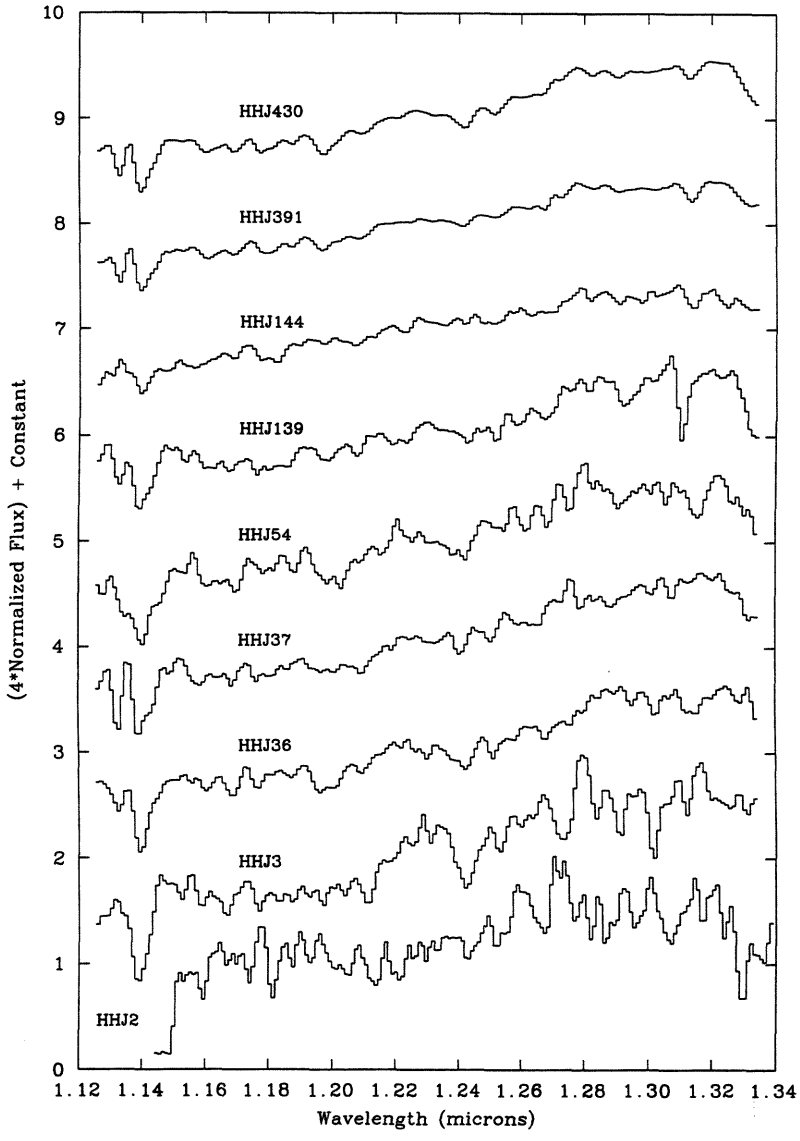

Figure 6.2: 1.2 micron spectral fragments.

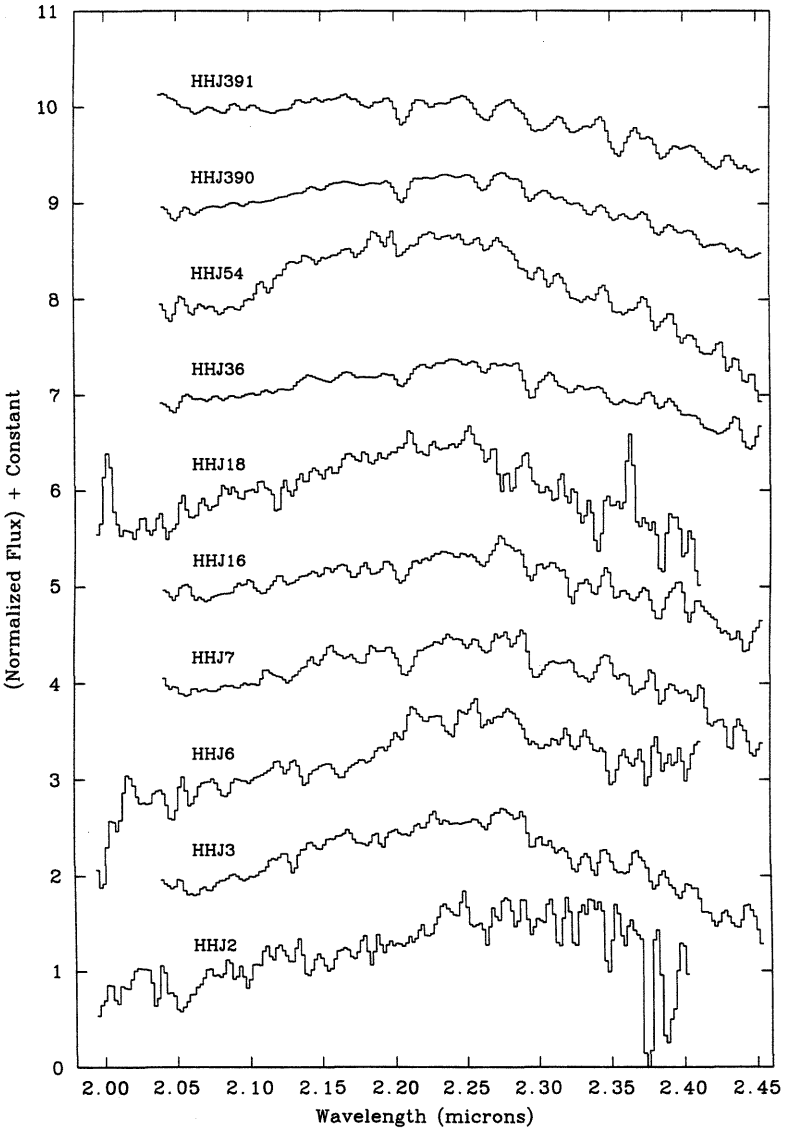

Figure 6.3: 2.2 micron spectral fragments.

due to the estimated error in the photometry. The Ludwig (1971) opacity curves (plotted in Figure 3.5 previously) are at 1500, 2000, 2500 and 3000K. An estimated temperature of 2750K (i.e. midway between the 2500 and 3000K water opacity curves) was therefore used to determine the wavelengths of the points of constant opacity. These were chosen at an opacity value of 0.026 cm^{-1} atm^{-1}, the 'high' opacity value used by JLJM94, which they found gave a better fit than a 'low' opacity value of 0.012 cm^{-1} atm^{-1}. The wavelengths used were therefore 1.366, 1.408, 1.508, 1.772, 2.130 and 2.384 μm.

The fit was carried out by a simple 'sliding curves' method. The spectrum to be fitted was converted to the log(flux) versus log λ plane. This was then fitted by overlaying and sliding a plot of log F_ν versus log λT where F_ν is the Plank function expressed as a function of λT (Allen 1973). When a fit was found then by reading off the difference between log λ and log λT it is possible to find the value of T, the fit temperature. An estimated error in the fit temperature may be derived by estimating the maximum and minimum values of the difference that give a reasonable fit.

Carrying out this procedure for HHJ3, a fit temperature was derived of $T_{fit} = 2754 \pm 50K$. The fit is shown in Figure 6.4. Note that for the purposes of fitting the spectrum was heavily smoothed in order to obtain a good value of the mean fluxes at the constant opacity points. Also the CO features around 2.3-2.4 μm must be interpolated over before carrying out the fit.

Using a combination of the infrared and optical spectroscopy and photometry, plus an assumed black body of temperature T_{fit} below 0.6 and above 2.4 microns a bolometric magnitude for this object was derived of $m_{bol} = 17.27$, corresponding to a received flux of $f_{bol} = 3.05 \times 10^{-12}$ ergs cm^{-2} sec^{-1}. This compares well with the value derived from the I magnitude using BC_I bolometric correction of Bessell (1991), which gives $m_{bol} = 17.19 \pm 0.05$. It is them simply a question of applying the mathematics outlined in Section 3.2 to derive values of R^2/d^2 and hence T_{eff}. The resulting temperature obtained is $T_{water} = 2803 \pm 60K$. Note that this is in excellent agreement with the figure derived from $I - K$ of $T_{I-K} = 2805 \pm 40K$ given above.

It therefore appears that the $T_{eff}, I-K$ relation of Bessell (1991) is well calibrated for the Pleiades and may be used with relative confidence in assigning effective

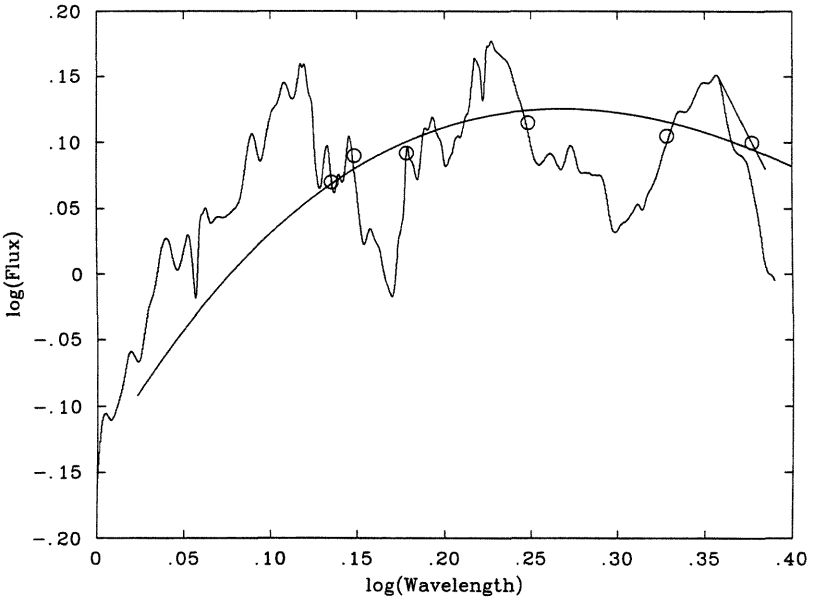

Figure 6.4: Black body constant opacity fit to HHJ3. The constant opacity points are circled. Note the interpolation over the CO bands at 2.3 microns

temperatures to Pleiades objects. However, this conclusion is based only on one object. It would be advantageous if some other method of measuring T_{eff} could be devised which did not rely on a complete $1-2.5\mu$m spectrum. The following section outlines an attempt at producing such a method.

6.2.2 Photometric ($RIJHK$) method

This method (the '$RIJHK$' method) is designed to be a "poor man's" version of the constant water opacity method used above, in that it only employs photometry to achieve its results. It is however more sophisticated than applying a single colour index or black body fitting through photometry.

The method is based upon the constant opacity method of JLJM94. However, the temperature T_{fit} is derived not from a spectrum but from the $H-K$ colour

of the object. Figure 6.5 plots $(H-K)_{CIT}$[1] versus T_{fit} as supplied by Hugh Jones (priv. com.) for the stars of JLJM94. The correlation is obvious and extremely good. Therefore it appears that knowing $H-K$ one may predict T_{fit}. Examining the example fit shown by JLJM94 (their Fig. 3) or Figure 6.4 above, shows why this might be the case - the fit is basically between two points in the H band and two in K. Therefore it is not unreasonable to expect $H-K$ to be a good estimator of T_{fit}.

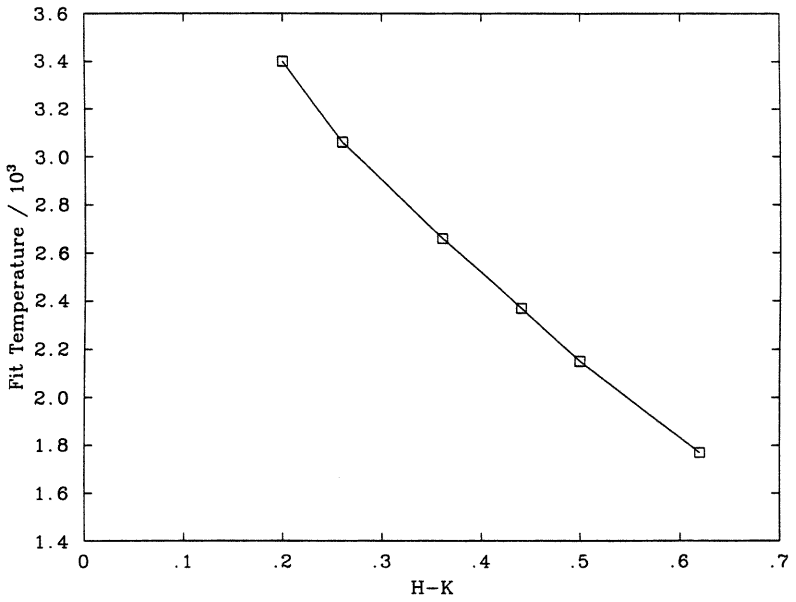

Figure 6.5: T_{fit} versus $H-K$ for the objects of Jones et. al. (1994).

It is now simply a question of following the method of JLJM94. As shown in Section 3.2 using T_{fit} allows the calculation of $(R/d)^2$ from the equation

$$f_\lambda = \frac{R^2}{d^2} F_\lambda(T_{fit}) \tag{6.1}$$

where f_λ is the measured flux at a point of constant opacity, R is the radius, d the distance of the object and $F_\lambda(T)$ is the Plank function. In this case one does not in

[1]Note Leggett (1992) provides transforms between the UKIRT system used elsewhere in this thesis and the CIT system used here.

general have f_λ so instead the K band flux F_K must be employed. From Bessel & Brett (1988) F_K has an equivalent wavelength of 2.19 microns, whereas Figure 3.5 shows that the nearest constant opacity point to this is around 2.12 microns (the exact location being a function of temperature). Using F_K will therefore overestimate R^2/d^2. To correct this I have determined an empirical correction to the value of R^2/d^2 using the data of JLJM94. I find that

$$\frac{(R/d)^2_{true}}{(R/d)^2_{calc}} = 1.7 \log_{10} T_{fit} - 5.052. \tag{6.2}$$

Having determined R^2/d^2, T_{eff} can then be calculated using the bolometric flux, F_{bol}, since, again as shown in Section 3.2,

$$\sigma T^4_{eff} = \frac{d^2}{R^2} F_{bol}. \tag{6.3}$$

In this case F_{bol} is calculated by combining the $RIJHK$ photometry with a black body of temperature T_{fit} shortward of R (0.64 microns) and longward of K (2.19 microns), ie.

$$F_{bol} = \int_0^{0.64} F_\lambda(T_{fit}) d\lambda + RIJHK_{contribution} + \int_{2.19}^{\infty} F_\lambda(T_{fit}) d\lambda. \tag{6.4}$$

It is valid to use a black body to model the long and short wavelength flux regions since a star of 3000K emits over 70% of its flux between R and K. Thus the error introduced by assuming a simple black body outside of this wavelength range will be relatively small. A more important source of error in the calculated F_{bol} will be the water vapour absorption bands between the J, H and K band peaks in the spectrum. Their presence will cause F_{bol} to be overestimated. The effect will become stronger as the temperature decreases, causing the water vapour bands to deepen. In order to correct for this another empirical correction from the data of JLJM94 has been derived. This takes the form

$$\frac{F_{bol_{true}}}{F_{bol_{calc}}} = 1.9 \times 10^{-4} T_{fit} + 0.288. \tag{6.5}$$

Once T_{eff} has been determined, it can substituted for T_{fit} in Equation 6.5. This leads to an improved estimate of F_{bol} and hence of T_{eff}. It is then possible to iterate the F_{bol} determination again, and the process may be repeated until the solution for T_{eff} reaches its limiting value.

This method has been implemented as a computer code, inputing $RIJHK$ magnitudes and iterating until T_{eff} has reached a stable value. This normally only requires two or three iterations. Figure 6.6 plots the T_{eff} values from the $RIJHK$ method against those determined by JLJM94 for all of the stars for which they quote $RIJHK$ photometry. It can be seen that the $RIJHK$ temperatures match those measured by JLJM extremely well, the maximum deviation being $\sim$ 60K.

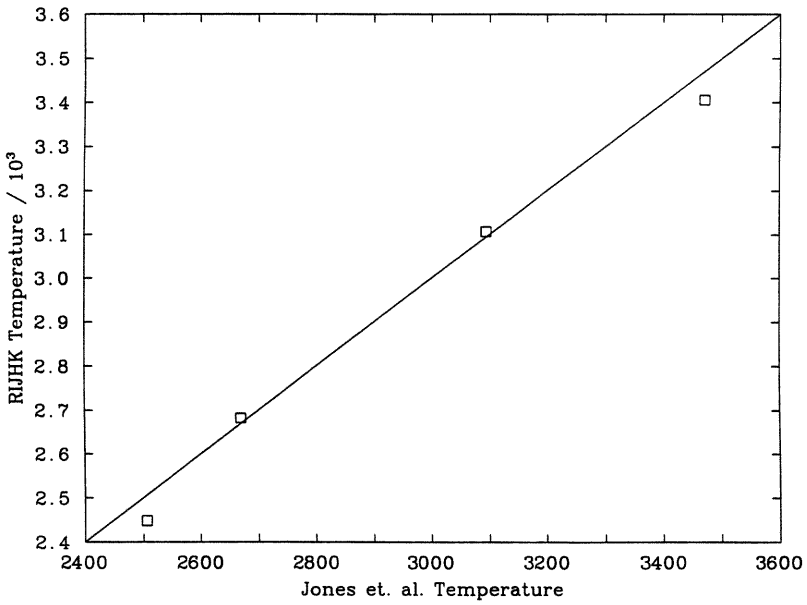

Figure 6.6: T_{water} versus T_{RIJHK} for the objects of Jones et. al. (1994).

It therefore appears that the $RIJHK$ method should be a reasonable indicator of T_{eff} for low mass objects. It should be noted however that the low mass object sample of JLJM94 is based on Old Disk stars whereas the low mass Pleiads belong to a higher metallicity, lower gravity (as they are still contracting) Young Disk population. Care will therefore be necessary when applying the $RIJHK$ method to the Pleiades. In addition the method, with its heavily reliance on bolometric fluxes, will only be reliable when applied to single (i.e. not binary) objects.

How good a temperature indicator is T_{RIJHK} as compared with $I-K$? To answer this question I use the spectral sequence derived in Chapter 5, choosing only single objects and assuming that the spectral sequence derived there is a true temperature sequence. The $RIJHK$ temperatures derived for all of the single objects are therefore listed in Table 6.5. Figure 6.7 plots (a) T_{I-K}, (b) T_{RIJHK}, (c) $m_{bol(I-K)}$ and (d) $m_{bol(RIJHK)}$ versus optical spectral subclass, where the suffixes indicate the method of deriving the temperatures and luminosities used. A further limitation of this approach is that the optical subclasses assigned in Chapter 5 are only derived to within 0.5 subclasses.

Recognising these limitations, it is still apparent from a comparison of the spread in Fig. 6.7 (a) and (b) that $I-K$ is a better indicator of temperature than the $RIJHK$ method. This is unfortunate as it means that the new method can not be used to check the effectiveness of $I-K$. That the $RIJHK$ method should be a good temperature indicator was shown earlier for the objects of JLJM94. The problem in this case appears to be that relatively large (~ 0.1 mag. in a value of ~ 0.3) errors in the Pleiades $H-K$ photometry give a large ($\sim 400K$) error in T_{fit}. In contrast the relatively small ~ 0.1 mag. error in a value of ~ 3 for the $I-K$ photometry corresponds to an error of only $\sim 40K$ in the derived T_{eff} (assuming of course that the photometric error is the only source of error in T_{eff} and no systematic errors are present).

The bolometric magnitudes derived by the two methods (taking Bessell 1991 (B91) as representative of the empirical scales discussed in Section 3.2) both seem to act as very good temperature indicators (obviously this will only be true in a cluster, where the objects are coeval). Figure 6.8 compares the bolometric magnitudes derived from the RIJHK method and B91 (using only I and $I-K$). Note the good agreement between the two methods. In general the $RIJHK$ bolometric magnitudes appear to be ~ 0.1 mag. fainter than those from B91. This could reflect problems with either (or both!) method(s).

In conclusion, with higher precision photometry of the Pleiades, or applied to nearby, brighter objects, there should still be some value in the $RIJHK$ method as a determinant of T_{eff}. On the other hand even with the present photometry the

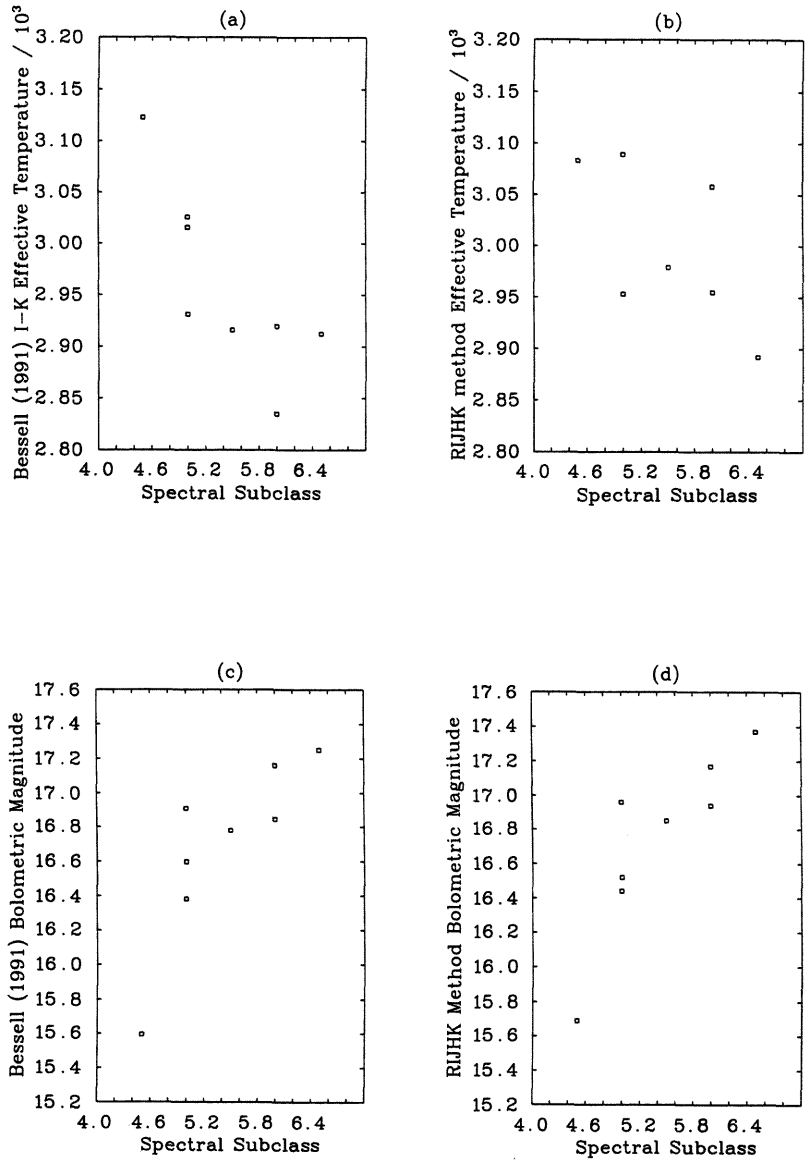

Figure 6.7: (a) T_{I-K}, (b) T_{RIJHK}, (c) $m_{bol(I-K)}$ and (d) $m_{bol(RIJHK)}$ versus optical spectral subclass.

Object	T_{I-K}	T_{RIJHK}	$m_{bol(I-K)}$	$m_{bol(RIJHK)}$	Spectral Class
hhj2	2912	2892	17.25	17.37	M6.5
hhj3	2835	3058	17.16	17.17	M6.0
hhj7	2919	2955	16.85	16.94	M6.0
hhj8	2923	2999	16.91	16.99	-
hhj13	2931	2924	16.74	16.83	-
hhj15	2951	3094	16.74	16.76	-
hhj17	2947	2801	16.70	16.89	-
hhj20	2977	2950	16.66	16.77	-
hhj21	3020	2960	16.72	16.85	-
hhj22	2931	2844	16.54	16.70	-
hhj25	3005	3148	16.59	16.63	-
hhj27	2991	3045	16.53	16.61	-
hhj37	3025	2953	16.38	16.52	-
hhj92	3097	3023	15.97	16.09	-
hhj139	3122	3083	15.59	15.69	M4.5
hhj153	3175	3115	15.50	15.58	-
hhj9	2931	3089	16.91	16.96	M5.0
hhj12	2916	2979	16.78	16.85	M5.5
hhj23	3015	3505	16.60	16.44	M5.0

Table 6.5: $RIJHK$ and $I-K$ Temperatures of Single Objects

bolometric luminosities derived by the $RIJHK$ method appear to be as good as those from any other.

6.2.3 T_{eff} from Spectral Features

Another method of measuring T_{eff}'s using the infrared spectra is the use of spectral features as temperature indicators. JLJM94 provide a comprehensive list of spectral features that may be used as temperature indicators. They also provide measurements of these features in their spectral sequence, allowing temperatures for other objects to be determined. Again the usual caveats about differing metallicities and gravities between the JLJM94 and Pleiades objcets apply. This means that the resulting temperatues for the Pleiades objects will only be relative.

Various spectral features in the 1.2 and 2.2 micron spectral fragments were therefore measured using the FIGARO routine ABLINE (Robertson 1986). Equivalent Widths (EWs) are listed in tables 6.6 and 6.7.

The mean resulting temperatures (T_{lines}) from the 1.2 micron EWs are listed in table 6.2.3. The error quoted is the standard deviation of the determinations of the

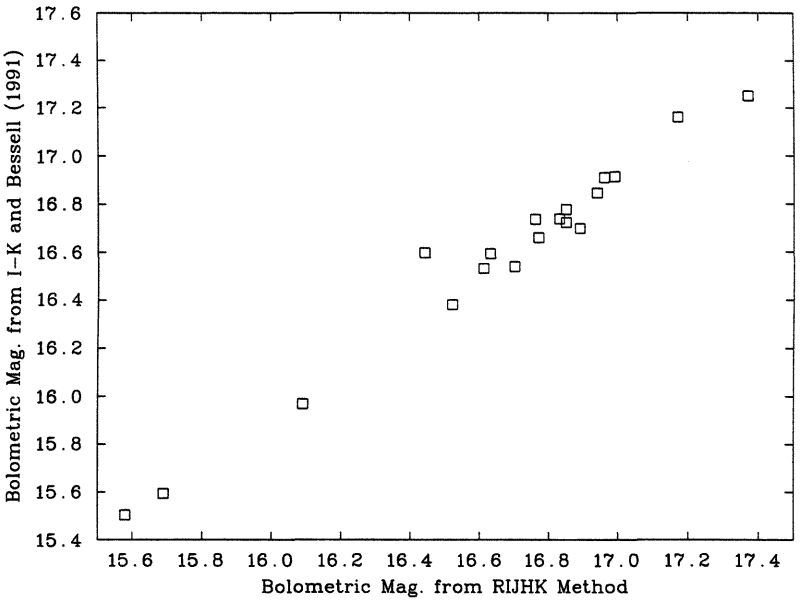

Figure 6.8: Comparison of Bolometric Magnitudes from RIJHK and Bessell (1991) method for Pleiades objects.

ID	NaI 1.14	KI 1.17	KI1.18	VO 1.20	KI 1.24	KI 1.25	CaI1.31
HHJ3	1.450	0.345	0.142	0.083	1.027	0.228	0.216
HHJ36	1.028	0.223	0.136	0.651	0.555	0.207	0.410
HHJ37	0.925	0.101	0.236	—	0.218	0.174	0.117
HHJ54	1.293	0.179	0.225	1.067	0.469	0.124	0.417
HHJ139	0.956	0.094	0.340	0.153	0.110	0.107	0.495
HHJ144	0.297	0.063	0.320	0.025	0.024	0.154	0.239
HHJ391	0.447	0.113	0.162	0.274	0.120	0.062	0.205
HHJ430	0.630	0.140	0.229	0.422	0.222	0.097	0.161

Table 6.6: Equivalent Widths in nm for 1.2 micron spectra.

ID	NaI 2.21	CaI 2.26
HHJ3	0.174	0.263
HHJ7	1.040	0.418
HHJ16	0.684	0.408
HHJ36	0.398	0.193
HHJ54	0.748	0.221
HHJ390	0.673	0.522
HHJ391	0.914	1.055

Table 6.7: Equivalent Widths in nm for 2.2 micron spectra.

ID	T_{lines}
HHJ3	$2710 \pm 300K$
HHJ36	$2825 \pm 200K$
HHJ37	$3000 \pm 80K$
HHJ54	$2810 \pm 280K$
HHJ139	$3025 \pm 250K$
HHJ144	$3300 \pm 310K$
HHJ391	$3175 \pm 240K$
HHJ430	$3040 \pm 280K$

Table 6.8: T_{eff} from infrared line equivalent widths.

various lines. Note JLJM94 do not find the CaI 2.26 μm feature in any of their spectra and so do not calibrate it. Therefore T_{eff}'s for objects with only 2 micron spectra have not been quoted since they would be based only on the measurement of one line.

Figure 6.9 plots these derived temperatures versus optical spectral subclass from chapter 5. From this figure it is apparent that the temperatures derived from line EWs appear to be quite reasonable temperature indicators overall. The large errors on each determination however show that this method will not be that reliable for any particular individual Pleiad. The large errors are caused by the generally poor poor signal to noise ratio of spectra, which makes accurate determination of EW difficult. With higher signal to noise (i.e. brighter targets) however this method could be very useful, since it relies on only one spectral fragment (1.2 microns) to measure T_{eff}.

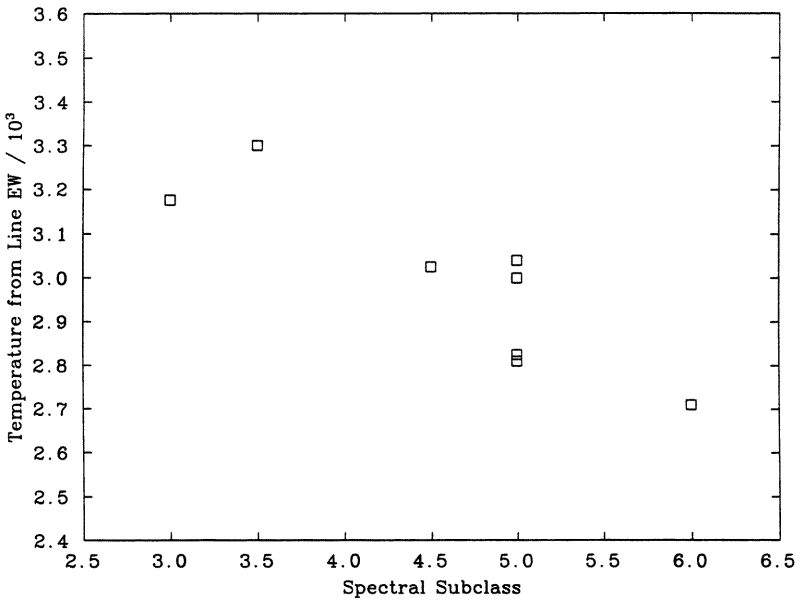

Figure 6.9: T_{lines} versus spectral subclass for Pleiades objects with 1.2 μm spectra.

6.3 Evidence for Binarity

In Section 4.3.4 I showed how a photometric model of the I band luminosity and $I - K$ colour of artificial binary stars allowed the identification of a binary star sequence (BSS) lying 0.75 mag. above the single star sequence (SSS). In section 5.4 I showed the effect of an unresolved companion on the optical FOS spectra would be small, shifting the spectral type by half a subclass at most. In the infrared however, one might expect things to be different, as a faint, very red companion would emit most of its flux in this region.

To model the effect of an unresolved companion on the CGS4 spectra I will consider two approaches. The first approach is a simple black body modelling approach. After that I will consider the results of coadding actual spectra. The approaches are complimentary, in that they each give some information as to the expected effect of binarity on the spectra.

6.3.1 Blackbody Model

In both cases I shall model a $0.09 + 0.04M_{\odot}$ binary pair. This will give detectable effects in the spectra at all wavelengths. Note that using an equal mass binary pair would give a spectrum identical to that of either of the components but simply twice as bright at all wavelengths. Since CGS4 is not designed to be a true spectrophotometric instrument, such an object would be spectroscopically indistinguishable from a single star at low resolution. With higher resolutions, as could be achieved with the Echelle mode of CGS4, then doubled lines due should be evident. However CGS4 lacks the sensitivity to make such measurements of the faint Pleiads objects of interest in this project.

For the Pleiades age Stringfellow (1991) shows that the $0.09 + 0.04M_{\odot}$ pair will have approximate T_{eff}'s of 2900 and $2500K$ respectively. The relative luminosity difference between the objects will be a factor of 4. Figure 6.10 therefore plots blackbody curves from Allen (1973) for those temperatures and relative luminosities. The 2900K object is shown as a dotted line and the 2500K object as a dashed line. The composite spectrum is shown by a solid line. Note that the effect of the cooler companion is apparent at all infrared wavelengths, but is greatest after 1.8 microns as the flux declines more slowly on the Wien tail of the blackbody curves than when rising towards the peak. At this wavelength the spectral slopes of the 2900K object and the artificial binary become virtually identical and remain so all the way out to 3.5 microns and beyond. From this it appears that there would be no point in looking for the effect of the companion anywhere beyond 1.8 microns.

Below 1.8 microns the situation is better, with significantly different slopes apparent between the binary and single objects. In particular in the region 1.2 - 1.3 microns an appreciable slope difference is apparent. From Figures 3.5 and 6.1 this region is fairly uncontaminated by water vapour and other band forming species. The continuum slope in this region should therefore be a good test for binarity involving a very low mass companion.

Continuum slopes were therefore measured by fitting a straight line to the continuum between 1.15 and 1.30 μm. A measure of the slope of that line was then

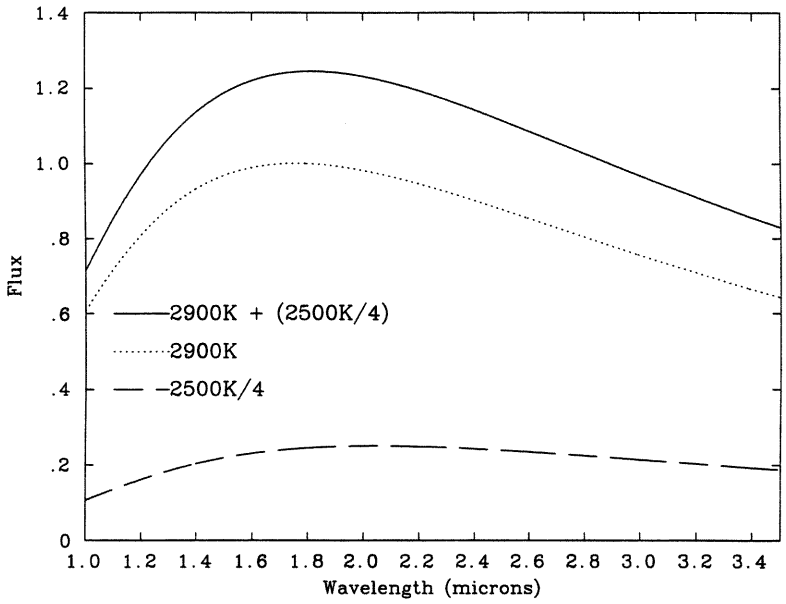

Figure 6.10: Artificial infrared binary spectrum calculated from blackbody curves.

defined:

$$S_{1.22} = \frac{F_{1.3} - F_{1.15}}{F_{1.3} + F_{1.15}}. \tag{6.6}$$

The denominator of the fraction ensures that all of the spectra are effectively normalized during the measurement of the slope. Table 6.9 list the measured values of $S_{1.22}$ for all of the 1.2 micron spectral fragments. Their optical spectral types (since this slope will also be a function of T_{eff}) and binary status from Chapter 4 is also given.

Three objects immediately stand out. The first is HHJ2 which appears to have an anomalously low value of $S_{2.1}$. Whether this is simply an artifact of the very poor signal-to-noise ratio of the HHJ2 observations is not easy to determine. HHJ2 was shown in Chapter 5 to be the coolest of the Pleiads whereas the slope measured here would make it the hottest. Therefore either something *very* strange is going on in this object, or, more likely, the poor quality of the spectrum makes even measurements of slopes unreliable.

ID	$S_{1.22}$	Spectral Class	Photometric Binary?
HHJ2	0.05	M6.5	no
HHJ3	0.15	M6	no
HHJ36	0.11	M5	yes
HHJ37	0.12	M5	no
HHJ54	0.13	M5	yes
HHJ139	0.12	M4.5	no
HHJ144	0.10	M3.5	no (non-member)
HHJ391	0.09	M3	???
HHJ430	0.11	M5	???

Table 6.9: 1.22 micron spectral slopes.

The second object is HHJ3. This has the steepest slope, although whether this is simply due to the coolness of this object or a companion is difficult to say without a similar single object for comparison. It is unfortunate therefore that HHJ2 looks so peculiar.

The final object of note is HHJ54. This object has a steeper slope than any of the other objects of its spectral class, and is a good photometric binary candidate, lying very close to the binary star sequence of Figure 4.7. That a companion is suggested by an (all be it modestly) increased slope is therefore encouraging.

6.3.2 Real Spectra Model

The black body model for the binary flux distribution outlined in the previous section is obviously only an approximation. A better approach is to coadd spectra of known single objects to create an artificial binary spectrum. This was carried out between 1.5 and 2.5μm using three objects from the spectral sequence of JLJM94 which were supplied by Hugh Jones (priv. com.). Note not all of these spectra extend below 1.5μm, so this method could not be applied to derive the change in $S_{1.22}$ of Section 6.3.1. Normalized spectra of GL699 ($T_{eff} = 3100K$) and GL406($T_{eff} = 2670K$) were averaged to produce a $\sim 2900K$ spectrum. To this was added VB10 ($T_{eff} = 2506K$) normalized to 0.25$\times$ the peak flux of the $2900K$ spectrum. The results of this procedure are shown in Figure 6.11. The artificial binary is shown as a dotted line and the $2900K$ spectrum a solid line.

Note that the effect of the water vapour bands is to make spectral differences

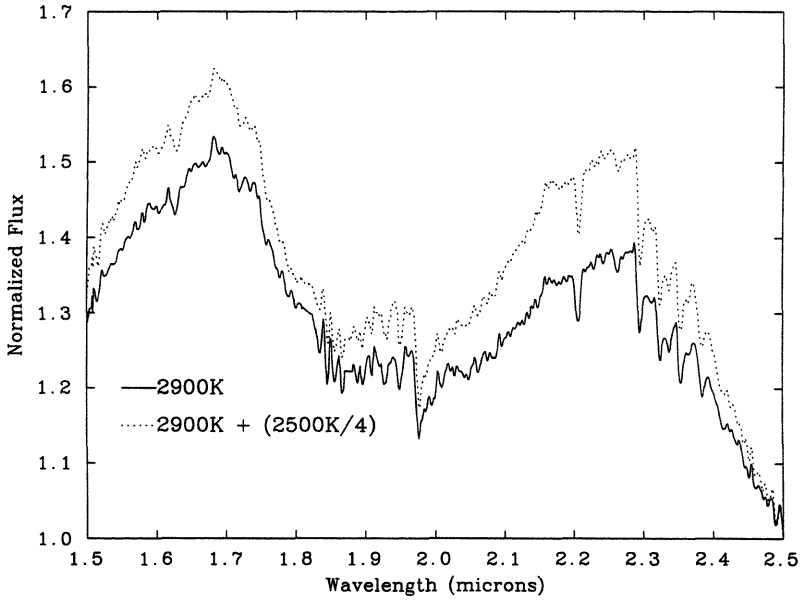

Figure 6.11: Artificial binary spectrum constructed from the data of Jones et. al. (1994).

obvious at 2-2.2 microns, where the simple black body model used above predicted no differences. The strength of the CO bands at 2.3 microns is also affected. To quantify these effects I use two more spectral indices. The first is a measure of the 2.1 micron slope analogous to that used at 1.22 microns and defined as

$$S_{2.1} = \frac{F_{2.3} - F_{2.1}}{F_{2.3} + F_{2.1}}. \tag{6.7}$$

and the second the CO index defined by JLJM94;

$$CO = \frac{< F_{2.22-2.28} >}{< F_{2.30-2.36} >}, \tag{6.8}$$

where the symbol $< F_{n-m} >$ indicates the mean flux over the wavelength interval $\lambda = n$ to $\lambda = m$.

The measured values of these indices, along with spectral type and photometric binary status are listed in Table 6.10. The table also lists measured values of these indices for the $2900K$ object and the artificial binary.

ID	$S_{2.1}$	CO	Spectral Class	Photometric Binary?
HHJ2	0.07	1.01	M6.5	no
HHJ3	0.05	1.11	M6	no
HHJ6	0.04	1.09	M6.5	yes
HHJ7	0.05	1.09	M6	no
HHJ16	0.05	1.09	M5.5	yes
HHJ18	0.05	1.19	???	???
HHJ36	0.04	1.08	M5	yes
HHJ54	0.16	1.17	M5	yes
HHJ390	0.04	1.09	M4.5	???
HHJ391	0.02	1.10	M3	???
2900K Obj.	0.06	1.08	N/A	N/A
Art. Bin.	0.09	1.11	N/A	N/A

Table 6.10: 2.1 micron slope and CO index.

The results from this exercise are even more interesting than the previous one. HHJ54 stands out as an excellent candidate for an object with a very low mass companion, with $S_{2.1} \sim 3\times$ steeper and $CO \sim 2\times$ deeper than objects of the same optical spectral type. Note that since this object lies on the BS, we can assign a minimum mass to the companion of $\sim 0.03M_{\odot}$ and the results of this exercise show it appears to be redder than the $0.04M_{\odot}$ object (which VB10 would be *if* it had the Pleiades age) added to the artificial spectrum. There is therefore strong evidence from the infrared spectra at both 1.2 and 2.2 microns for an unresolved companion of around $\sim 0.035M_{\odot}$. If this could be confirmed by high-resolution imaging (either by shift-and-add, adaptive optics or use of the Hubble Space Telescope) or by high resolution optical spectroscopy the companion would be a certain brown dwarf, with the added advantage of the possibility of measuring a dynamical mass.

By contrast HHJ6,16 and 36, if they are binary systems, seem to have components of roughly equal mass, since no effects can be seen in the spectra.

The anomalous optical spectrum of HHJ18 was noted in Sections 5.2 and 5.4 and its infrared spectrum can also be seen to be peculiar, with very strong CO but only average water vapour. This is the signature of a giant. However the optical spectrum can not be explained as a giant, and the true nature of this object remains undetermined.

6.4 Conclusions

In this chapter I have used spectra in the range 1-2.5μm to investigate both the determination of effective temperature and evidence of unresolved binary companions amongst the Pleiades sample.

For the determination of effective temperature three methods have been employed:

1. The constant water vapour opacity method of JLHM94 for one object (HHJ3). This derives a temperature which closely agrees to that derived from $I-K$ using the temperature scale of B91.

2. A new method, the '$RIJHK$' method. This is a "poor-man's" version of the constant water vapour opacity method based on photometry and empirically derived corrections. While the method may have some useful applications, the large photometric errors in the $H-K$ colours of the Pleiades sample meant that the method was found to be a poor indicator of T_{eff} in this case.

3. Temperatures derived from line equivalent widths calibrated by the data of JLJM94. This derives reasonable temperatures but the errors on any one temperature can be large ($\sim 200K$).

The 'best' method is undoutably that of JLJM94. However $I-K$ also remains a good indicator for single objects, hence diagrams such as those in Chapters 4 and 5 should remain valid in identifying low mass stars and brown dwarf candidates.

In searching for evidence of unseen binary companions both 1.2 and 2.2 micron spectra yield useful information in the shape of slopes and the 2.3 micron CO bands. In the Pleiades sample observed in this chapter one object (HHJ54) shows strong evidence for an unseen binary companion of mass $\sim 0.035M_{\odot}$.

Chapter 7

Conclusions

In Chapter 1 I set out the primary aim of this thesis - to determine the nature of the lowest mass members of the Pleiades star cluster. In this chapter I review the results of Chapters 4, 5 and 6 and discuss how these results point to the lowest mass members being brown dwarfs. I also discuss the arguments put forward by other workers that these objects are *not* brown dwarfs. Finally I give suggestions for future work in the field.

7.1 Arguments for Pleiades Brown Dwarfs

7.1.1 Chapter 4 - Infrared Photometry

Chapter 4 presented IRCAM infrared JHK photometry of a total of 62 objects. 48 of the objects were proper motion members according to HHJ91 and the remaining were 'I-only' objects that appear only on I band plates and are therefore very red. In addition CCD observations ar R and I for 15 objects were presented. These showed that the COSMOS magnitudes from the survey of HHJ91 were well callibrated.

The $I, I-K$ diagram was shown to be a good discriminant of cluster membership. Using this diagram it was possible to identify a small number of objects from the HHJ91 survey that appeared to be cluster non members. The number of these objects found agreed with that predicted by the statistical membership probabilities for the proper motion survey given by Hambly (1991). For the I-only objects only

2 out of 14 appeared to be cluster members, however without proper motions their membership status is still very uncertain.

This chapter attempted a comparison of the observed $I, I-K$ diagram with theoretical isochrones from Stringfellow (1991) and Burrows et. al. (1993). These were converted to the obsevational plane using the relations provided by Bessell (1991). The combination of Stringfellow (1991) and Bessell (1991) was shown in Chapter 3 to be the *most* conservative combination of the current models and temperature scales. In addition this combination matches the old disk stars well. Even using this conservative combination two good, single brown dwarf candidates with masses of $\sim 0.075 M_{\odot}$ are indicated - HHJ2 and HHJ3. Using the model of Burrows et. al. (1993) increases the number of single brown dwarf candidates to 11.

In this chapter I also showed how the $I, I-K$ diagram may be used as an indicator of binarity for low mass objects, with binary objects (of *all* mass combinations involving an object with $M > 0.03 M_{\odot}$) lying on a binary star sequence 0.75 mag. above the single stars. In addition I showed how objects lying below and to the right of the $0.08 + 0.08 M_{\odot}$ binary point will all contain at least one brown dwarf component. The exact position of this point is again of course dependant on the theoretical model used. Using Stringfellow (1991) gives seven brown dwarf containg binaries, Burrows et. al. (1993) increases this to 15.

7.1.2 Chapter 5 - Optical Spectroscopy

Chapter 5 presented FOS optical spectra of a sample of 31 of the HHJ91 members. All of the spectra of members determined photometrically to be cluster members show Hα emission, whereas the one photometric non-member observed does not. This is further evidence that the Pleiades sample selected by the combination of proper motions and photometry really is uncontaminated by background objects. The spectra are all typical of early to mid M dwarfs, and a spectral sequence was contructed using the least squares minimization technique devised by Kirkpatrick et al. (1991). The inclusion of several spectral standards in the observations allowed spectral types to be assigned to the Pleiades objects. These range from M0 for the hottest to M6.5 for the coolest.

The spectal sequence allowed the investigation of various temperature indicators, both photometric and spectroscopic. Of the photometric indicators, both $R-I$ and $I-K$ were found to be reasonable indicators of T_{eff}. The $I-K$ indicator is strongly affected by binarity, but for known single objects is probably the best indicator. Of the spectroscopic indicators, the best were found to be those based on TiO and VO bands rather than atomic lines.

In addition the spectral sequence allowed an investigation of the surface gravity of the low mass Pleiades objects to be made. Measurement of the NaI 8183/8195Å doublet indicated that the Pleiades objects of spectral type M5.5 have lower surface gravities than field objects of equivalent temperature. Pleiades objects of spectral type M3.5 and below appeared to have similar surface gravities as the field. The surface gravity properties of both the M3.5 and M5.5 objects were shown to be consistent with the masses derived from theory for these objects, assuming an age of 70 Myr. This is further evidence that the masses derived for the very low mass objects in Chapter 4 are correct (assuming the theory is valid of course!)

In addition I note here that the high resolution optical spectra presented by Marcy et. al. (1994), Magazzu et. al. (1994) and Stauffer et. al. (1994b) of several of the HHJ91 objects all show rotational broadening indicating rapid rotation (a signature of youth) and radial velocities consistent with cluster membership. This is further evidence that the HHJ91 sample is uncontaminated by background objects.

The effect of multiplicity on the spectra was discussed using an artifical binary created by coadding two single star spectra. The effect of binarity on the photometric temperature indicators has already been discussed. For the spectral sequence the effect of unresolved binarity was found to be a possible increase of up to half a subclass in the spectral type derived. Similar increases in several of the spectroscopic indictors were also found. The overall effect of unresolved binarity on the optical spectra was small, and attempts to deconvolve the spectra, or simply search for evidence of binarity were unsuccessful. However the infrared spectra presented in Chapter 6 give an opportunity for at least the second of these.

Chapter 5 also considered the nature of the activity dynamo in low mass stars. While not directly relevant to the primary aim of the thesis, this work shows the

value of the homogenous HHJ91 sample as a powerful tool in investating the variation of stellar properties with mass. In this case the combination of Hα measurements from the FOS spectra and ROSAT X-ray fluxes allowed chromospheric and coronal activity to be traced down to below $0.3M_{\odot}$ (the mass below which a star becomes fully convective). A turnover in both types of activity was seen, providing both the first clear evidence for a change in the nature of the dynamo at this mass and evidence that the dynamoes driving both types of activity are closely linked.

7.1.3 Chapter 6 - Infrared Spectroscopy

This chapter considered results obtained using the CGS4 cooled grating spectrometer. The results consisted of a small sample of 1.2 and 2.2 μm spectral fragments of HHJ91 objects plus complete 1-2.5 μm spectra of HHJ2 and HHJ3. Unfortunately due to poor weather the signal to noise ratio of the HHJ2 spectrum was very poor. However, HHJ3 had sufficiently good signal to noise to apply the constant water vapour opacity method (Jones et al. 1994) for determining T_{eff}. The temperature derived by this method agrees very closely with that derived from $I-K$ for this object using Bessell (1991). This is further evidence that the choice of Bessell (1991) as a temperature scale in Chapter 4 was a good one and that the brown dwarf candiates identified there remain good.

A new method of measuring temperatures (the '$RIJHK$ method') was introduced. This was an attempt to produce a photometric equivalent of the method of Jones et. al. (1994). While the method appears to work for the field stars observed by Jones et. al. (1994), the relatively large errors in the $H-K$ colours of the Pleiades sample meant it could not be applied there.

The 1.2μm spectral fragments contained many spectral lines and using these another determination of T_{eff} was carried out. This found temperatures broadly in agreement with those derived from $I-K$ for the single objects, although the errors in the line temperatures are large due to the relatively poor signal-to-noise of the spectra.

Chapter 6 also looked for evidence of binarity in the infrared spectra. Two approaches of modelling the effect of binarity were considered. Using black bodies

to model the effects at 1.2μm (where water vapour opacity is low) showed that the 1.22μm slope should be a good indicator of binarity. One object was shown to have a slope possibly indicative of binarity, HHJ54. This object lies on the binary star sequence of Chapter 4. The second approach to modelling the effects of binarity was to coadd real single star spectra. This showed that due to the varying water vapour band strenghs and CO absorption binarity should also be detectable via. the 2.2μm slopes and 2.3μm CO index of the spectra. Strong evidence of binarity was found for HHJ54, and an argument given which suggests the mass of the binary companion is around $\sim 0.035 M_{\odot}$.

This evidence that at least one of the objects on the binary sequence has strong spectral support for its binary status reinforces the status of the other objects on that sequence as unresolved binaries, and the interpretation of objects below the $0.08 + 0.08 M_{\odot}$ point as systems containing brown dwarfs.

7.2 Arguments against Pleiades Brown Dwarfs

There are two principle arguments againgst the identifcation of the faintest objects in the Pleiades sample of HHJ91 as brown dwarfs. The following sections discuss each of these in turn.

7.2.1 The Lithium Test

None of the optical spectra of our brown dwarf candidates show radical differences in appearance from the higher (stellar) mass objects. This is not surprising given their relatively low resolution. Higher resolution spectra would allow a search to be made for the lithium indicator of brown dwarf status proposed by Rebolo, Martin & Magazzu (1992).

The Lithium Test is based on the fact that the element burns at temperatures of around $2.5 \times 10^6 K$, easily attained even in the interiors of very low mass M stars. The theoretical models of D'Antona & Mazzitelli (1985,1994), Nelson et. al. (1986,1993) and Burrows et. al. (1993) all show that for masses under $\sim 0.06 M_{\odot}$ the maximum central temperature is always below the lithium burning temperature. For

masses between 0.08 and $0.06M_{\odot}$ the models predict lithium will be burnt, but on a timescale slightly greater than the Pleiades age (70 Myr). Therefore the presence of the Li resonance doublet at 6708Å would provide firm evidence of brown dwarf status for any candidate.

Searches for this line have been carried out for HHJ3 and HHJ14 by Marcy, Basri & Graham (1994) and for HHJ10 by Magazzu, Rebolo & Martin (1994). In all cases the lithium line was not detected, apparantly indicating significant lithium depletion has taken place and that these objects are not brown dwarfs.

However, since it has never been applied succesfuly to any brown dwarf candidate the validity of the lithium test is unknown. I point out that in general the lithium test is based on comparison of lithium equivalent width with that of a T-Tauri star (UX Tau C, Li EW $\sim$ 600mÅ). Walter et. al. (1988) show that Li equivalent widths (EW) for T-Tauri stars vary considerably from object to object, down to $\sim$ 100mÅ for many 'naked' T-Tauri stars, which they regard as the true precursors of lower mass objects. The Li upper limit for the Pleiades objects observed by Marcy et. al. (1994) and Magazzu et. al. (1994) was $\sim$ 200mÅ. Therefore even if Li was present at its initial abundance, it still may not have been observed. In addition T-Tauri stars are much younger than the Pleiades objects and so have considerably lower surface gravities. This may affect the abundance of atomic lithium, since higher gravities favour the formation of molecules involving Li. Further work is necessary in modelling this chemistry in stellar atmospheres before the lithium test can be considered truly reliable. Further all of the brown dwarf candidates proposed here are in the range $0.08M_{\odot} > M > 0.06M_{\odot}$. These should eventually burn Li and it may be that convection takes Li to the core faster than existing models predict, possibly as a result of the rapid rotation which Marcy et al. note in their spectra. Alternatively the core may heat up quicker than expected, causing Li to be depleted earlier. In any case there is a conflict between the observations and the theories of brown dwarf structure and the lithium test here. The structure theory predicts the faintest HHJ objects are brown dwarfs whereas the lithium theory does not. Therefore one (or both!) of the theories must be in error.

In conclusion much further work is necessary both theoretically and observationally in this field before the brown dwarf candidates identified here can be dismissed on the evidence of the lithium test.

7.2.2 'Differential Analysis' of Stauffer et. al. (1994b)

In view of the problems already discussed in converting theoretical models from the theoretical to observational planes, Stauffer et. al. (1994b) present an alternative method of determining the location of the minimum mass for hydrogen burning on the $I, I-K$ diagram. This method does not use a temperature scale at all, but compares the properties of an assumed $0.1M_{\odot}$ main sequence object (GL406) with a Pleiades age brown dwarf. Using the models of Burrows et al. (1993) they show that such objects should have the same T_{eff} (and hence presumably the same $I-K$) and differ in bolometric luminosity by a factor two (the Pleiades object being the brighter). This locates the 70Myr $0.08M_{\odot}$ point at $I = 17.4, I-K = 3.31$. All of the HHJ91 objects lie above this point (HHJ3 is just above it!), and therefore by this analysis are not brown dwarfs.

This method of analysis is obviously a powerful tool, and initially does seem to rule out the faintest HHJ91 objects as brown dwarfs. There are however some assumptions in the analysis that are difficult to quantify. The method is quite sensitive to the assumed mass of GL406 and while a mass for GL406 of $0.10M_{\odot}$ is reasonable, the estimate of Jones et. al. (1994), $0.095M_{\odot}$, from the T_{eff} and m_{bol} derived by their method and the models of Burrows et. al. (1993) is just as good. The 70 Myr $0.08M_{\odot}$ point lies $3\times$ higher in bolometric luminosity than the $0.095M_{\odot}$ point according to Burrows et al. (1993). Therefore for this assumed mass the $0.08M_{\odot}$ point occurs at $I = 17.0$, and HHJ2 and HHJ3 again become good brown dwarf candidates.

Another problem is the differing metallicities of GL406 and the Pleiades sample. GL406 belongs to the old disk population according to Leggett (1992), and will therefore have lower metallicity than the Pleiads. This will effect the surface opacities and hence the bolometric correction and colour of this object compared to the Pleiades objects, and therefore adds another uncertainty.

While this new method of analysis is therefore certainly appealing, in the light of the uncertainties outlined above it can not rule out the brown dwarf candidates presented here.

7.3 Final Conclusion

In his thesis Hambly (1991) stated "This work originally set out to *discover* brown dwarfs ... While it would be nice to be able to unequivocally identify a brown dwarf, it has to be said that the only way to do so is to measure such a low mass and total luminosity for a star that it cannot be anything else. Given that accurate masses can only be determined for those objects in binary systems and that the theoretical lowest luminosity for a 'normal' star is uncertain to a large degree, such measurements are extremely difficult."

While much progress (evidenced by the work presented here, and the many recent publications referenced herein) has been made in the study of brown dwarfs in the last three years, these statements of Hambly (1991) are still essentially valid. The brown dwarf candidates presented in this thesis are much strengthened by the work presented here compared with the initial tentative identifications made by HHJ91. They remain candidates however, and will do so until model atmospheres are developed that allow the determination of their effective temperatures to accuracies of a few percent and theorists finally agree on a standard set of brown dwarf models. Both of these will happen eventually, although the timescales involved will almost inevitably turn out to be longer than anyone expects. Until then the candidates identified here remain the faintest known proper motion members of the Pleiades, and the best young cluster brown dwarf candiates. In addition the identification of HHJ54 as a possible brown dwarf binary, with a component of estimated mass $\sim 0.035 M_{\odot}$ is very exciting. If this companion could be confirmed, either by high resolution imaging or high dispersion spectroscopy, and its luminosity determined, then here would be the object of such a low luminosity that it can't be anything but a brown dwarf. Follow up observations of this object should therefore be made as soon as possible.

Much other work remains to be done on the Pleiades sample of HHJ91, both in terms of further exploration of the characteristics of the faintest objects, and in using it as a homologous sample of low mass stars of different masses but constant age and metallicity. Suggestions for future work (in no particular order) include:

- A programme of high accuracy I and K band photometry to quantify the binary statistics of the cluster. This has important implications for theories of binary formation.
- Further CGS4 spectroscopy at 2.2 microns of a larger sample of the binary sequence objects in order to search for evidence of other very low mass companions.
- Further CGS4 spectroscopy over the complete range 1-2.5 microns to apply the method of Jones et al. (1994) for a larger sample of objects to refine the $I-K$ temperature scale for the cluster.
- HST imaging and high dispersion spectroscopy of the potential binary objects. Note these techniques are sensitive to different binary separations and the spectroscopic technique only applicable to objects of approximately equal mass (otherwise the strengths of the doubled line components will be so different as to make their detection impossible).
- A superCOSMOS survey of the cluster using I band plates to derive the proper motions. This would reach ~ 1 magnitude deeper than the survey of HHJ91 and should therefore give some excellent brown dwarf candidates.
- Longer Wavelength infrared observations of the cluster using ISO to search for unresolved companions, evidence of vestigial formation disks and to help derive more accurate bolometric luminosities for the objects.
- A deep CCD survey of the cluster at R and I. This would identify many good, faint brown dwarf candidates although without the security of proper motions. However such a survey would provide an invaluable first epoch for a second survey 5 years hence which would give proper motion information down to

$I \sim 22$. Such a proper motion survey would map the cluster mass function down to $\sim 0.02 M_{\odot}$ and should discover a large number of undoubted brown dwarfs.

- Further investigations of the activity of the Pleiades sample, both by further FOS and higher resolution spectroscopy and by X-ray observations by forthcomming satellite missions.

- Investigations of other clusters. Hambly et. al. (1994a,b) have produced a proper motion survey of Praesepe, and plan to investigate several other clusters. This will generate further high quality samples of low mass stars for investigation at all wavelengths.

Appendix A

Tables of Theoretical Models

In this appendix I give the luminosities and effective temperatures for the theoretical models used in the course of this work. Also given are I magnitudes and $I-K$ colours, produced from the transforms of Bessell (1991) assuming a Pleiades distance modulus of 5.65.

A.1 Stringfellow (1991)

Age 1 Myr.

Mass	T_{eff}	$\log(L/L_{\odot})$	$I-K$	I
0.15	2850	-1.00	3.04	12.88
0.10	2780	-1.26	3.26	13.40
0.09	2760	-1.30	3.34	14.05
0.08	2750	-1.40	3.38	14.22
0.07	2740	-1.50	3.42	14.68
0.06	2720	-1.58	3.50	14.68
0.05	2700	-1.70	3.60	15.00
0.04	2660	-1.83	3.82	15.72
0.03	2630	-2.00	3.94	16.03
0.02	2575	-2.23	4.20	16.94
0.01	2450	-2.66	4.58	18.38

Age 6 Myr.

Mass	T_{eff}	$\log(L/L_\odot)$	$I-K$	I
0.20	2980	-1.38	2.73	13.61
0.15	2930	-1.56	2.83	14.15
0.10	2860	-1.78	3.00	14.81
0.09	2850	-1.82	3.04	14.93
0.08	2830	-1.88	3.10	15.13
0.07	2800	-1.98	3.19	15.45
0.06	2780	-2.04	3.26	15.66
0.05	2750	-2.14	3.38	16.01
0.04	2720	-2.24	3.50	12.85
0.03	2660	-2.40	3.82	17.03
0.02	2570	-2.78	4.22	18.34

Age 10 Myr.

Mass	T_{eff}	$\log(L/L_\odot)$	$I-K$	I
0.20	3010	-1.50	2.66	13.87
0.15	2950	-1.70	2.79	14.42
0.10	2880	-1.90	2.95	15.12
0.09	2860	-2.00	3.00	15.36
0.08	2840	-2.06	3.07	15.61
0.07	2820	-2.14	3.13	15.82
0.06	2800	-2.22	3.19	16.06
0.05	2760	-2.36	3.34	16.52
0.04	2710	-2.46	3.55	16.98
0.03	2660	-2.62	3.82	17.56
0.02	2550	-2.88	4.29	18.66

Age 50 Myr.

Mass	T_{eff}	$\log(L/L_{\odot})$	$I-K$	I
0.20	3050	-1.98	2.59	15.02
0.15	2990	-2.18	2.70	15.60
0.10	2920	-2.38	2.85	16.20
0.09	2890	-2.46	2.92	16.44
0.08	2870	-2.54	2.98	16.69
0.07	2840	-2.62	3.06	16.95
0.06	2780	-2.72	3.27	17.39
0.05	2720	-2.86	3.50	17.88
0.04	2600	-3.02	4.08	14.73

Age 70 Myr.

Mass	T_{eff}	$\log(L/L_{\odot})$	$I-K$	I
0.20	3040	-2.08	2.61	15.42
0.15	2985	-2.26	2.72	15.95
0.10	2900	-2.53	2.90	16.75
0.09	2880	-2.57	2.94	16.90
0.08	2860	-2.62	3.01	17.13
0.07	2820	-2.74	3.12	17.43
0.06	2765	-2.82	3.32	17.80
0.05	2680	-2.99	3.75	18.59
0.04	2480	-3.16	4.48	19.69
0.03	2000	-3.8	~ 6.5	~ 22.5

Age 300 Myr.

Mass	T_{eff}	$\log(L/L_{\odot})$	$I-K$	I
0.20	3045	-2.38	2.60	16.18
0.15	2985	-2.60	2.71	16.80
0.10	2860	-2.95	3.01	17.88
0.09	2795	-3.04	3.21	18.27
0.08	2700	-3.16	3.60	18.88

A.2 Burrows et. al. (1993)

Age 70 Myr.

Mass	T_{eff}	$\log(L/L_{\odot})$	$I-K$	I
0.20	3550	-2.03	2.19	15.05
0.15	3240	-2.22	2.32	15.60
0.10	3090	-2.50	2.53	16.43
0.09	3040	-2.57	2.61	16.71
0.08	2980	-2.65	2.72	16.93
0.07	2910	-2.73	2.88	17.30
0.06	2830	-2.85	3.09	17.71
0.05	2710	-3.00	3.55	18.45
0.04	2530	-3.18	4.36	19.63

A.3 Nelson, Rappaport & Joss (1993)

Age 70 Myr.

Mass	T_{eff}	$\log(L/L_{\odot})$	$I-K$	I
0.20	3270	-2.15	2.28	15.40
0.15	3180	-2.30	2.39	15.85
0.10	3130	-2.65	2.47	16.72
0.09	2990	-2.70	2.70	17.05
0.08	2920	-2.80	2.86	17.40
0.07	2820	-2.85	3.03	17.65
0.06	2770	-2.95	3.30	18.12
0.05	2660	-3.10	3.82	19.06
0.04	2450	-3.35	4.58	20.28

A.4 D'Antona & Mazzitelli (1985)

Age 70 Myr.

Mass	T_{eff}	$\log(L/L_\odot)$	$I-K$	I
0.40	3530	-1.71	2.00	14.13
0.30	3420	-1.86	2.11	14.57
0.20	3310	-2.04	2.22	15.10
0.15	3175	-2.33	2.39	15.93
0.10	3095	-2.47	2.52	16.36
0.09	3040	-2.55	2.61	16.60
0.08	2982	-2.64	2.72	16.92
0.07	2878	-2.77	2.95	17.40
0.06	2745	-2.92	3.40	18.13

A.5 D'Antona & Mazzitelli (1994)

Age 70 Myr.

Mass	T_{eff}	$\log(L/L_\odot)$	$I-K$	I
0.30	3573	-1.765	-	-
0.20	3443	-2.025	2.08	14.98
0.15	3365	-2.207	2.17	15.48
0.10	3258	-2.462	2.29	16.20
0.09	3221	-2.530	2.34	16.39
0.08*	3176	-2.609	2.40	16.62
0.07	3126	-2.700	2.47	16.89
0.06	3055	-2.812	2.58	17.25
0.05	2917	-2.966	2.86	17.82
0.04	2540	-3.405	4.18	20.01

* Note that the parameters for this mass appear to be given incorrectly in the original paper (all masses shifted up by one age division). This is (presumably) the correct T_{eff} and L_{bol}

Appendix B

Pleiades: Infrared Photometry

B.1 Observations of HHJ91 proper motion members

ID	RA	DEC	R(±0.21)	I(±0.12)	J(±0.04)	H(±0.04)	K(±0.04)
HHJ2	03 35 27	25 20 33	19.38*	17.30*	15.26	14.72	14.37
HHJ291	03 36 50	23 41 15	15.93	14.45	12.65	12.10	11.83
HHJ236	03 39 11	26 40 14	16.79	14.79	13.28	12.41	12.25
HHJ153	03 39 51	23 25 18	16.95	15.20	13.58	13.07	12.78
HHJ320	03 39 56	25 49 21	16.05	14.22	12.66	12.21	11.84
HHJ413	03 40 17	26 30 57	15.12	13.38	12.07	11.50	11.25
HHJ89	03 40 17	26 20 52	17.75	15.74	14.47	13.96	13.72
HHJ321	03 40 47	22 53 54	15.49	14.21	12.72	11.96	11.73
HHJ391	03 40 53	25 19 04	15.25*	13.52*	12.32	11.64	11.41
HHJ5	03 41 38	23 25 18	19.22	17.04	14.87	14.30	13.95
HHJ139	03 42 03	24 55 58	17.15	15.34	13.73	13.13	12.84
HHJ81	03 42 09	25 13 09	17.87	15.75	13.86	13.33	12.97
HHJ204	03 42 11	22 29 08	16.59	14.96	13.30	12.73	12.48
HHJ425	03 42 16	24 57 16	14.62	13.17	11.86	11.24	11.05
HHJ410	03 42 17	25 06 27	14.96	13.43	11.88	11.37	11.08
HHJ25	03 42 52	24 16 52	19.05	16.48	14.64	14.02	13.77
HHJ27	03 42 59	23 53 46	18.42	16.44	14.59	13.99	13.70

ID	RA	DEC	R(±0.21)	I(±0.12)	J(±0.04)	H(±0.04)	K(±0.04)
HHJ127	03 43 01	23 39 28	17.34	15.47	13.91	13.33	13.09
HHJ297	03 43 12	22 33 19	15.99	14.37	12.80	12.15	11.91
HHJ319	03 43 45	25 18 15	15.71	14.22	12.74	12.12	11.90
HHJ390	03 44 04	25 13 36	15.33*	13.73*	12.14	11.47	11.23
HHJ37	03 44 10	24 06 21	18.45	16.24	14.49	13.90	13.57
HHJ92	03 44 13	24 04 40	18.00	15.74	14.05	13.51	13.20
HHJ198	03 44 26	24 06 04	17.12	14.99	13.87	13.38	13.05
HHJ26	03 44 45	23 54 44	18.24	16.44	15.07	14.37	14.15
HHJ15	03 44 48	22 03 31	18.68	16.71	14.74	14.15	13.88
HHJ21	03 45 07	23 15 03	18.69	16.59	14.80	14.24	13.91
HHJ288	03 45 09	23 35 13	15.99	14.45	12.82	12.33	12.03
HHJ373	03 45 25	22 43 12	15.03	13.72	12.28	11.78	11.43
HHJ339	03 45 28	23 02 20	15.89	14.06	12.21	11.51	11.30
HHJ10	03 45 37	22 44 33	18.94	16.90	14.75	14.13	13.75
HHJ3	03 45 53	22 35 22	19.56*	17.41*	15.08	14.50	14.23
HHJ8	03 45 56	24 12 33	19.23	16.94	14.91	14.34	14.04
HHJ440	03 46 07	23 35 16	14.25	12.97	11.62	10.98	10.76
HHJ22	03 49 53	23 24 55	18.48	16.55	14.64	14.04	13.67
HHJ13	03 50 05	24 55 23	18.66	16.75	14.74	14.19	13.87
HHJ28	03 50 49	23 40 20	18.44	16.43	14.32	13.73	13.43
HHJ20	03 51 02	23 10 52	18.11	16.59	14.73	14.15	13.82
HHJ144	03 52 23	22 23 26	16.75	15.27	13.90	13.21	13.08
HHJ430	03 53 30	24 08 39	14.89	13.08	11.10	10.59	10.26
HHJ17	03 53 51	25 01 27	18.92	16.68	14.82	14.23	13.84
HHJ85	03 54 07	22 40 38	17.34	15.74	14.24	13.71	13.50
HHJ4	03 54 50	23 20 07	18.91*	17.20*	15.37	14.86	14.53
HHJ7	03 54 52	21 59 57	19.32*	???*	14.83	14.29	13.97
HHJ292	03 55 56	24 10 02	16.19	14.43	12.92	12.07	12.05
HHJ133	03 56 14	25 45 38	16.92	15.39	13.90	13.18	13.03
HHJ39	03 56 29	22 12 55	17.93	16.23	14.68	14.15	13.80

B.2 Observations of *I*-only objects

ID	RA	DEC	R	I(±0.25)	J(±0.03)	H(±0.07)	K(±0.08)
I16	03 38 12.4	24 37 42	19.61*	17.39*	15.35	14.65	14.41
I15	03 39 32.4	24 38 49	-	17.96	16.41	15.90	15.66
I8	03 41 42.1	25 05 06	19.66*	17.51*	15.67	15.10	14.71
I4	03 42 42.5	25 36 23	-	17.85	-	-	15.22
I25	03 43 26.8	24 14 46	-	17.75	16.21	15.64	15.43
I3	03 44 12.4	25 57 10	19.37*	17.32*	15.58	15.05	14.77
I17	03 45 07.6	24 35 06	-	17.76	-	-	14.89
I10	03 45 29.1	24 52 32	-	18.07	-	-	15.69
I12	03 46 38.6	24 48 23	-	17.90	-	-	15.39
I5	03 46 45.1	25 23 37	-	18.05	17.04	16.19	15.94
I7	03 48 09.4	25 09 53	19.18*	17.38*	15.42	14.88	14.55
I11	03 49 37.8	24 51 51	-	18.08	-	-	15.59
I13	03 51 34.8	24 47 03	-	17.84	-	-	15.18
I14	03 52 23.1	24 40 22	20.36*	18.05*	15.48	14.87	14.59

B.3 Observations of HHJ91 members reproduced from HHJ91

ID	RA	DEC	R (±0.21)	I (±0.12)	J (±0.04)	H (±0.04)	K(±0.04)
HHJ19	03 34 15	26 19 41	18.45	16.62	14.51	13.88	13.52
HHJ101	03 37 32	25 19 03	17.53	15.69	13.67	13.08	12.90
HHJ12	03 38 36	23 02 10	18.87	16.82	14.76	14.21	13.90
HHJ6	03 38 44	23 45 23	19.34	16.99	14.67	14.06	13.71
HHJ58	03 38 51	22 53 49	17.77	15.93	13.78	13.17	12.86
HHJ18	03 40 10	22 08 20	18.54	16.64	14.14	13.58	13.16
HHJ46	03 41 38	24 16 15	18.29*	16.32*	14.10	13.49	13.21
HHJ24	03 41 47	24 13 40	18.39	16.46	14.46	13.79	13.52
HHJ54	03 42 01	23 11 56	17.78	15.93	13.99	13.39	13.07
HHJ14	03 42 14	23 44 24	18.87	16.75	14.55	13.90	13.59
HHJ118	03 42 14	24 06 02	17.89	15.54	13.75	13.05	12.79
HHJ11	03 43 04	22 03 10	18.77	16.82	14.55	13.87	13.65
HHJ30	03 43 33	22 52 18	18.29	16.38	14.37	13.68	13.41
HHJ9	03 43 36	23 15 56	19.89	16.92	15.02	14.30	14.04
HHJ1	03 43 42	22 38 31	19.49*	17.85*	16.23	15.53	15.26
HHJ23	03 44 25	22 52 44	18.30	16.47	14.57	13.90	13.78
HHJ16	03 44 31	23 24 02	18.64*	16.62*	14.13	13.56	13.35
HHJ10	03 45 37	22 44 33	18.94	16.90	14.73	14.09	13.72
HHJ36	03 46 17	22 13 43	18.14*	16.18*	14.00	13.44	13.17
HHJ79	03 46 28	22 53 44	17.49	15.75	13.78	13.19	12.99

Appendix C

Pleiades: FOS Spectral Indices and Equivalent Widths

C.1 Spectral indices

C.1.1 Kirkpatrick (1991) ratios

Object	Ratio A	Ratio B	Ratio C	Ratio D
g65ab.1	1.46	1.08	1.25	1.04
g65ab.2	1.41	1.07	1.24	1.04
g806	1.17	1.04	1.14	1.10
g809	1.11	1.03	1.16	1.10
g829	1.27	1.06	1.14	1.08
g875.1	1.25	1.06	1.14	1.07
g905.2	1.23	1.06	1.09	1.09
g905	1.29	1.06	1.16	1.03
hhj101	1.49	1.10	1.14	1.05
hhj111	1.38	1.08	1.15	1.04
hhj12	1.44	1.08	1.19	1.06
hhj139	1.50	1.09	1.22	1.01

Object	Ratio A	Ratio B	Ratio C	Ratio D
hhj144	1.26	1.06	1.10	1.11
hhj16	1.45	1.08	1.16	1.02
hhj161	1.32	1.11	1.17	1.07
hhj18	1.41	1.08	1.17	1.02
hhj19	1.45	1.07	1.19	1.02
hhj2	1.40	1.07	1.14	1.06
hhj229	1.40	1.10	1.22	1.07
hhj23	1.29	1.09	1.12	1.05
hhj250	1.38	1.12	1.15	1.06
hhj257	1.45	1.07	1.20	1.06
hhj298	1.36	1.07	1.13	1.06
hhj3	1.39	1.08	1.12	1.03
hhj336	1.29	1.05	1.13	1.07
hhj36	1.44	1.09	1.15	1.06
hhj37	1.38	1.07	1.17	1.06
hhj390	1.34	1.09	1.13	1.07
hhj391	1.25	1.05	1.11	1.07
hhj427	1.23	1.07	1.19	1.26
hhj429	1.26	1.07	1.15	1.07
hhj430	1.39	1.08	1.11	1.05
hhj435	1.11	1.05	1.17	1.13
hhj436	1.17	1.06	1.09	1.10
hhj44	1.39	1.06	1.14	1.06
hhj48	1.55	1.07	1.18	1.04
hhj54	0.00	1.07	1.14	1.07
hhj58	1.40	1.08	1.17	1.08
hhj59	1.35	1.08	1.14	1.08
hhj6	1.48	1.16	1.16	1.05
hhj7	1.46	1.06	1.13	1.07
hhj9	1.31	1.04	1.13	1.05

C.1.2 Hamilton & Stauffer (1993) indices

Object	$[TiO]_1$	$[TiO]_2$	$[TiO]_3$	$[TiO]_4$	$[VO]$	$[PC]$	$[PC]_2$
g65ab.1	2.08	1.58	1.20	0.31	0.21	0.38	0.82
g65ab.2	1.98	1.57	1.18	0.22	0.21	0.39	0.89
g806	0.77	0.36	0.16	-0.05	0.09	0.20	0.53
g809	0.58	0.28	0.12	-0.05	0.07	0.16	0.42
g829	1.09	0.57	0.33	0.01	0.09	0.23	0.60
g875.1	1.05	0.54	0.34	-0.01	0.11	0.21	0.56
g905.2	1.00	0.76	0.51	0.01	0.11	0.25	0.63
g905	1.79	1.19	0.77	0.27	0.21	0.42	0.97
hhj101	1.85	0.75	0.51	0.11	0.19	0.24	0.72
hhj111	1.61	0.95	0.62	0.13	0.15	0.33	0.80
hhj12	1.87	0.91	0.51	0.17	0.20	0.40	0.92
hhj139	1.75	0.95	0.68	0.25	0.21	0.27	0.63
hhj144	1.10	0.73	0.51	0.02	0.10	0.22	0.68
hhj16	1.91	0.95	0.54	0.25	0.20	0.41	0.86
hhj161	1.51	0.86	0.52	0.03	0.18	0.34	0.86
hhj18	1.88	0.83	0.50	0.35	0.20	0.33	0.74
hhj19	1.91	0.88	0.48	0.26	0.23	0.40	0.89
hhj2	2.17	0.89	0.47	0.26	0.29	0.42	1.17
hhj229	1.50	0.86	0.57	0.09	0.15	0.29	0.66
hhj23	1.53	0.88	0.51	0.18	0.14	0.37	0.87
hhj250	1.37	0.87	0.59	0.03	0.14	0.28	0.66
hhj257	1.61	0.85	0.48	0.12	0.17	0.37	0.79
hhj298	1.37	0.85	0.58	0.08	0.14	0.27	0.73
hhj3	2.01	1.13	0.62	0.29	0.24	0.51	1.06

Object	$[TiO]_1$	$[TiO]_2$	$[TiO]_3$	$[TiO]_4$	$[VO]$	$[PC]$	$[PC]_2$
hhj336	1.07	0.82	0.58	0.00	0.12	0.24	0.62
hhj36	1.75	0.88	0.48	0.17	0.16	0.40	0.86
hhj37	1.82	0.98	0.61	0.18	0.20	0.37	0.81
hhj390	1.25	0.71	0.42	0.05	0.13	0.29	0.69
hhj391	0.90	0.64	0.42	-0.03	0.09	0.22	0.62
hhj427	0.99	0.71	0.52	-0.04	0.11	0.19	0.53
hhj429	1.05	0.65	0.43	0.00	0.13	0.22	0.60
hhj430	1.73	0.96	0.64	0.24	0.18	0.32	0.82
hhj435	0.53	0.68	0.49	-0.13	0.09	0.19	0.58
hhj436	0.64	0.70	0.49	-0.03	0.08	0.21	0.57
hhj44	1.62	0.82	0.46	0.11	0.18	0.36	0.81
hhj48	1.83	1.00	0.61	0.18	0.19	0.39	0.83
hhj54	1.65	0.75	0.40	0.13	0.16	0.35	0.80
hhj58	1.75	0.98	0.63	0.16	0.20	0.35	0.83
hhj59	1.49	0.91	0.56	0.12	0.16	0.35	0.81
hhj6	2.03	1.00	0.60	0.41	0.26	0.40	1.02
hhj7	2.02	1.00	0.54	0.27	0.21	0.46	0.96
hhj9	1.31	0.80	0.46	0.01	0.18	0.34	0.79

C.2 Hα and Na Equivalent Widths

Object	$EW_{H\alpha}$ (Å)	Continuum (mJy)	EW_{NaI} (Å)	Continuum (mJy)
hhj2	3.2	0.057	5.9	0.46
hhj3	4.1	0.064	4.9	0.54
hhj6	<2	0.053	5.6	0.49
hhj7	3.3	0.11	5.5	0.78
hhj9	<2	0.072	3.5	0.34
hhj12	<2	0.09	6.3	0.55
hhj16	6.8	0.16	5.4	0.96
hhj18	4.1	0.058	4.8	0.43
hhj19	3.1	0.078	5.7	0.48
hhj23	<2	0.12	4.8	0.63
hhj36	5.2	0.31	5.4	1.70
hhj37	3.8	0.22	5.1	1.21
hhj44	2.9	0.15	4.9	0.73
hhj48	11.1	0.30	4.9	1.61
hhj54	1.8	0.42	4.8	2.0
hhj58	2.8	0.28	5.3	1.47
hhj59	1.9	0.32	4.6	1.41
hhj101	5.9	0.21	4.3	1.55
hhj111	5.6	0.39	5.0	1.78
hhj139	2.5	0.21	5.3	0.97
hhj144	<2	0.56	3.0	1.89
hhj161	3.0	0.27	4.8	1.20
hhj229	5.0	0.61	5.2	2.55
hhj250	2.5	0.69	4.5	2.75
hhj257	4.4	0.53	5.7	2.44
hhj298	6.2	1.5	4.1	5.4
hhj336	2.6	2.2	3.8	6.4

Object	$EW_{H\alpha}$ (Å)	Continuum (mJy)	EW_{NaI} (Å)	Continuum (mJy)
hhj390	3.9	4.4	3.8	15.1
hhj391	2.5	5.4	3.4	13.9
hhj427	1.5	1.78	4.8	4.7
hhj429	3.4	3.4	3.9?	9.7
hhj430	5.4	2.3	3.2	12.1
hhj435	0.4	3.9	4.1	8.6
hhj436	1.6	7.7	2.8	17.1
g65ab.1	4.0	95	7.5	610
g65ab.2	2.0	105	7.1	670
g806	No emission	350	3.4	870
g809	No emission	3400	3.2	6900
g829	No emission	950	3.5	2770
g875.1	2.8	240	4.2	660
g905	No emission	140	6.3	980
g905.2	No emission	300	3.0	920

References

Adams, F., 1994, in proc. ESO Workshop "The Bottom of the Main Sequence and Beyond", ed. C. Tinney (Garching, ESO), in press.

Alcock et. al., 1993, Nat., 365, 621.

Allard, F., 1990, PhD Thesis, Univ. Heidelburg.

Allard, F., 1994, in ASP Conference Series Vol. 64 "Cool Stars, Stellar Sytems, and the Sun - 8th Cambridge Workshop", ed. J.P.Caillault.

Allen, C.W., 1973, "Astrophysical Quantities", 3rd Edition, Athlone Press.

Allington-Smith, J.R., et. al., 1989, MNRAS, 238, 603.

Aubourg et. al., 1993, Nat., 365, 623.

Bahcall, J.N., 1987, in proc. IAU Symposium No. 177, "Dark Matter in the Universe", ed. J. Kormendy, G.R. Knapp.

Bailey, J, 1991, UKIRT Observer Note 9.1, ROE.

Barnbaum, C., Zuckerman, B., 1992, ApJ, 396, L31.

Becklin, E.E., Zuckernan, B., 1988, Nat., 336, 656.

Berriman, G., Reid, N., 1987, MNRAS, 227, 315.

Berriman, G., Reid, N., Leggett, S.K., 1992, ApJ, 392, L31.

Bessell, M.S., 1979, PASP, 91, 598.

Bessell, M.S., 1983, PASP, 95, 480.

Bessell, M.S., 1986, PASP, 98, 1303.

Bessell, M.S., 1987, PASP, 99, 642.

Bessell, M.S., 1991, AJ, 101, 662.

Bessell, M.S, Brett, J.M., 1988, PASP, 100, 1134.

Bessell, M.S., Weis, E.W., 1987, 99, 642.

Boesgaard, A.N., Friel, E.D., 1990, ApJ, 351, 467.

Bohm-Vitense, E, 1989, "Introduction to Stellar Astrophyics", Vol. 1, Cambridge University Press.

Boss, A.P., 1991, Nat., 351, 298.

Breger, M., 1987, ApJ, 319, 754.

Bryja, C., Jones, T.J., Humphreys, R.M., Lawrence, G., Pennington, R.L., Zumach, W., 1992, ApJ, 388, L23.

Bryja, C., Humphreys, R.M., Jones, T.J., 1994, AJ, 107, 246.

Burrows, A., Hubbard, W.B., Saumon, D., Lunine, J.I., 1993, ApJ, 406, 158.

Burrows, A., Hubbard, W.B., Saumon, D., Lunine, J.I., 1994, preprint.

Burrows, A., Liebert, J., 1993, Rev. Mod. Phys, 65, 301.

Burstein, P., Heiles, C., 1982, A&A, 87, 1165.

Clegg, R.E.S, Carter, D., Charles, P.A., Dick, J.S.B., Jenkins, C.R., King, D.L., Laing, R.A., 1992, "ISIS Astronomers Guide", RGO.

Comeron, F.G., Rieke, H., Burrows, A., Rieke, M.J., 1993, ApJ, 416, 185.

Cousins, A.W., 1976, Mem. RAS, 81, 25.

Crawford, D.L., Perry, C.L., 1976, AJ, 81, 419.

Currie, M.J., 1992, Starlink User Note 95.

D'Antona, F., Mazzitelli, I., 1985, ApJ, 296, 502.

D'Antona, F., Mazzitelli, I., 1994, ApJS, 90, 467.

D'Antona, F., 1994, in proc. ESO Workshop "The Bottom of the Main Sequence and Beyond", ed. C. Tinney (Garching, ESO), in press.

Draper, P.W., Eaton, N., 1992, Starlink User Note 109.

Drukier, G.A., Fahlman, G.G., Richer, H.B., VandenBerg, D.A., 1988, AJ, 95, 1415.

Duquennoy, A., Mayor, M., 1991, A&A, 248,455.

Eggen, O.J., Iben, I., 1988, AJ, 96, 635.

Eichhorn, H., Googe, W.G., Lukac, C.F., Murphy, J.K., 1970, Mem. RAS, 73, 125.

Erro, B.I, 1969, Bol. Inst. Tonantzintla, 5, 89.

T̈ay, T.D., Jr., Stein, W.L., Warren, W.H., Jr., 1974, PASP, 86, 772.

Faber, S.M., Gallagher, J.S., 1979, ARA&A, 17, 135.

Fabian, A.C., Nulsen, P.E.J., Canizares, C.R., 1991, AArev, 1991, 2, 191.

Fahlman, G.C., Richer, H.B., Searle, L., Thompson, I.B., 1989, ApJ, 349, L49.

Feigelson, E.D., Nelson, P.I., 1985, ApJ, 293, 192.

Fillipenko, A.V., 1982, PASP, 94, 715.

Flemming, T.A., Giampapa, M.S., 1989, ApJ, 346, 299.

Forrest, W.J., Ninkov, J.D., Garnett, J.D., Strutskie, M.F., Shure, M., 1989, in proc. "Third Infrared Detector Technology Workshop", ed. C.R. McCreight (NASA), 221.

Gatewood G., Castelaz, M., Han, I., Persinger, G., Stein, J., Stephenson, B., Tangern,

W., 1990, ApJ, 364, 144.

Giampapa, M.S., Liebert, J., 1986, ApJ, 305, 784.

Gilmore, G., 1993, in "4th Canary Islands Winterschool on Infrared Astronomy", Cambridge University Press.

Glazebrook, K., Peacock, J.A., Collins, C., Miller, L., 1993, MNRAS, 266, 65.

Golub, L., Rosner, R., Vaiana, G.S., Weiss, N.O., 1981, ApJ, 243, 309.

Graham, J.R., Matthews, K., Neugebauer, G., Soifer, B.T., 1990a, ApJ, 357, 216.

Graham, J.R., McCarthy, J.K, Reid, I.N., Rich, R.M., 1990b, ApJ, 357, L21.

Guarnieri, M.D., Dixon, R.I., Longmore, A.J., 1991, PASP, 103, 675.

Hambly, N.C., 1991, PhD Thesis, Univ. Leicester.

Hambly, N.C., Hawkins, M.R.S., Jameson, R.F., 1991, MNRAS, 253, 1. – HHJ91

Hambly, N.C., Hawkins, M.R.S., Jameson, R.F., 1993, A&AS, 100, 607. – HHJ93.

Hambly, N.C., Steele, I.A., Hawkins, M.R.S., Jameson, R.F., 1994a, A&AS, in press.

Hambly, N.C., Steele, I.A., Hawkins, M.R.S., Jameson, R.F., 1994b, MNRAS, in press.

Hamilton, D., Stauffer, J.R., 1993, AJ, 105, 1855. – HS93

Harris, G., 1976, ApJS, 30, 451.

Hawkins, M.R.S., 1986, MNRAS, 223, 845.

Hawkins, M.R.S., 1994, in ASP Conference Series Vol. 64 "Cool Stars, Stellar Sytems, and the Sun - 8th Cambridge Workshop", ed. J.P.Caillault.

Hawkins, M.R.S., Bessel, M.S., 1988, MNRAS, 234, 177.

Heintz, W.D., 1978, ApJ, 20, 931.

Heintz, W.D., 1989, A&A, 217, 145.

Henry, T.J., Johnson, D.S., McCarthy, D.W., Kirkpatrick, J.D., 1992, A&A, 254, 116.

Herbig, G.H., 1985, ApJ, 289, 269.

Hertzsprung, E., 1947, Annu. Leiden Obs., 19, Part 1A.

Hoffliet, D., Jaschek, C., 1982, "The Bright Star Catalogue", Yale University Observatory.

Jameson, R.F., Sherrington, M.R., Giles, A.B., 1983, MNRAS, 205, 30P.

Jameson, R.F., Skillen, W.J.I., 1989, MNRAS, 239, 247.

Johnson, H.L., Morgan, W.W., 1953, ApJ, 117, 313.

Jones, B.F., 1973, A&S, 9, 313.

Jones, B.F., 1981, AJ, 86, 290.

Jones, H.R.A., Longmore, A.J, Jameson, R.F., Mountain, C.M., 1994, MNRAS, 267, 413. – JLJM94

Jones, H.R.A., Miller, L., Glazebrook, K., 1994, MNRAS, 270, L47.

Kaplan, E.L., Meier, P., 1958, J.Am.Stat.Ass., 53, 457.

King, D.L., 1985, RGO La Palma technical note 31.

Kirkpatrick, J.D., Henry, T.J., Liebert, J., ApJ, 406, 701.

Kirkpatrick, J.D., Henry, T.J., McCarthy, D.W., Jr., 1991, ApJS, 77, 417 – K91.

Kirkpatrick, J.D., Kelly, D.M., Rieke, G.H., Liebert, J., Allard, F., Wehrse R., 1993, ApJ, 402, 643.

Kirkpatrick, J.D., McCarthy, D.W., Jr., 1994, AJ, 107, 333.

Kitchin, C.R., 1991, "Astrophysical Techniques", 2nd edition, Adam Hilger.

Kleinmann, S.G., Hall, D.N.B., 1986, ApJS, 62, 501.

Kroupa, P., Tout, C., Gilmore, G., 1990, MNRAS, 244, 76.

Kroupa, P., Tout, C., Gilmore, G., 1991, MNRAS, 251, 293.

Kumar, S.S., 1963, ApJ, 137, 1211 .

Latham, D.W., Mazeh, T., Stefanik, R.P., Mayor, M., Burki, G., 1989, Nat., 339, 38.

Leggett, S.K., 1992, ApJS, 82, 351.

Leggett, S.K., Harris, H.C., Dahn, C.C., 1994, AJ, 108, 944.

Leggett, S.K., Hawkins, M.R.S., 1988, MNRAS, 234, 1065.

Leggett, S.K., Hawkins, M.R.S., 1989, MNRAS, 238, 145.

Liebert, J., Probst, R.G., 1987, ARA&A, 25, 473.

Liebert, J., Staffer, R.A., Nosworthy, J., Giampapa, M.S., Stauffer, J.R., 1992, in Seventh Cambridge Workshop on Cool Stars, Stellar Systems, and the Sun, ASP Conference Series 26, ed. M.S. Giampapa and J.A.Bookbinder.

Ludwig, C.B., 1971, Appl. Opt., 10, 1057.

MacGillivray, H.T., Stobie, R.S., 1984, Vistas in Astronomy, 27, 433.

Magazzu, A., Rebolo, R., Martin, E.L., 1994, ApJ, submitted.

Marcy, G.W, Basri, G., Graham, J.R., 1994, ApJ, letter in press.

Marcy, G.W., 1994, in proc. ESO Workshop "The Bottom of the Main Sequence and Beyond", ed. C. Tinney (Garching, ESO), in press.

Martin, E., 1993, PhD Thesis, Univ. La Laguna.

McLean, I.S., 1987, in Infrared Astronomy with Arrays, ed. C.G. Wynn-Williams, E.E. Becklin (Honolulu, Univ. Hawaii), 180.

McLean, I.S., 1987, in proc of ESO Conference "Very Large Telescopes and their Instrumentation", Volume II, ed. M.H.Ulrich (Garching, ESO), 955.

Mountain, C.M., Robertson, D.J., Lee, T.J., Wade, R., 1990, ROE Preprint 7/90 presented at SPIE Symposium on Astronomical Telecopes and Intrumentation for the 21st Century (Tuscon).

Mould, J.R., 1978, ApJ, 226, 923.

Nelson, L.A., Rappaport, S.A., Joss, P.C., 1986, ApJ, 311, 226.

Nelson, L.A., Rappaport, S.A., Joss, P.C., 1993, ApJ, 404, 723.

O'Dell, M.A., Hendry, M.A., Collier-Cameron, A., 1994, MNRAS, 268, 181.

Oke, J.B., Gunn, J.E., 1983, ApJ, 266, 713.

Oort, J.H., 1960, Bull. Ast. Inst. Neth., 1960, 15, 45.

Parker, E.N., 1975, ApJ, 198, 205.

Patenaude, M., 1978, A&A, 66, 225.

Popper, D.M., 1980, ARA&A, 18, 115.

Probst, R., Liebert, J., 1983, ApJ, 274, 245.

Prosser, C.F., Stauffer, J.R., Kraft, R.P., 1991, AJ, 101, 1361.

Puxley, P.J., Beard, S.M., Ramsay, S.K., 1992, in proc. 4th ESO/ST-ECF Data Analysis Workshop, ed. P. Grosbul.

Pye, J.P., Hodgkin, S.T., Stern, R.A., Stauffer, J.R., 1994, MNRAS, 266, 798.

Rebolo, R., Martin, E.L., Magazzu, A., 1992, ApJ, 389, L83.

Reid, N., 1994, in proc. ESO Workshop "The Bottom of the Main Sequence and Beyond", ed. C. Tinney (Garching, ESO), in press.

Reid, N., Gilmore, G., 1984, MNRAS, 206, 19.

Reid, N., 1992, MNRAS, 257, 257.

Reid, N., 1993, MNRAS, 265, 785.

Richer, H.B., Fahlman, G.G., 1992, Nat., 358, 383.

Richer, H.B., Fahlman, G.G., Buonanno, R., Fusi Pecci, F., 1990, ApJ, 359, L11.

Richer, H.B., Fahlman, G.G., Buonanno, R., Fusi Pecci, F., Searle, L., Thompson, I.B., 1991, ApJ, 381, 147.

Richichi, A., Leinert, Ch., Jameson, R.F., Zinnecker, Z., 1994, A&A, in press.

Rieke, G.H., Rieke, M.J., 1990, ApJ, 362, L21.

Robertson, J.G., 1986, PASP, 98, 1220.

Rosner, R., 1980, in Cool Stars, Stellar Systems and the Sun (Smithsonian Astr. Obs. Spec. Rpt. 389), ed. A.K. Dupree, 79.

Salpeter, E.E., 1955, ApJ, 121, 161.

Saumon, D., Lunine, J.I., Hubbard, W.B., Burrows, A., 1994, ApJ, in press.

Shortridge, K., 1991, STARLINK MUD, Figaro – General Data Reduction & Analysis.

Simons, D.A., Becklin, E.E., 1992, ApJ, 390, 431.

Skrutskie, M.F., Forrest, W.J., Shure, M., 1989, AJ, 98, 1409.

Stauffer, J.R., 1980, AJ, 85, 1341.

Stauffer, J.R., 1982, AJ, 87, 1507.

Stauffer, J.R., 1984, ApJ, 280, 189.

Stauffer, J.R, Hamilton, D., Probst, R., Rieke, G., Mateo, M., 1989, ApJ, 344, L21.

Stauffer, J.R., Hamilton, D., Probst, R., 1994a, AJ, 108, 155.

Stauffer, J.R., Hartmann, L.W., 1987, ApJ, 318, 337.

Stauffer, J.R., Herter, T., Hamilton, D., Rieke, G.H., Rieke, M.J., Probst, R., Forrest, W., 1991, ApJ, 367, L23.

Stauffer, J.R., Liebert, J., Giampapa, M., Macintosh, B., Reid, N., Hamilton, D., 1994b, AJ, 108, 160.

Steele, I.A, Jameson, R.F., Hambly, N.C., MNRAS, 1993, 263, 647 – SJH93.

Stetson, P.B., 1987, PASP, 99, 191.

Stevenson, C.C., 1994, MNRAS, 267, 904.

Stevenson, D.J., 1991, ARA&A, 29, 163.

Stringfellow, G.S., 1991, ApJ, 375, L21.

Tarter, J.C., 1975, PhD Thesis, Univ. California, Berkley.

Tokunaga, A.T., Becklin, E.E., Zuckerman, B., 1990, 1990, ApJ, 358, L21.

Trimble, V., 1987, ARA&A, 25, 425.

Turner, D.G., 1979, PASP, 91, 642.

Unger, S.W., Brinks, E., Laing, R.A., Tritton, K.P., Gray, P.M., "La Palma Isaac Newton Group Observers Guide", RGO.

van de Kamp, P., 1977, Vistas Ast., 20, 501.

van de Kamp, P., 1981, in "Stellar Paths" (Reidel, Dordrecht).

van Leeuwen, F., 1980, in IAU Symopium No. 85 "Star Clusters", ed. J.E. Hesser, 185.

van Leuuwen, F., Alphenaar, P., Brand, J., 1986, A&AS, 65, 309.

Walter, F.M., Brown, A., Mathieu, R.D., Myers, P.C., Vrba, F.J., 1988, AJ, 96, 297.

Wright, G.S, Mountain, C.M., Bridger, A., Daly P.N., Griffin, J.L, Ramsey, S.K., 1993, ROE preprint 14/93, paper presented at SPIE Conference 1946 "IR detectors and Intrumentation" (Orlando).

Yang, E., 1989, "Microelectronic Devices", McGraw-Hill.

Zuckerman, B., Becklin, E.E., 1988, Nat., 330, 138.